CHARACTERIZATION OF SOFT 3-D PRINTED ACTUATORS FOR PARALLEL NETWORKS

by

Shashank Khetan

A Thesis

Submitted to the Faculty of Purdue University

In Partial Fulfillment of the Requirements for the degree of

Master of Science in Mechanical Engineering

School of Mechanical Engineering

West Lafayette, Indiana

May 2022

THE PURDUE UNIVERSITY GRADUATE SCHOOL
STATEMENT OF COMMITTEE APPROVAL

Dr. Laura Helen Blumenschein, Chair

School of Mechanical Engineering

Dr. David J. Cappelleri

School of Mechanical Engineering

Dr. Gregory M. Shaver

School of Mechanical Engineering

Approved by:

Dr. Nicole L. Key

Dedicated to my beloved grandmother

ACKNOWLEDGMENTS

I would like to thank my family and friends for their constant support, especially my parents, Maira, Alankriti, Aditya, and Antonio for being there through each step and providing support, both moral and research-oriented. I would also like to thank the members of RAAD Lab for being accommodating and extremely helpful with their feedback on my research. Finally, I would like to thank my advisor, Prof. Laura Blumenschein, for being an absolutely amazing mentor and making my graduate school journey positively memorable right from the start. I truly appreciate the lab hangouts, and the incredible opportunity to present our work at the RoboSoft conference in Edinburgh.

TABLE OF CONTENTS

LIST OF TABLES

LIST OF FIGURES

ABSTRACT

Soft pneumatic actuators allow compliant force application and movement for a variety of tasks. While most soft actuators have compliance in directions perpendicular to their direction of force application, they are most often analyzed only in their direction of actuation. In this work, we show a characterization of a soft 3D printed bellows actuator that considers shear and axial deformations, modeling both active and passive degrees of freedom. We build a model based on actuator geometry and a parallel linear and torsional spring system which we fit to experimental data in order to obtain the model constants. We demonstrate this model on two complex parallel networks, a delta mechanism and a floating actuator mechanism, and show how this single actuator model can be used to better predict movements in parallel structures of actuators. These results verify that the presented model and modeling approach can be used to speed up the design and simulation of more complex soft robot models by characterizing both active and passive forces of their one degree-of-freedom soft actuators.

1. INTRODUCTION

1.1 Motivation

What are soft robots, and how are they different from conventional robots? These are important and fundamental questions to be addressed before diving deeper into this work. Soft robots, as in their name, are largely constructed out of soft compliant materials [1] such as silicon elastomers, rubber (natural, synthetic), and polymer composites [2]. Traditional robots are generally made from rigid materials like steel, aluminum and ABS plastic, and are often electrically or hydraulically powered to generate large forces, and high precision. This is conducive for a manufacturing environment but not so much for natural environments or human-robot interaction [1]. Traditional robots are controlled with great precision, which is necessary due to the damage they can cause to themselves or to their environment, if they become unstable. However, the movement precision becomes challenging with increasing number of joints, which increases the degrees of freedom, and with natural environments with changing conditions [1]. Some of these computations can be reduced by exploiting natural kinematics and dynamics in design, much like the multigait robot inspired by animals without a hard internal skeleton [3], and how animals navigate complex natural environments [4].

Due to intrinsic compliance of soft robots, they are capable of performing real-world tasks that could hardly be achieved by traditional robots [5]. A few examples of such tasks are safe and direct human-robot interactions using an octopus-inspired soft robot arm [6], building assessment in areas affected by earthquakes [7], environment navigation through growth [8], enabling safer medical implants which do not come in contact with blood [9], and minimally invasive surgery [10]. The range of these tasks are exemplary in showing the potential of soft robots in multiple disciplines.

Thus far, we have shown how soft robotics and soft actuators have great potential to be used in a variety of settings that require delicate or safe operation, including exploration, human robot interaction, and biomedical devices [11]–[13]. Soft actuators in particular benefit significantly from the compliance of soft materials, allowing them to apply forces in desired directions while deforming passively and safely in non-actuated directions. This al-

lows for benefits like easier design of wearable devices compared to traditional robotics [14], beneficial natural responses when navigating cluttered environments [15], and successful under-actuation for tasks like grasping [16].

However, while these unactuated degrees of freedom offer beneficial capabilities, most analyses of soft actuators only consider the forces and displacements in the nominal direction of actuation (active), and don't consider how those forces change when the actuator is deformed in one of these unactuated directions (passive) [17]–[19]. While this doesn't inherently limit the use of these actuators or limit the benefits of passive compliance, it does mean that using the actuators in generally deformed cases may lead to errors in predicting forces and displacements. More general approaches to simulation and modeling of soft actuator forces and displacement have been shown using finite element analysis methods, either real-time for control [20], [21] or iterative for design and optimization [22]. These methods can generally achieve accurate modeling of even complex soft structures, but they require accurate knowledge of materials and structures, and can involve significant mathematical computation which can limit the use in more complex systems.

In this thesis, we present a simplified approach to modeling soft robotic systems: characterizing both active and passive forces produced by simple, one degree-of-freedom, soft actuators, with active and passive forces orthogonal to each other. These models can significantly simplify forward kinematics models when used in conjunction with geometric models like piecewise constant curvature [23], [24]. Characterizing passive forces also has potential in improving modeling of fluidic elastomer actuators to reduce position prediction errors from external reaction forces and deformations, like in soft snake robots and rolling mobile robots [25].

We demonstrate this modeling approach for soft parallel robots in haptic application ranges by characterizing its one degree-of-freedom soft actuator. Much like traditional parallel robots, soft parallel robots have multiple actuators connected to and actuating a single point. Continuum manipulators are one example of soft parallel robots where the actuators are parallel to a backbone they are collectively deforming [23]. Another class of parallel soft robots was recently demonstrated using soft 3D printed pneumatic bellows actuators arranged similar to a delta mechanism [26]. Such actuators have previously shown to have

linear behavior with pressure in the actuated direction [26], [27] making them good test cases to present the aforementioned modeling approach. Previous work on parallel 3D printed bellows actuation only analyzed active forces when the actuators were in their undeformed states [26]. The active and passive forces can be clearly distinguished as axial and shear forces respectively in this actuator, which makes force characterization relatively simpler. This also enables the validation of model's accuracy in position prediction by extending the model to parallel soft actuator networks.

1.2 Background

With the motivation of how soft robots and soft actuators are useful for various delicate tasks across multiple disciplines, we established the need for a simpler modeling approach for designing complex soft robots by characterizing the active and passive forces produced by a single, one degree-of-freedom soft actuator. In this section, we provide a strong overview of previous work on soft bellows actuators, and modeling techniques for soft robots.

1.2.1 Soft Bellows Actuators

Soft bellows actuators are soft actuators that use bellow-shaped geometry as chambers which can inflate or deflate based on designed stimuli, including but not limited to pneumatic [33], fluidic [34], electrostatic [35], and electromagnetic [36], [37] activation. Both of the hydraulics-inspired techniques enable actuation without the need for energized parts, unlike electrostatic and electromagnetic actuation. Additionally, pneumatic and fluidic bellows actuators scale well [26], [38] whereas the same is not necessarily true for electrostatic actuators in the millimeter to centimeter range [35] or outside the millimeter range for electromagnetic actuators [38]. In this thesis, we focus primarily on the soft pneumatic bellows actuator since they are good test cases for proving the effectiveness of the modeling approach presented in this thesis. The forces produced by these actuators can clearly be distinguished into their active and passive components, as the axial and shear forces respectively.

The actuation of the bellow chambers has been enhanced to develop soft actuators that can work as linear actuators that actuate actively in the axial direction, or as bending

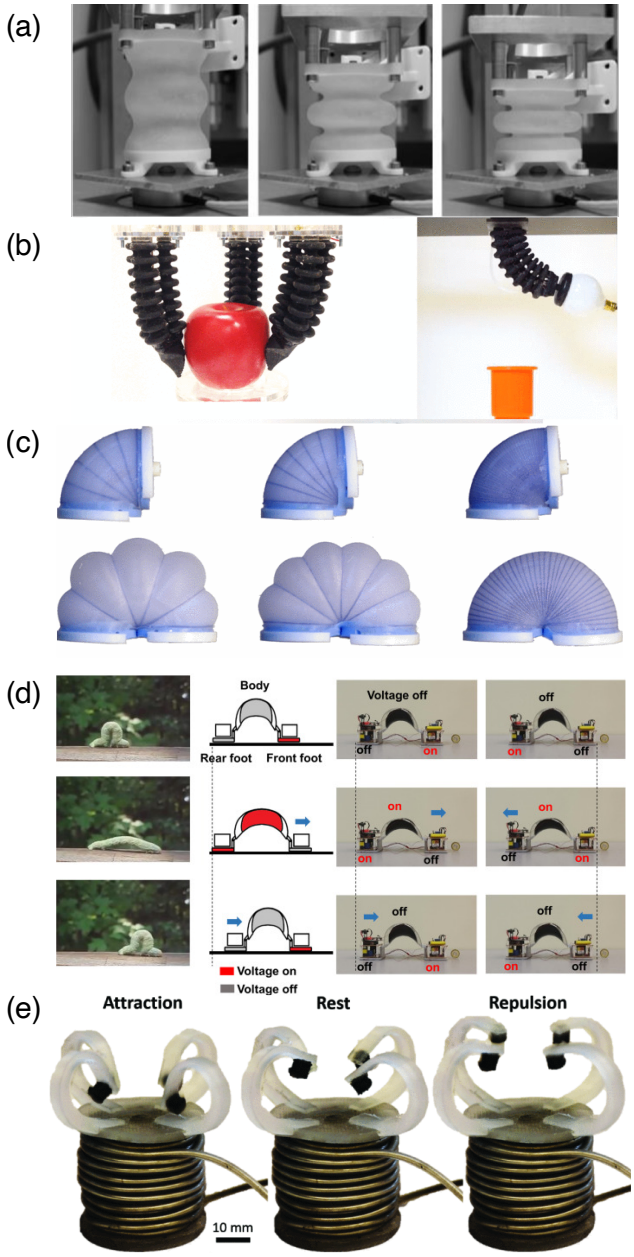

Figure 1.1. Various types of soft actuators presented in previous work. (a) Soft pneumatic linear bellows actuators under testing, from [28] ©IEEE 2018, (b) applications of soft 3D printed bending actuator module, from [29] ©IEEE 2019, (c) soft fluidic rotary actuator, from [30] ©IEEE 2017, (d) untethered locomotion robot using soft electrostatic actuators, reprinted from Extreme Mechanics Letters (2018) [31] with permission from Elsevier, and (e) attraction, rest, and repulsion configurations of the soft electromagnetic Xenia-inspired actuator, from [32] ©IEEE 2020.

actuators which actuate actively to create rotation [39]. The linear bellows actuators are generally designed to be axisymmetric around the actuation axis. This allows for nearly axial displacement of the actuator, even at higher displacement magnitudes. Asymmetry of the bellows about the actuation axis, on the other hand, leads to non-zero displacements normal to the actuation axis, creating bending motions. The bending actuators are designed for the asymmetry to achieve rotational motion. This asymmetry has been achieved in numerous ways such as having a semi-convolution about a flat plate such that the bellows are effectively on only one side of the flat plate. This results in the centroid being slightly shifted from the center of pressure [40], [41] and causes the bending action. Various bellow convolution profiles for both linear and bending actuators have been investigated including U-shaped, triangular and square [33], [40], [41], and each can be optimized based on geometric parameters to achieve desired elongation and force requirements.

With varying new ways of actuator mechanisms comes innovative manufacturing techniques. The most common ways are molding (2D and 3D), soft lithography, shape deposition manufacturing, thin-film manufacturing and 3D printing [42]–[45]. In this thesis, we focus on 3D printing techniques due to its rapid prototyping ability, ease of design replication, and design freedom for complicated geometries without need of additional processes [44]. There has been significant developments in soft materials for 3D printing, such as thermoplastic polyurethane-based (TPU) [46], silicone-based [47], biologically-inspired [48] or stimuli-responsive materials [49] which have expanded the use of 3D printing technologies in soft robotic fabrication [42]. Additionally, 3D printing provides the interesting ability to create multi-material parts by using multiple extrusion heads loaded with different materials. This opens up possibilities to create prototypes with soft deformable parts mixed with rigid elements, to pattern both materials to achieve intermediary compounds, or to create hybrid soft-rigid robotic systems [27], [44], [50]. However, 3D printing fabrication does come with drawbacks. The tensile strength of 3D printed soft materials is generally low [51] but with improvements in 3D printing machines, there are advances to improve the tensile strength of the materials [52], [53]. Design considerations also need to be made for the printer's size limitations and especially, for overhang geometries [44]. In this work, we employ 'vat polymerization' or more commonly known as stereolithography (SLA) techniques to achieve the

additive manufacturing process. This technique exploits the temporal and spatial control of light to selectively photopolymerize each layer of a solid object from a liquid pre-polymer. Additionally, holographic patterning is used to build entire objects in a single step which reduces cost and time. Such systems maintain a high resolution while being able to fabricate numerous parallel components [54].

1.2.2 Soft Modeling

One of the biggest challenges in soft robotics is modeling due to the high material and contact nonlinearities [55]. Numerous methods have been approached, both analytical and numerical. One of the common analytical approaches for soft pneumatic actuators is using piecewise constant curvature models for the kinematic modeling of soft continuum robots. Here, the robots can be considered of having a finite number of curved links which are described by arc parameters [23]. This method enables the kinematics to be decomposed into two mappings- actuator space to configuration space, which is robot-specific and describes constant curvature arcs. The other mapping is from configuration space to task space, which is robot-independent since it consists of a space curve describing position and orientation along a backbone, and is applicable to all systems that can be approximated as piecewise constant-curvature arcs [23], [56]. Despite the accuracy and usefulness of such models for continuum robots, it is not easily applicable to parallel actuator networks due to the increasing complexity as degree-of-freedoms increases. Other analytical models approximate the soft pneumatic actuator using a linear spring [26]. Here, a test-based approach is used to identify the linear behavior of the actuator in terms of its displacement and output force as separate tests when the actuator is pressurized. Consequently, a pressurized spring model is determined with experimentally fitted constants for slope, physically interpreted as the cross-sectional area for the pressure to act on, and the offsets, indicating the stiffness of the actuator at different lengths. This model is useful for behavior prediction of the actuator when working in axially actuated cases but are insufficient when the actuators are in shear orientations, which is likely in parallel actuator networks. Other common approaches use sophisticated theories such as Cosserat rods which include shear, extension, and rotational

inertia of the rod cross-section, unlike Bernoulli-Euler, to allow for all forms of deformation [57]. These are robust models when appropriately applied but are computationally expensive, making them cumbersome for preliminary design iterations, and challenging for real-time implementation.

Due to the challenges in obtaining analytical solutions to soft robotic systems, numerical methods are often used. Finite element modeling (FEM) is a commonly used numerical method. There have been multiple approaches ranging from using FEM in the design process [55], [58] to real-time control using asynchronous FEM [59] and reduced-order models [21], [60], [61]. Using FEM for soft robots is challenging due to the multiple nonlinearities, including geometric, material, and contact [55]. A large focus of FEM in soft robotics is on material modeling using various hyperelastic models such as Neo-Hookean, Mooney-Rivlin, Yeoh, and Ogden [21], [58], [62]. Experimental testing is performed using material samples and the data is fit to these models to obtain the relevant parameters for use in the FEM softwares. To achieve real-time control using asynchronous FEM, complex computations such as accurate FEM deformations are performed at low frequency whereas the control is performed at high frequency using strong real-time constraints [59]. In the reduced-order models, a set of expensive, whole model simulations are performed offline, and then snapshot-proper orthogonal decomposition (POD) is applied for a posteriori analysis to provide optimal functions and reduce the number of state variables [21]. A proper generalized decomposition (PGD) approach is employed in [60] where the learning campaign is not necessary since the optimal functions are computed a priori. The FEM simulations can be done using commercially available software such as ABAQUS or ComSol, but they rely on a good understanding of physical modeling. Additionally, the cost of their precision is the slow computation speed and suitability for only offline simulations [63]. To model for real-time online simulation, [63] presents the open-source framework SOFA which is founded upon continuum mechanics for material modeling, constraint solving using Lagrangian multipliers, and Signorini's law of contacts. Despite the high accuracy promised through FEM simulations, offline and real-time, they rely heavily on case-specific simulation setup, and require significant time and testing for verification prior to obtaining useful results. Thus, it may not be most time-efficient for preliminary design iterations to ensure performance requirements are met before

fabrication of samples. The work presented in this thesis overcomes this drawback by presenting a simplified modeling approach which can be used to ensure adequate performance in a more time-efficient manner for preliminary designs.

1.3 Outline

In this thesis, we build a combined axial and shear forces model for a 3D printed bellows actuator that can be used to predict the behavior of parallel actuator networks. We do this by first, discussing the design and manufacturing of a soft pneumatic actuator for haptic applications, and then present a model that relates the inlet pressure and actuator geometry to the output forces in Chapter 2. Thereafter, we design and manufacture a static test setup to characterize the one DOF soft actuator in Chapter 3. Here, we measure the force output of the pressurized actuator as it is statically deformed. The obtained experimental results are qualitatively and quantitatively analyzed by comparing them to the presented model, and fitting for model constants. Based on this characterization, we describe how this model can be used for predicting parallel combinations of actuators and compare previous work to presented model using experimental results from a soft parallel delta mechanism with three independent actuators and a floating actuator mechanism with five independent actuators in Chapter 4. Finally, we conclude with a summary of the contributions of this thesis and recommendations for future work in Chapter 5.

2. DESIGN AND MODELING OF SOFT PNEUMATIC ACTUATOR

The first step to understanding the behavior of multiple degree-of-freedoms (DOFs) soft actuator parallel networks is to study their one degree-of-freedom components, the 1-DOF actuator. Previous work has primarily focused on active (axial) actuation which may not be sufficient when modeling the complex movement and force profiles of soft parallel networks. In this chapter, we present a new approach to such modeling by characterizing both active (axial) and passive (shear) forces at the 1-DOF actuator. In order to do this, we start with motivating the actuator design for haptic applications and its manufacturing process, and then derive a mechanical model for the force profiles using parallel linear and torsional springs. Portions of this chapter have been presented in [64] ©IEEE 2022.

2.1 Soft Pneumatic Actuator Design and Manufacturing

In a one-dimensional soft pneumatic actuator, the key requirements we seek are the creation of forces and displacements in magnitudes of Newtons and millimeters respectively which is in line for haptic applications [65], linear behavior of forces to pressure for simple characterization, and the ability to pneumatically drive the actuator for easy implementation without the risk of hydraulic spillage or need for controlled environments such as clean rooms. Soft bellows actuators provide good flexibility in adjusting design parameters and number of convolutions to achieve desired forces and displacements. Three-dimensional (3D) printed bellows actuators have shown to be highly linear in their behavior towards air pressure and stiffness [26], [27]. Pneumatically driven soft bellows actuators convert air inlet pressure into material bending to extend and consequently, exert force at its ends [26]. These forces can be classified easily into their active and passive components as axial and shear directions of force. Since they meet all design requirements set forth earlier, soft bellows actuators make for good one-dimensional soft pneumatic actuator for the purposes of this work.

We employ 3D printing methods using a Formlabs Form 3 SLA (stereolithography) Printer to realize the designed actuator. 3D printing is beneficial for rapid prototyping

of actuators and offers a less laborious manufacturing method without significant impact on repeatability, as compared to other methods such as replica molding [66], [67] or rotational casting [52] which require intricate mold design, preparation, or an expensive system setup for each design change. Additionally, 3D printing has the benefit of easier construction of parallel structures which are the primary focus of this work. However, upside-down SLA printing, like in the Form 3, does come with its drawbacks which need to be accommodated for in the actuator design. It is recommended to not print enclosed parts without drain holes, to avoid cupping blowout failures during printing. Moreover, the Form 3 is unable to print multi-material parts like the Polyjet printers in [27]. Therefore, for a successful design, the actuator assembly consists of four parts: a soft bellows actuator, two rigid caps (one at each end) and a flexible plug.

The soft pneumatic actuator model, shown in Figure 2.1, has a bellow-shaped profile, inspired by the actuator shapes of previous work [27]. [27] presents an optimized geometry for a bellows profile for force requirements of 12 N by using maximum (logarithmic) principal strain, $\epsilon_{ln,max}$, as a fatigue life indicator. However, we simplify the dimensions to maintain a constant bellows thickness and four "half-waves" in the bellows profile (shown in Figure 2.3) for manufacturability and modeling simplicity. Values for the dimensions of the prototype actuator are shown in Table 2.1 (from [64] ©IEEE 2022). It is printed using the Elastic 50A resin by Formlabs which has an ultimate tensile strength of 3.23 MPa and 160% elongation at failure post cure [68].

Table 2.1. Dimensions of Prototype Actuator (Figure 2.1(a))

Actuator dimension	**Size(mm)**
a	R1.50
b	R3.00
c	2.00
d	18.00
L_0	18.50

Figure 2.2 helps visualize the interface geometry between the barbed air inlet, flexible plug, rigid cap and actuator better. The actuator has flanges of 3 mm on both ends to aid in

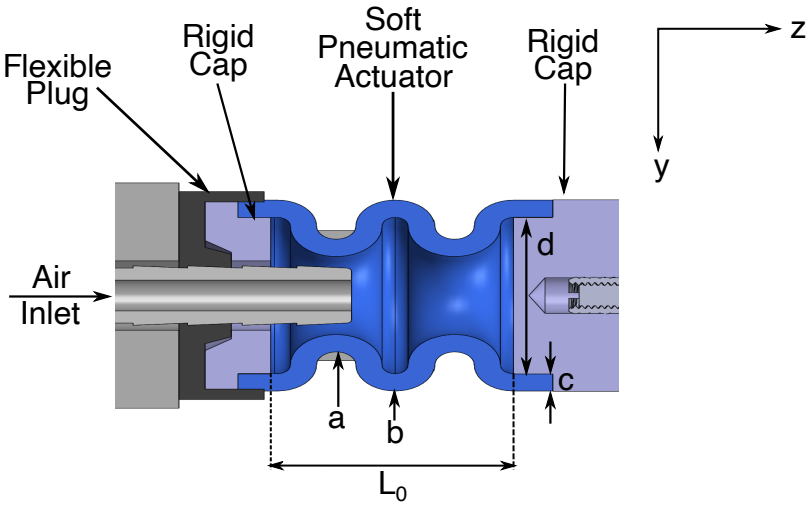

Figure 2.1. Soft pneumatic bellows actuator profile with marked dimensions (refer to Table 2.1). This profile maintains a uniform wall thickness throughout the actuator and is symmetric about the vertical axis for uniform force application at both ends. The natural length, L_0, corresponds to the resting effective length of the "soft" portion of the actuator and doesn't include the flange ends on both sides which interface with the rigid caps. Modified from [64] ©IEEE 2022.

assembly with the rigid caps. The caps ensures uniform force application and secure joints with the soft actuator material. It is printed using the Clear resin by Formlabs which has an ultimate tensile strength of 65 MPa and elongation of 6.2% at failure post-cure [69]. Its geometry allows for a through hole of radius 4.76 mm for the barbed air inlet fitting at one end, while maintaining a diameter 0.10 mm larger than the bellow actuator's inner diameter of 18 mm for the flange's length and equal to the actuator's outer diameter of 20 mm for the remainder of its width, at both ends. Such mating geometry reduces air gaps while still enabling hand assembly, and the compliant nature of the soft material permits such interference fits. To completely seal the cap-actuator interface, a flexible epoxy adhesive (DP110 Clear, 3M) is applied on the mating surfaces and held under compressive load for more than 10 minutes. Initially, a super glue (Ultra Gel Control, Loctite) was used at the mating interfaces, however the joints formed were too rigid and couldn't withstand the higher

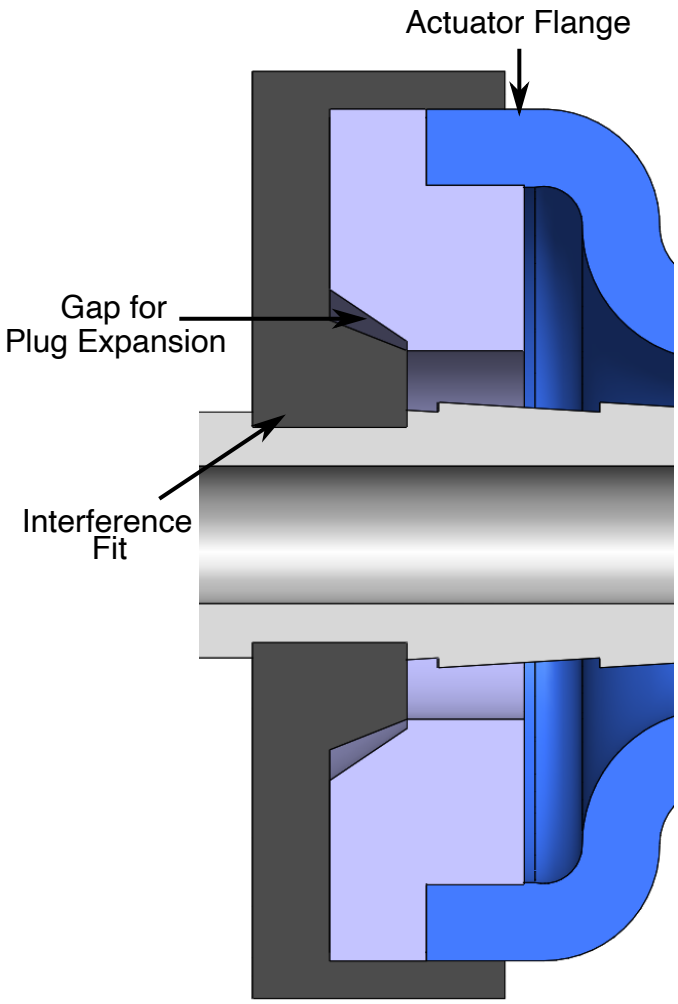

Figure 2.2. Focused cross-section model representation of the interface between the barbed air inlet, flexible plug, rigid cap and actuator showing the transition fits.

orientation angles during testing. Using the flexible epoxy adhesive mitigates this issue with negligible change in actuator performance.

Even though the air gaps around the cap-actuator interface have been addressed, the through hole in the rigid cap for the barbed inlet is still a source of air leak. Hence, the flexible plug is designed to be on top of the rigid cap, acting as the primary interface to the barbed air inlet fitting. As the name suggests, this plug is made of a flexible material which enables it to have an interference fit with the air inlet fitting and can still be assembled by

hand, to ensure hermetic assembly. It is printed using the Flexible 80A resin by Formlabs which is a stiffer resin as compared to the Elastic 50A with an ultimate tensile strength of 8.9 MPa and elongation of 120% at failure post-cure [70]. This allows for a comparatively stiffer interface at the air inlet end, while still preserving the flexible nature of this component. The plug also interfaces with the rigid cap through a plug-like geometry to appropriately transfer loads to the rigid cap. To allow for proper assembly amidst the interference fits, there is an intentional gap at the plug-like interface to allow for the flexible plug to displace as the barbed inlet air fitting is inserted. This reduces stresses on both the flexible plug and rigid cap, and makes assembly easier. Additionally, it has mating flanges extending along the cap's and actuator's circumferences to further mitigate air leaks at the cap-actuator interface. All the interfaces for the flexible plug to the rigid cap are completely secured

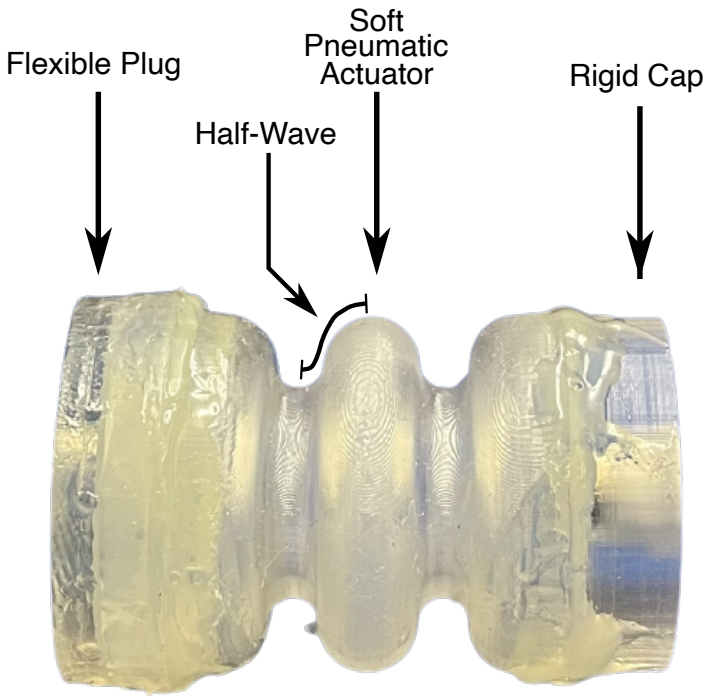

Figure 2.3. Realized soft pneumatic actuator assembly. The rigid cap is labeled only on one end since the rigid cap on the air inlet end is covered by the flexible plug. One can also see the cured flexible epoxy adhesive used at the interfaces to ensure hermetic assembly.

through the flexible epoxy adhesive (DP110 Clear, 3M). The realized actuator assembly is now airtight and is presented in Figure 2.3.

2.2 Model

Another crucial step before characterization testing of the actuator designed in Section 2.1 is the derivation of a theoretical model that attempts to explain the actuator forces upon pressurization and deformations in the axial, F_z, and shear, F_y, directions. Previous work using a lumped parameter approach has only considered the linear stiffness of soft actuators [26], but that may not be sufficient when modeling passive deformations in unactuated directions. There have also been more complex modeling approaches to explain the dynamic behavior of soft continuum robots using non-linear Cosserat beams [71], but it is time consuming to formulate and requires numerical solution techniques, which is not a time-efficient way for preliminary design iterations. We attempt to bring forth a simplified lumped parameter modeling approach using a pressurized piston, and linear and torsional springs in a parallel arrangement to characterize the actuator forces and deformations under the assumptions of static equilibrium.

To begin, we divide the axial and shear forces into pressure-based forces, $F_{z,P}$ and $F_{y,P}$, defined as the force generated from pressurization of the soft bellows actuator, and static offset forces, $F_{z,0}$ and $F_{y,0}$, defined as the force at zero inlet pressure, i.e. the force generated due to the bellows actuator deformation alone. We combine these forces linearly following the principle of superposition:

$$F_z = F_{z,P} + F_{z,0} \tag{2.1}$$

$$F_y = F_{y,P} + F_{y,0}. \tag{2.2}$$

Since, in general, the relationship between pressure and force is linear based on area (i.e. $F = PA$ from Pascal's Law), these equations can be rewritten:

$$F_z = PA_{z,\text{eff}} + F_{z,0} \tag{2.3}$$

$$F_y = PA_{y,\text{eff}} + F_{y,0}. \tag{2.4}$$

where P is the air inlet pressure and $A_{z,\text{eff}}$ and $A_{y,\text{eff}}$ are the effective cross-sectional areas in axial and shear directions respectively. This leads to the force models being linear in pressure, with the slope based on effective area and the intercept based on the static offset force due to the bellows actuator's deformation. The bellows actuator's geometric deformation in the y-z plane can be completely parameterized by its change in effective length, $\Delta L = L$ - L_0, where L is the actuator's effective length along the axis of the actuator's soft portion post deformation, and its orientation angle, θ, which is the angle measured from the z-axis to the axis of the actuator's soft portion, as shown in Figure 2.4(a). In the remainder of this section, we describe the models for effective areas and static offset forces as functions of ΔL and θ. As a note, all equations in this section compute the shear angle in radians.

2.2.1 Pressure Forces Model

The pressure forces act on the soft bellows actuator through the internal surface area. Under pure axial deformation, this can be modeled as a simple pressurized piston, i.e. only forces in the axial direction. This model results in:

$$F_{z,P}(P) = PA_{z,\text{eff}} \tag{2.5}$$

Since the axial effective area, $A_{z,\text{eff}}$, is based on the rigid cap geometry of the bellows actuator, neither axial nor shear deformation will affect the pressure force in the axial direction.

In the shear force direction, the majority of the pressure forces cancel out due to the rotational symmetry of the bellows. Under pure axial deformation (i.e. orientation angle, $\theta = 0$ degrees), this means that the shear effective area, $A_{y,\text{eff}}$, will be zero since the forces acting on the walls of the actuator are equal and cancel each other out as visualized in Figure 2.4(b). However, under shear deformation when $\theta \neq 0$ degrees, a non-zero shear effective area will result from the deformed geometry as shown in Figure 2.4(c). The width of the actuator leads to the outer edge lengthening more than the inner edge, hence creating

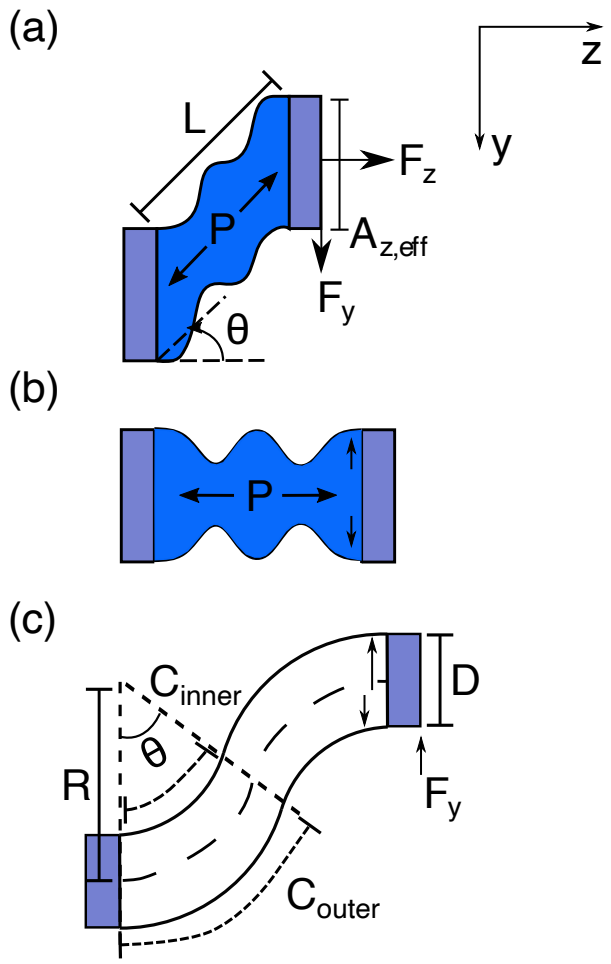

Figure 2.4. Geometry of the pneumatic bellows actuator under axial and shear deformations. (a) Bellows actuator under axial and shear deformations, showing respective forces and physical meaning of $A_{z,\text{eff}}$ and $A_{y,\text{eff}}$. (b) Centerline deformation used to generate models for axial and shear forces. Centerline approximately forms two circular arcs perpendicular to the rigid end-caps. Modified from [64] ©IEEE 2022.

a non-zero shear pressure force acting in the negative y- direction. This can be described by the following equation:

$$C_{\text{outer}} - C_{\text{inner}} = \theta\left(R + \frac{D}{2}\right) - \theta\left(R - \frac{D}{2}\right) = \theta D \tag{2.6}$$

where $C_{\text{outer}} - C_{\text{inner}}$ is the length difference between outer and inner edges, R is the radius of curvature the bellows actuator makes when sheared, and D is the width of the cylindrical

approximation of the actuator. The difference in area for the pressure to act on between the outer and inner edges of the actuator result in a net pressure force in the negative y-direction (direction of shear) for a positive shear angle, as per the axes defined in Figure 2.1, given a constant internal pressure, P, from the air inlet. This difference in area is proportional to the angle of shear, θ, and hence the magnitude of shear pressure force, F_y, would increase with greater shear angles. Since the actual area change is complex and based on the shape of the bellows actuator, we will fit a proportional constant, $W_{y,\text{eff}}$, where $A_{y,\text{eff}} = W_{y,\text{eff}}\theta$, using experimental data. This results in the shear pressure force model as:

$$F_{y,P}(P,\theta) = -PA_{y,\text{eff}} = -PW_{y,\text{eff}}\,\theta \tag{2.7}$$

As a note, the negative sign is added to account for the direction of shear pressure force, given the axes defined in Figure 2.1.

2.2.2 Static Offset Forces Model

The static offset forces are modeled as a linear and torsional spring in parallel based on the deformation of the elastic bellows material (Figure 2.5(a)). Previous work only considered the linear stiffness of the soft actuator [26], but we add the torsional spring to better account for the shear behavior. We describe the derivation for the linear spring force, $\vec{F}_{0,s}$, and the torsional spring force, $\vec{F}_{0,t}$, separately below.

The force due to the linear stiffness of the actuator, $\vec{F}_{0,s}$, will act in the direction of extension and be proportional to the length change along the center axis, ΔL, as shown in Figure 2.5(b), resulting in a force magnitude of:

$$\left|\vec{F}_{0,s}\right| = k_s|\Delta L| \tag{2.8}$$

where k_s is the linear spring stiffness of the actuator.

The torsional spring component is in parallel to the linear spring and is assumed to undergo an angular deflection equivalent to the shear angle, θ, of the soft actuator. Consequently, it is modeled to have a free position of 0 degrees such that there is no contribu-

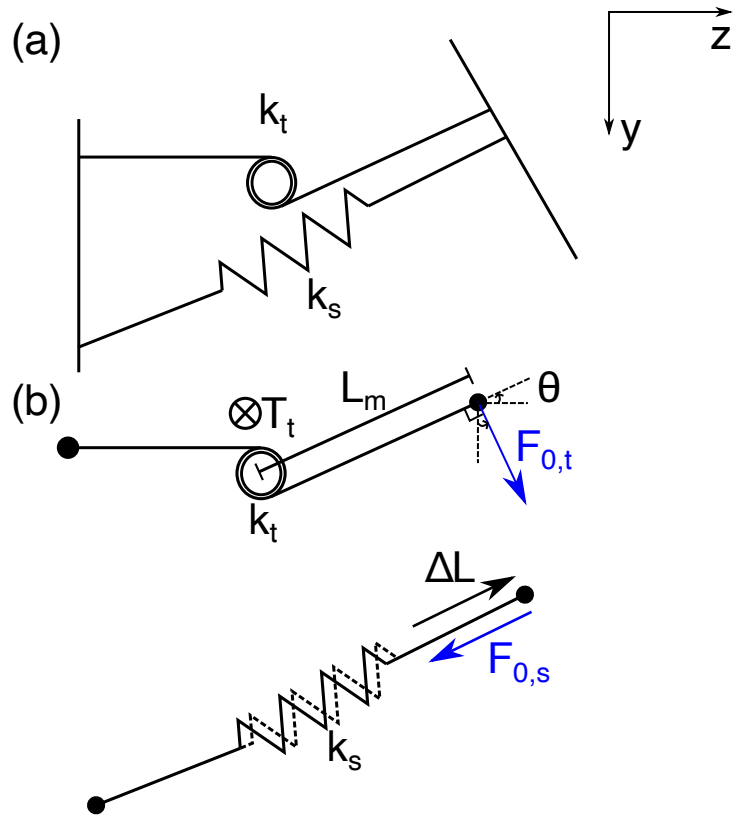

Figure 2.5. Static offset forces model which depend entirely on the actuator's orientation and is independent of air inlet pressure, P (a) Parallel linear and torsional spring model used to derive static offset forces. (b) Force balance of each component in (a). Modified from [64] ©IEEE 2022.

tion of the torsional spring force, $\vec{F}_{0,t}$, when the actuator is in a pure axial configuration with $\theta = 0$ degrees.

When the actuator is not in a pure axial configuration, the torsional spring generates a moment based on the angle of shear, which can be equated to a force that acts perpendicular to the direction of extension, using the moment arm as shown in Figure 2.5(b). The magnitude of the torque will be:

$$\left|\vec{T}_t\right| = L_m \left|\vec{F}_{0,t}\right| = k_t|\theta| \tag{2.9}$$

where $\vec{T}_t$ is the torque generated by the torsion spring due to its deformation, L_m is the moment arm from the torsion spring to the rigid end cap and k_t is the torsional spring stiff-

ness. For simplicity, we assume that the moment arm, L_m, remains approximately constant, neglecting the effects from the length change of the bellows actuator. As a result we have:

$$\left|\vec{F}_{0,t}\right| = \frac{\left|\vec{T}_t\right|}{L_m} = \frac{k_t|\theta|}{L_m} \tag{2.10}$$

The total force for the combined static offset forces system is now of the form:

$$\vec{F}_0 = \vec{F}_{0,s} + \vec{F}_{0,t} \tag{2.11}$$

This can now be separated into its shear and axial components based off the shear angle, θ, yielding:

$$F_{z,0} = -k_s \Delta L \cos(\theta) + (k_t/L_m)\theta \sin(\theta) \tag{2.12}$$

$$F_{y,0} = k_s \Delta L \sin(\theta) + (k_t/L_m)\theta \cos(\theta) \tag{2.13}$$

Here, the sign convention based on the defined coordinate system has been factored in. For a positive shear angle, the linear spring force resolves in the negative z-direction and positive y-direction whereas the torsional spring force resolves in the positive y- and z-directions.

Additionally, we can simplify the model using small angle approximation since the expected operating range is usually within $\theta = 0°$ to $\theta = 30°$ (0.52 radians):

$$F_{z,0} \approx -k_s \Delta L + k_\theta \theta^2 \tag{2.14}$$

$$F_{y,0} \approx k_s \Delta L \theta + k_\theta \theta \tag{2.15}$$

where k_θ, coined as torsional factor, is equal to the torsion spring stiffness, k_t, divided by the magnitude of the moment arm, L_m.

2.2.3 Superposition of Pressure and Static Offset Forces Model

With the pressure and static offset forces characterized in Sections 2.2.1 and 2.2.2, we can combine them using the principle of superposition to obtain the complete model in Equations 2.16 and 2.17.

$$F_z = PA_{z,\text{eff}} - k_s \Delta L + k_\theta \theta^2 \tag{2.16}$$

$$F_y = -PW_{y,\text{eff}}\theta + k_s \Delta L \theta + k_\theta \theta \tag{2.17}$$

Here, we can identify few trends on how we can expect the actuator forces in both axial and shear directions to behave as it is deformed. First, we can see that the axial forces increase whereas the shear forces generally decrease as the actuator is pressurized for a given actuator configuration. However if the shear angle is zero, the air inlet pressure has no direct impact on the shear force, F_y, exerted by the actuator. Additionally, we can see that the axial forces increase quadratically as the shear angle increases, signifying the contribution of the torsional spring in predicting actuator forces. The shear forces vary linearly to θ. A deeper look at Equations 2.16 and 2.17 suggest that there are non-trivial configurations where the axial and/or shear forces can be zero! These can be interesting configurations in the application workspace of these soft pneumatic actuators. Finally, we can also identify the linear relationship of ΔL to both forces, and we'd expect the axial forces to decrease and the shear forces to increase with an increase in actuator length.

In this chapter, we presented a detailed design for the soft pneumatic actuator along with its motivation. We also discussed the manufacturing and assembly process for each component in the actuator. Thereafter, we derive a pressurized piston, and parallel linear and torsional springs model to characterize the forces exerted by the actuator. In the next chapter, we will present a testing method and strategy for the soft actuators, and analyze the validity of the presented model when compared to experimental results.

3. STATIC TEST DESIGN, METHODS, AND ANALYSES

In Chapter 2 we established the need, consequent design, and mechanical model for a 1-DOF soft 3D-printed actuator. In this chapter, to prove the validity of the model, a static test is designed to measure the axial and shear forces exerted by the actuator at different configurations. Thereafter, the acquired data is analyzed to investigate the correlations and obtain the linear spring stiffness, k_s, and the torsional factor, k_t, for the designed soft actuator. This also enables us to quantify the losses in accuracy due to the modeling assumptions of small angle deformations, and constant torsional moment arm made in Chapter 2. Portions of this chapter have been presented in [64] ©IEEE 2022.

3.1 Static Test Fixture Design

To begin the test fixture design, it is important to establish the input parameters to the test setup and the desired output variables. Since we derive the model primarily in terms of the actuator's change in effective length, ΔL, orientation angle, θ, and air inlet pressure, P, these are the optimal input parameters to the test system. Similarly, since axial and shear forces are characterized for the soft actuator, these are the desired output variables. For static testing of the actuator, the tests are to be performed at a fixed actuator length, L, and shear angle, θ, for a particular sample as the air inlet pressure, P, is varied while the "blocked forces" in the axial and shear directions are measured. In Sections 3.1.1, 3.1.2 and 3.1.3, we will discuss design considerations and measurement strategies for the input parameters, output variables, and additional considerations respectively.

3.1.1 Design for Input Parameters

Actuator's length, L, and shear angle, θ, can be visualized as the actuator's end-effector positional representation in the polar coordinate system. Therefore, one can easily convert them to the Cartesian coordinate system and still achieve desired actuator parameters. Recognizing this allows us to vary horizontal, z-, and vertical, y-, positions on a test fixture in order to set L and θ. The coordinate frames are as established in Chapter 2. To prevent

unintentional out-of-plane movements during test setup, facilitate easy adjustments, and enable abundance of mating components, 20 mm T-slotted aluminum framing with a single four slot rail are used as rails, and are held perpendicular to each other using a 90° gusset. During preliminary testing trials, it was identified that the gusset itself is not sufficient to limit movement of the vertical rail upon actuator pressurization. Hence, 3D printed brackets were manufactured to secure the perpendicular rails. The rails, gusset, and brackets arrangement is shown in Figure 3.1.

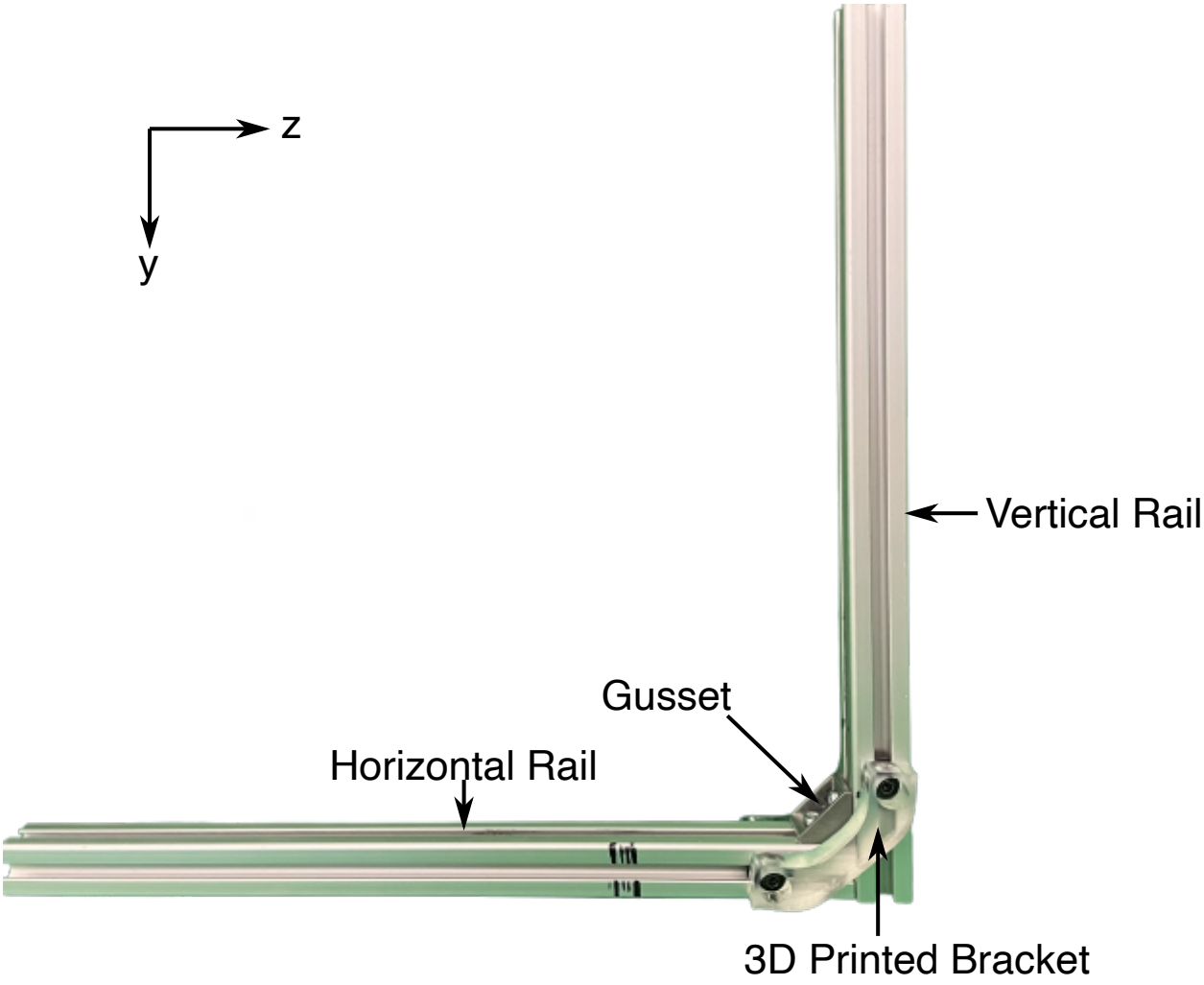

Figure 3.1. Horizontal and vertical rails design using T-slotted aluminum framing, 90° gusset and 3D printed brackets to enable z- and y- positioning to define actuator configuration, and to create normal sliding guides for supports.

The next step towards a robust fixture is to design supports for both ends of the actuator. Since blocked force measurements are desired, the supports need to be in a "fixed" configuration for each experiment, but must be able to slide along their respective rails when adjustments are needed. Hence, two supports, horizontal and vertical, are designed which slide on the horizontal and vertical rails respectively. The horizontal support is attached to the air inlet end for assembly ease. The requirements of this support is to house the air inlet nozzle, support any reactions from pressurization, and determine the horizontal component of the actuator configuration. A counterbore hole of counterbore diameter 17.50 mm, depth of 11 mm and pilot diameter 8 mm is modeled to house the air inlet nozzle, based on the purchased nozzle's dimensions. The pilot hole, housing the nozzle tip, has a clearance fit whereas the nozzle body, housed in the counterbore has a transition fit such that the frictional contact between the nozzle body and support is sufficient for reactions affecting this mating contact. To secure the horizontal support to the rails setup, end-feed fasteners are used. Using such a fastening method also allows the supports to slide for adjustment when the fasteners are loose, but act as fixed joints when the fasteners are tightened up using an allen wrench. After preliminary testing, slots are added to the horizontal support for securing the C-clamp attachment, which is discussed in more detail under Section 3.1.3. The CAD model and the realized horizontal support are shown in Figure 3.2. The nozzle tip is inserted to the flexible cap end of the actuator to create a hermetic air inlet.

Next, the vertical support is designed. Similar to its horizontal counterpart, it needs to be fixed during an experiment and retain its slidability for adjustments in between experiments to achieve desired actuator lengths and orientation angles. To do this, a similar approach for fastening is taken where the vertical support's base is secured to the vertical rail using end-feed fasteners. While the horizontal support acts as the air inlet end, the vertical support must mount a force/torque (F/T) transducer to measure the blocked forces exerted by the actuator. More details of the F/T transducer are discussed in 3.1.2 but for the purposes of vertical support to transducer interface, only the mounting side bolt pattern is of relevance. According to the transducer's technical drawing [72], there are two mounting options. Using two 3 mm diameter slip fit interfaces, or three equally spaced M3x0.5 mounting interfaces, both with 5 mm maximum interface depth. Due to the abundance of M3 screws of various

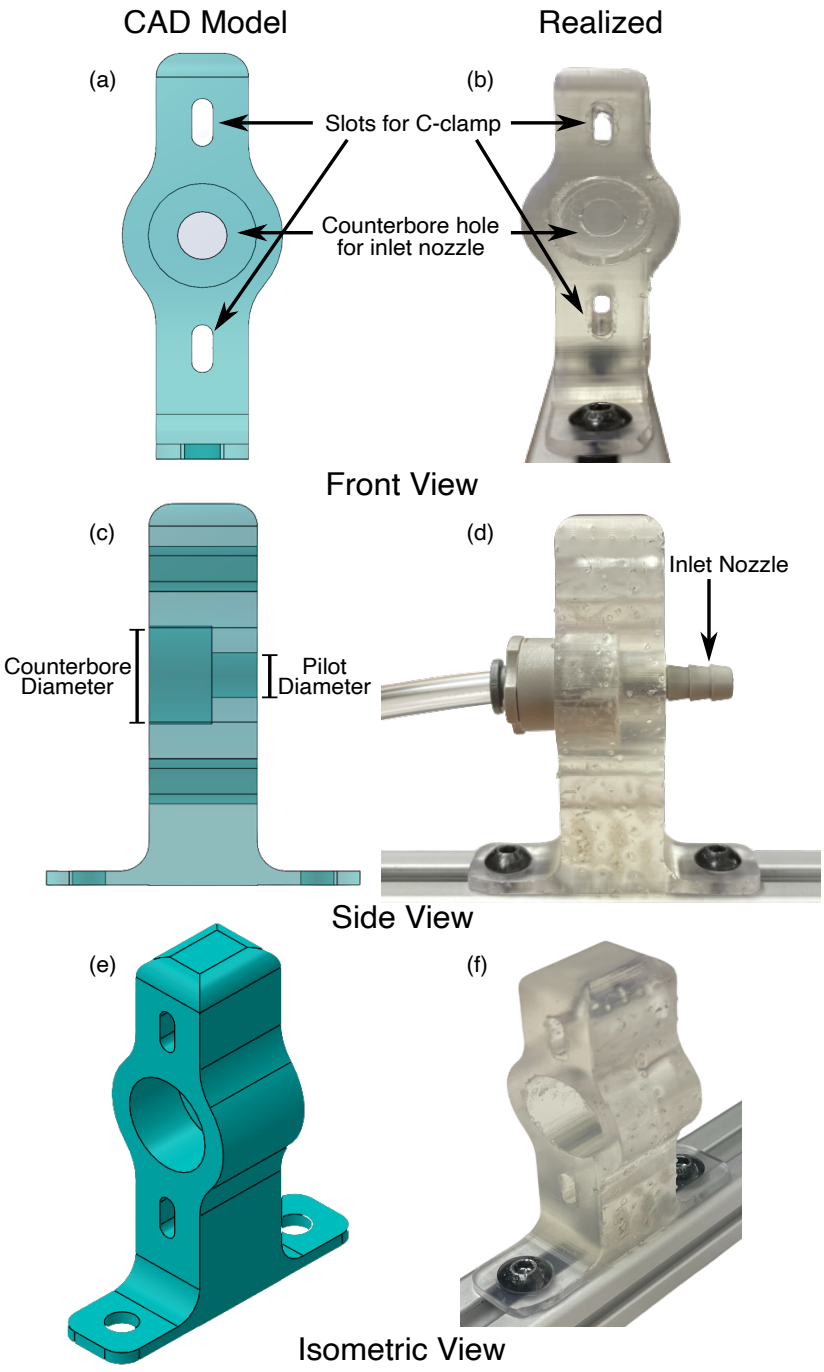

Figure 3.2. Horizontal support's CAD model and manufactured component. (a) and (b) show the front view, (c) and (d) present the side view, and (e) and (f) display the isometric view of the support.

lengths, and relative ease of screw assembly design as compared to slip fit assembly, the three M3 mounting interfaces were chosen. On the vertical support, a mounting plate is designed with its normal, or area vector, parallel to the horizontal (z-) axis. With a thickness of 6 mm, this plate has two M3 countersunk through holes with a head clearance of 2.50 mm, and a M3-sized countersunk through slot of length 6 mm, and head clearance of 2.50 mm to mate with the mounting side of the F/T transducer using three M3 screws of length 8 mm. The countersunk slot is added to the geometry to ease assembly by providing a larger assembly tolerance. The support has a 20 mm long neck that joins the mounting plate to the support's 36 mm long, 15 mm wide and 2.5 mm thick base. The CAD model and the realized vertical support are shown in Figure 3.3. In the first iteration of the vertical support, the end-feed fasteners were added to the same side of the support's neck which resulted in non-negligible support movement when the actuator is tested in an elongated configuration ($\Delta L > 0$), in addition to making it difficult to tighten the fasteners upon adjustment. The tool access concerns could be addressed by elongating the neck, however that would only worsen the support movement condition. Hence, the new iteration involved end-feed fasteners on both ends, and longer neck to minimize both concerns.

Both supports are 3D printed using the Formlabs Form 3 printer with the clear resin due to its rigid material properties, making it suitable for the supports designed. Next, the actuator and transducer interface is to be designed such that the output variables, axial and shear forces, are accurately measured.

3.1.2 Actuator-Transducer Interfacing Design

The horizontal support ensures a rigid assembly at the air inlet end through it's design, however, the vertical support must appropriately interface with the F/T transducer while maintaining a rigid assembly as well, to get meaningful blocked forces measurements. The F/T transducer used is the Mini40 Multi-Axis F/T Transducer (ATI). This particular transducer is calibrated for ± 120 N in the axial direction with 95% measurement uncertainty of 0.75%, and ± 40 N in the shear directions with 95% measurement uncertainty of 1.25% [73]. The high accuracy of this sensor increases the reliability of test measurements, and eliminates

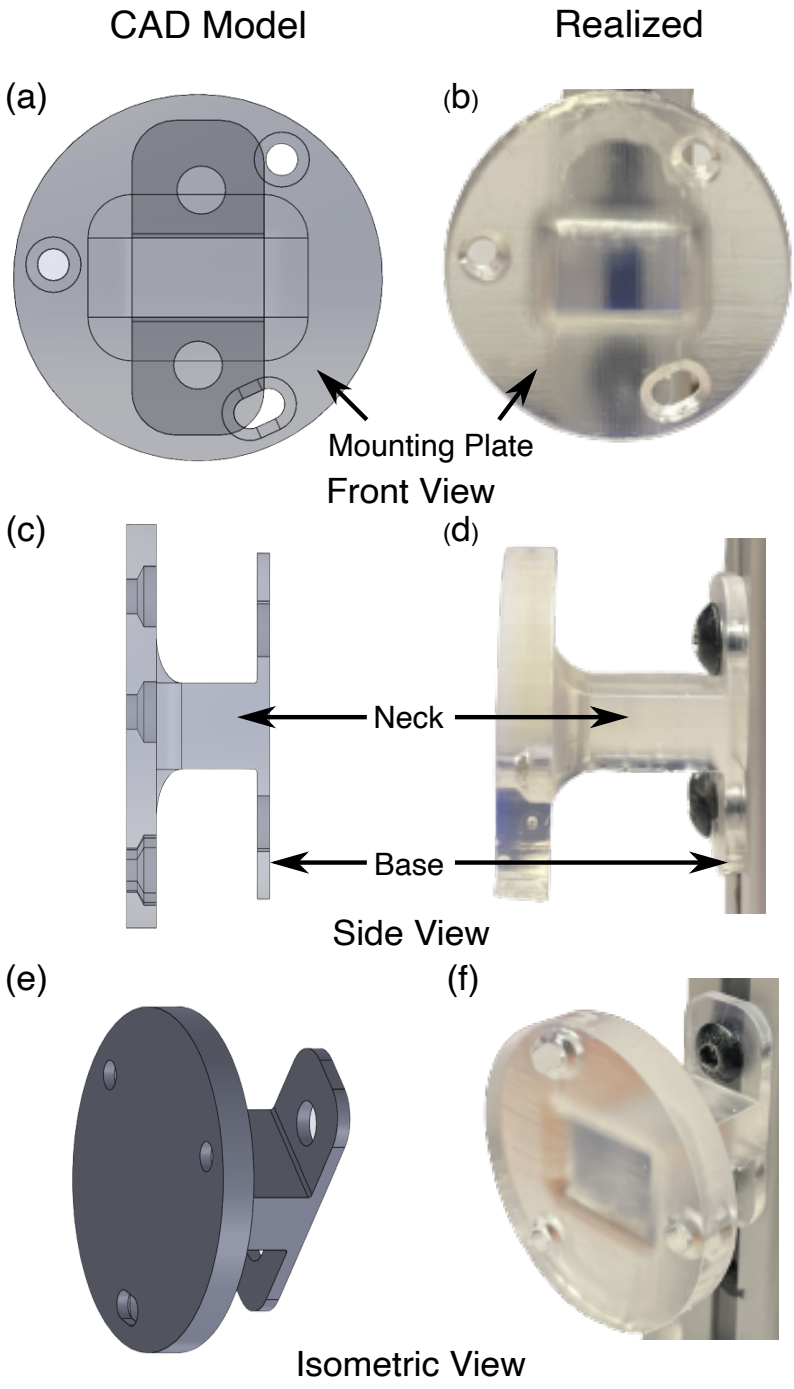

Figure 3.3. Vertical support's CAD model and manufactured component presented with a front view, (a) and (b), side view, (c) and (d), and isometric view, (e) and (f).

the need for external signal processing in this application. From the technical drawing [72], it is noted that the tool side, here actuator side, can be mounted using three equally spaced M3x0.5 tapped holes, similar to the mounting end, but with a maximum interface depth of 3 mm. Additionally, these holes lie on a circle of diameter 33 mm. The actuator designed in 2.1 has a rigid end cap of diameter 22 mm. Therefore, an adapter plate needs to be designed to transfer the forces onto the sensor.

The key requirements for the adapter plate is to be sufficiently rigid such that the exerted forces are transferred to the F/T transducer with minimal losses due to material deformation, and no relative rotation with respect to the actuator to avoid inaccurate readings. Firstly, we decide to 3D print this part using the clear resin material to achieve the needed rigidity, and to maintain the ability to rapidly prototype a custom design. Moving on to the component design, the adapter plate must interface with the F/T transducer at one end, and the pneumatic actuator at the other. The plate itself is designed to have a thickness of 5.50 mm, to accommodate interface depth constraints of the transducer. At the F/T transducer end, the adapter plate has a similar bolting pattern with two countersunk through holes and one countersunk through slot but with head clearances of 0.25 mm, such that M3 screws similar to the vertical support assembly can be used.

At the actuator end, the design is more involved. This is because the interface mechanism needs to be sufficiently strong to withstand the pressure and static offset forces, and also preserve the hermetic nature of the soft actuator. Using flexible epoxy or super glue would not be sufficient since the repeated actuation through multiple tests could weaken the adhesiveness, and could give skewed force readings. Therefore, a screw interface is decided upon. This is achieved by using a heat-set M3 threaded insert at the rigid cap of the actuator and designing a countersunk through hole at the adapter plate with a head clearance of 1.50 mm such that the 8 mm long M3 screw would have sufficient thread engagement with the threaded insert. To allow a heat-set threaded insert, the rigid cap of the actuator on the transducer end is made slightly thicker, now 9 mm, to accommodate a hole of diameter 4.10 mm with a depth of 6.60 mm per the specifications of the insert. The CAD models of the adapter plate, and its interfaces are shown in Figure 3.4.

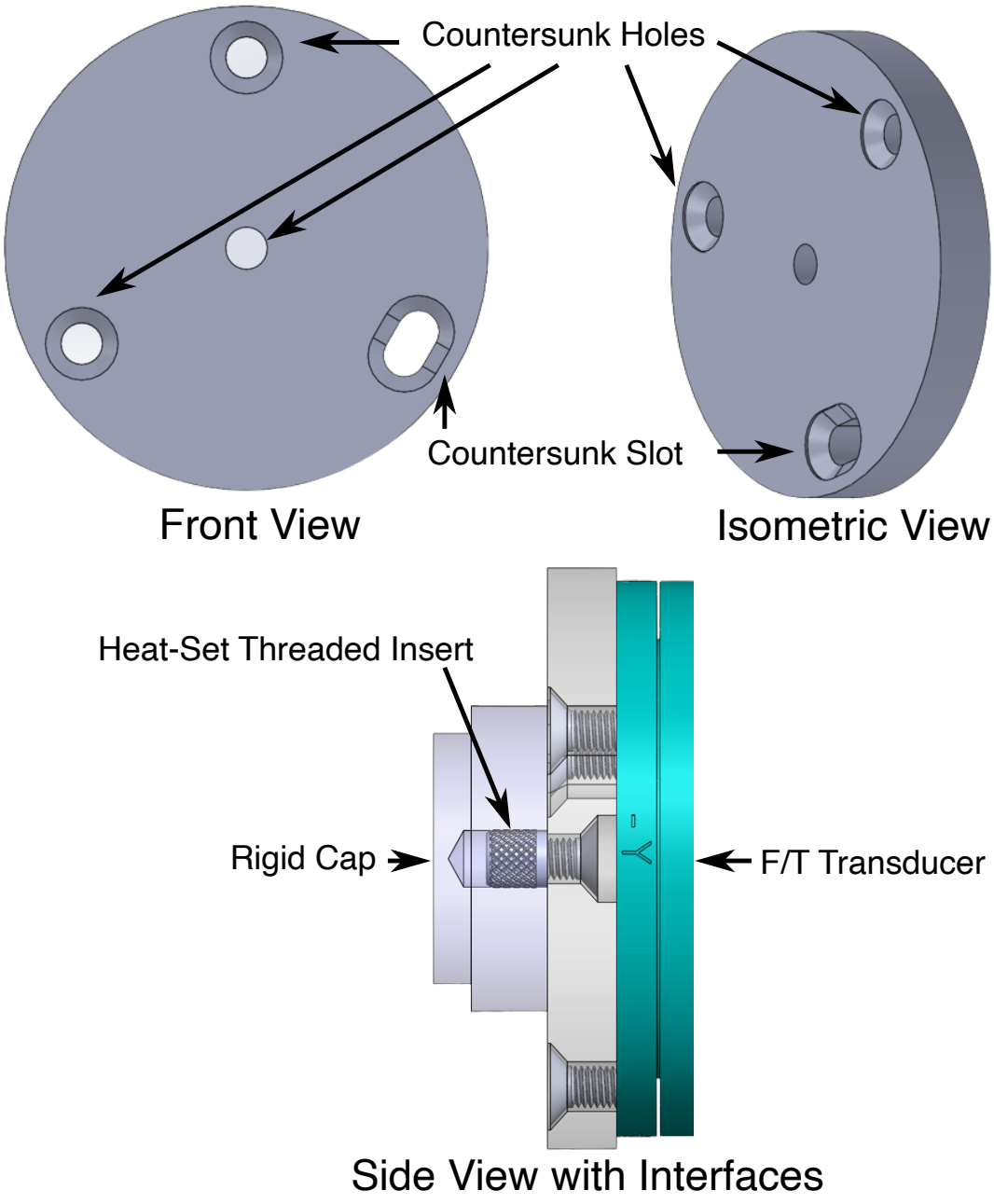

Figure 3.4. CAD model of the adapter plate which transfers actuator forces to the F/T transducer, shown in (a) front view, (b) isometric view. (c) presents the adapter plate and its interfacing strategy with the rigid cap and F/T transducer.

3.1.3 Additional Design Considerations

With the static test fixture design completed, preliminary static tests were conducted. Here it was identified that the nozzle to actuator interface through the flexible plug would slip at higher actuator elongations, when the static offset axial forces are large enough to overcome the contact friction. This would reduce the effective length of the bellows actuator and result in inaccurate readings. Therefore, C-clamp inspired attachments are designed to secure the air inlet end of the actuator to the horizontal support. The C-clamp attachment is in two C-pieces joined through two M3 screws and nuts at each end to form a clamp on the actuator assembly. The attachment is then secured to the horizontal support through flanges on the C-pieces using another pair of M3 screws and nuts. The CAD model and realized attachment are shown in Figure 3.5. This requires slight modification of the support where two M3-sized clearance through slots of slot length 8 mm are added for the screws. Additionally, the slots enable some assembly clearance for the screws in the vertical direction as the attachment is secured. The C-piece geometry adheres to the actuator assembly's outer diameter of 23.50 mm at their interface and then curves away at an inflection point to later form flat clamping surfaces. This results in a robust test fixture design which can be used to get reliable axial and shear blocked force measurements from the soft pneumatic actuator at different lengths and orientation angles. The complete test fixture assembly with the designed actuator is shown in Figure 3.6. Here, one might identify from Figure 3.6(c) that the threaded insert has a lip that is not flush with the rigid cap surface. Although this is not ideal and in future test setups a different threaded insert would be used, it does not affect force measurements since all the loads are transferred through the secured M3 screw.

3.2 Testing Procedure and Methods

With the soft actuator and static test fixture manufactured, we discuss the testing methods which enable us to acquire useful experimental data to verify the active (axial) and passive (shear) force models presented in Chapter 2. With the six axis F/T transducer, we will be able to measure the three orthogonal forces (F_x, F_y, and F_z) along with the mo-

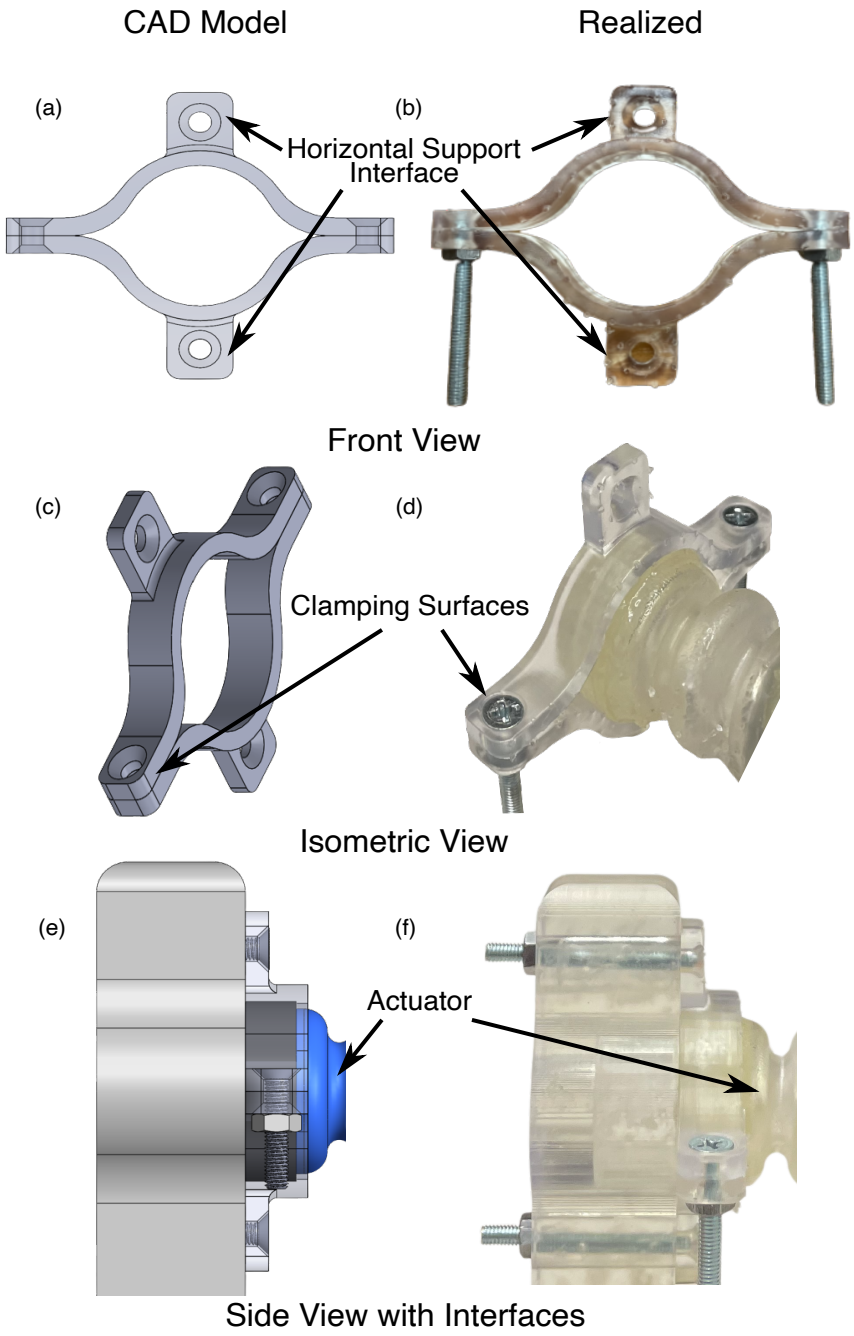

Figure 3.5. C-clamp attachment's CAD model manufactured component, and interfaces. The front views of the C-clamp are shown in (a) and (b), and isometric view in (c) and (d). In (e) and (f), the CAD modeled interfacing strategy and the realized interfaces between the C-clamp, actuator and horizontal support are shown.

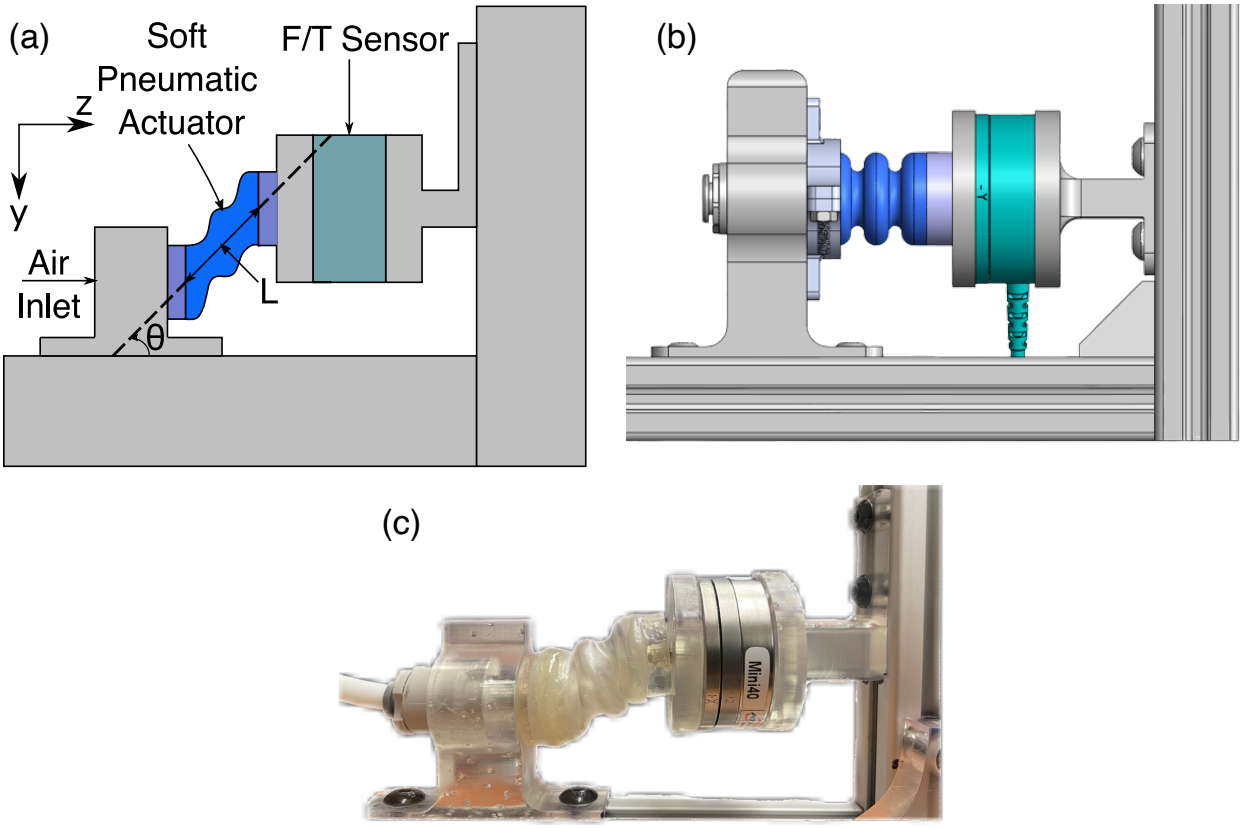

Figure 3.6. The complete test fixture with all components as designed. (a) A schematic of the test fixture where both structural supports are movable. The effective length of the actuator, L is calculated along the axis of the soft portion of actuator and the angle, θ is measured from the z-axis to the axis of the soft portion of actuator. (b) CAD model of the test fixture, and (c) realized test fixture setup for $L = 20.30$ mm ($\Delta L = 1.8$ mm) and $\theta = 50°$. Modified from [64] ©IEEE 2022.

ments (T_x, T_y, and T_z). Because of the static test setup, only y-z planar forces, and its corresponding out-of-plane moment, T_x are expected to be non-zero.

Two input parameters for the force characterization model and the test fixture are identified as the change in effective length, ΔL, and the orientation angle, θ, of the soft actuator. Hence, it is wise to prescribe tested deformation configurations in terms of the same parameters. We assume that the effect of orientation angles on the forces are symmetrical about the horizontal (z-) axis, as is shown in Equations 2.16 and 2.17. Since a possible application of this work is for haptic feedback, the test ranges are based on the ranges of previous haptic

devices designed to produce skin stretch or skin slip [65] where the maximum angular rotation is 60° and maximum skin-stretch displacement is about 10.5 mm. The testing ranges are also adjusted based on the limitations of the actuator assembly, since it was identified through testing that part failure might occur upon pressurization at $\theta > 50°$. Thus, tests are conducted at nominal orientation angles of $\theta = 0°$, 10°, 18°, 25° and 30° for each of nominal compressed ($\Delta L = -2$ mm, -1 mm), natural (0 mm) and elongated ($\Delta L = +1$ mm, $+2$ mm) lengths. Two additional tests at $\theta = 0°$ for nominal compressed $\Delta L = -3$ mm and elongated $\Delta L = +3$ mm lengths are performed to obtain a more robust axial forces dataset. Furthermore, to establish repeatability, each configuration is tested twice resulting in a total of 54 tests. For the adjustments of the actuator on the static test fixture to obtain the desired lengths and orientation angles, the known dimensions and geometry were used in Microsoft Excel's equation solver to obtain the supports' positions along their respective rails. These positions were set using a vernier caliper, for precise positioning, with the 90° corner of the fixture as datum. Since, the y- and z- positions of the test supports are manually set for the actuator's test configurations, there is a mean error of 0.04 mm and 0.18 degrees in the experimental ΔL and θ measurements with maximum errors of 0.13 mm and 0.65 degrees respectively. We call out where experimental measurements are used instead of nominal measurements throughout the analysis.

The other input parameter in the presented force models is the air inlet pressure, P. It is essential to regulate air inlet pressures in this experimental setup to obtain force outputs at varying pneumatic pressures. This is achieved by using a closed-loop pressure regulator (QB3TANKKZP10PSG, Proportion-Air) controlled by an input/output device (myRIO 1900, National Instruments). The pressure regulator used is analog DC voltage-controlled from 0 to 5 V with a linear output ability between 0 and 68.95 kPa (10 psi) of gauge air pressure, and pressure accuracy under ±0.5 % of full scale [74]. To verify proper functioning of the pressure regulator and obtain real-time pressure data, air inlet pressure is also measured using a board mount pressure sensor (HSCDANN015PGAA5, Honeywell). This sensor has a sensing range from 0 to 103.42 kPa (15 psi) of gauge pressure with an analog output which can be fed directly into a data acquisition system. Its accuracy is ±0.25 % of full scale from the best fit straight line, which enables reliable measurements for characteri-

zation [75]. Tests are conducted by increasing air inlet pressures from 0 to 41.4 kPa (6 psi) at 2.76 kPa (0.4 psi) intervals and then decreasing at 4.14 kPa (0.6 psi) intervals, to study hysteresis effects. Each pressure interval was maintained for three seconds in order to avoid the pressure regulator dynamics becoming dominant and to check for viscous effects from the soft actuator's material. In preliminary testing, each pressure interval was held for up to ten seconds to analyze the dynamic and viscous behavior of the system. We observed that the pressure regulator dynamics dominate over the soft actuator dynamics, and the settling time of the pressure is less than 0.4 seconds. Hence, the pressure interval hold was reduced to three seconds for efficient testing. As well, there were no significant viscous effects from the material, since the actuator deformation is performed before the test and held constant. More details and discussion on the experimental results from this analysis is presented in Section 3.3.

With the F/T transducer and pressure sensor setup as outputs of the static test setup, it is imperative to implement a data acquisition system with synchronous measurements. This can be most efficiently achieved using a voltage input module. We employ the C-Series 9205 with a cDAQ 9174 chassis, both by National Instruments to accomplish this. A LabVIEW environment which integrates and processes the six axis readings from the F/T tranducer, and the board mount pressure sensor is developed using the F/T transducer manufacturer's sample code and provided calibration files. To ensure that we obtain accurate static offset data, the F/T transducer is zero biased through LabVIEW at the experimental natural length, $\Delta L = 0$ mm, and orientation angle, θ, of 0 degrees every time the data acquisition system or the sensors are power cycled.

3.3 Experimental Results and Model Fitting

So far, we have designed the soft pneumatic bellows actuator in Chapter 2, the static testing fixture in Section 3.1, and outlined the testing procedure in Section 3.2. Now, we are prepared to start testing and obtain experimental results.

With the tests successfully completed, the raw experimental results for axial and shear forces are plotted as functions of inlet pressure as shown in Figures 3.7 to 3.14. Due to the

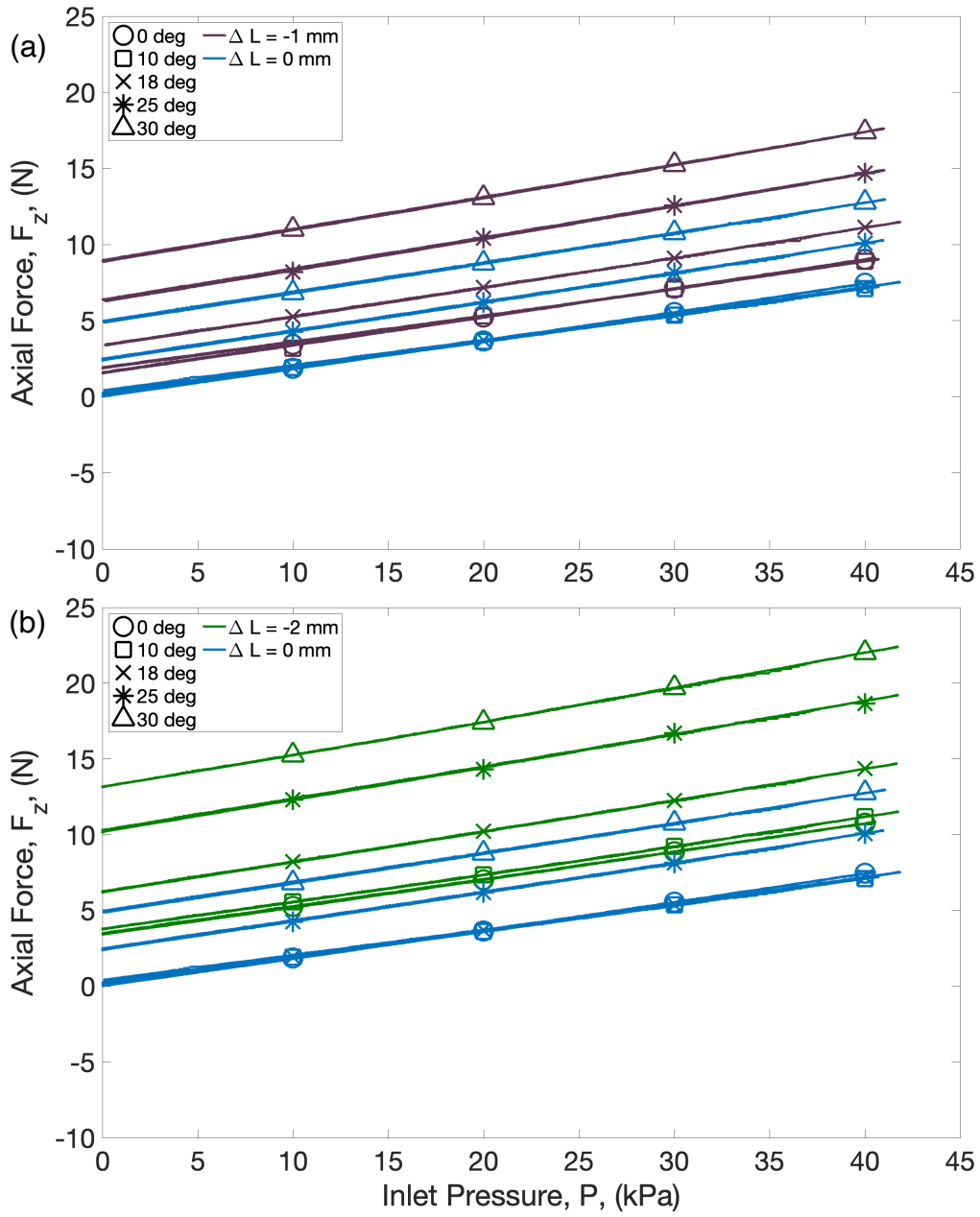

Figure 3.7. Axial forces vs air inlet pressure for compressed actuator lengths. (a) Axial forces for different orientation angles when nominal $\Delta L = -1$ mm, (b) Axial forces for different orientation angles when nominal $\Delta L = -2$ mm. The plots show the entire axial force versus pressure data obtained from the F/T transducer. The markers are only added for visibility and identification of the different actuator configurations. The legend markers signify the nominal ΔL and θ.

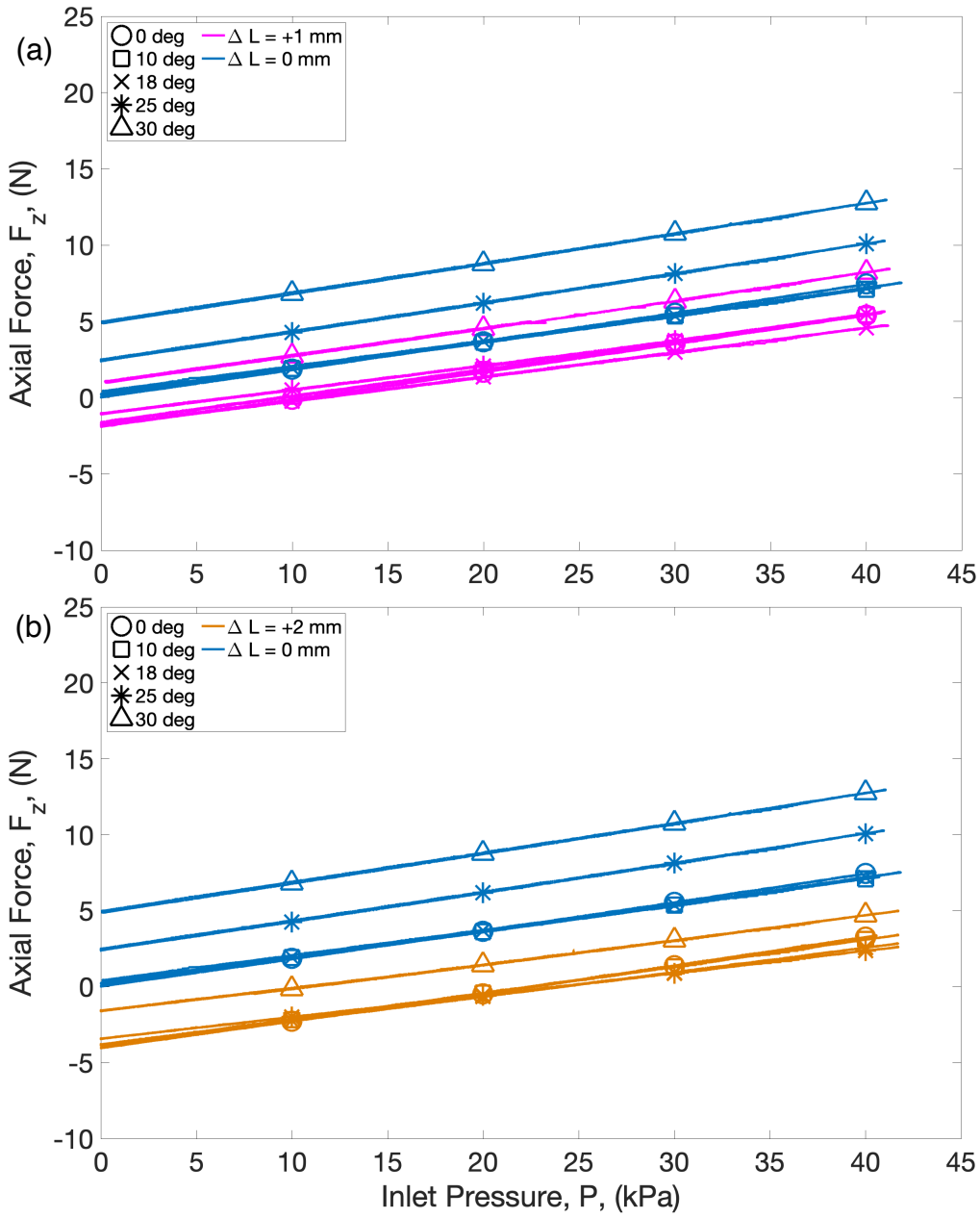

Figure 3.8. Axial forces vs air inlet pressure for elongated actuator lengths. (a) Axial forces for different orientation angles when nominal $\Delta L = 1$ mm, (b) Axial forces for different orientation angles when nominal $\Delta L = 2$ mm. The plots show the entire axial force versus pressure data obtained from the F/T transducer. The markers are only added for visibility and identification of the different actuator configurations. The legend markers signify the nominal ΔL and θ.

large amount of data and consequent overlap of force profiles between different configurations, the data has been distributed between the graphs. Figures 3.7 and 3.8 present the axial forces exerted by the soft actuator at different orientation angles with the actuator under compression ($\Delta L < 0$ mm) and under elongation ($\Delta L > 0$ mm) with the nominal natural length ($\Delta L = 0$ mm) configurations added to each for visual comparison. Figures 3.9 and 3.10 present the shear forces exerted by the soft actuator in a similar format. This helps in qualitative analysis to determine the influence of θ on the forces for a given actuator length, ΔL. Figures 3.11, 3.12, 3.13, and 3.14 present the axial and shear force readings from the same experiments but now segregated by orientation angles to better visualize the relationship between the forces and ΔL for a given orientation angle, θ. From the force outputs, it is evident that the both force components have strong linear behaviors to air inlet pressure, as expected from knowledge of internal pressures and from Equations 2.5 and 2.7 in Chapter 2.

From Figures 3.7 and 3.8, it can be inferred that the gradient of axial forces to air inlet pressure is independent of the actuator configurations of ΔL and θ, since the slope of every plotted force profile is visually the same. This is in agreement with the presented model in Equation 2.5. Additionally, we can identify that the static offset axial force, axial force at zero inlet pressure, increases as the orientation angle increases, and decreases as the actuator length increases. The axial static offset forces are analyzed in more detail in Figures 3.15 later in this section.

Unlike the axial forces, shear forces are clearly dependent on the actuator configuration. This is identifiable in Figures 3.9 and 3.10 where the gradient of the shear force is increasingly negative as the orientation angle increases, whereas there is no discernible effect of change in actuator length, ΔL, on the gradient. This is in conjunction with the derived Equation 2.7 where the shear pressure forces are linearly dependent on θ but independent of ΔL. Moreover, we can also identify that the shear static offset forces increase with increasing θ as well as increasing ΔL, and is analyzed in further detail in Figure 3.16.

Figures 3.11 and 3.12 give us a different perspective to the same data by making the effects of changing the actuator length on the axial forces more intuitive. Here, we can clearly see that changing the effective actuator length, ΔL, only decreases the axial component of

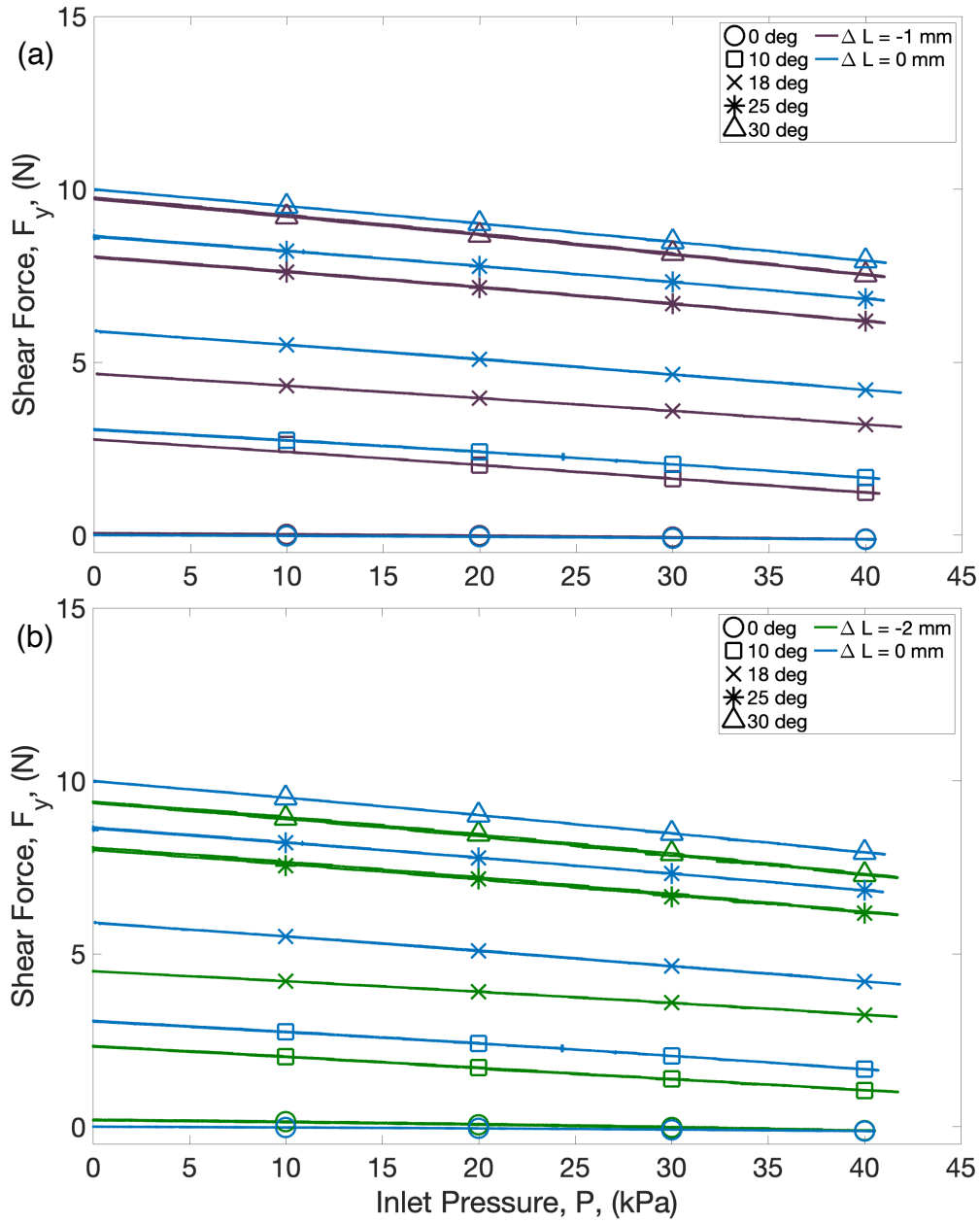

Figure 3.9. Shear forces vs air inlet pressure for compressed actuator lengths. (a) Shear forces for different orientation angles when nominal $\Delta L = -1$ mm, (b) Shear forces for different orientation angles when nominal $\Delta L = -2$ mm. The plots show the entire shear force versus pressure data obtained from the F/T transducer. The markers are only added for visibility and identification of the different actuator configurations. The legend markers signify the nominal ΔL and θ.

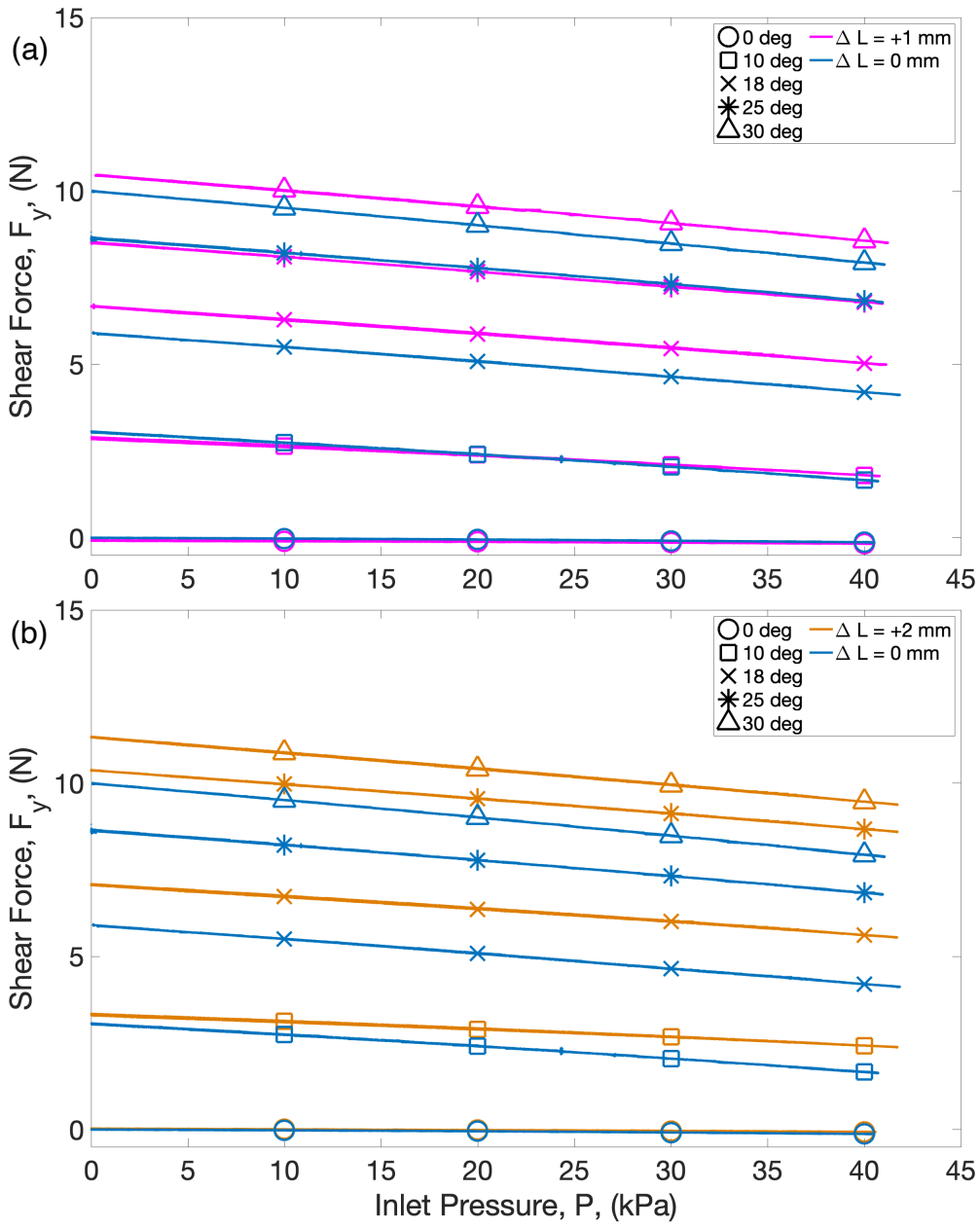

Figure 3.10. Shear forces vs air inlet pressure for elongated actuator lengths. (a) Shear forces for different orientation angles when nominal $\Delta L = 1$ mm, (b) Shear forces for different orientation angles when nominal $\Delta L = 2$ mm. The plots show the entire shear force versus pressure data obtained from the F/T transducer. The markers are only added for visibility and identification of the different actuator configurations. The legend markers signify the nominal ΔL and θ.

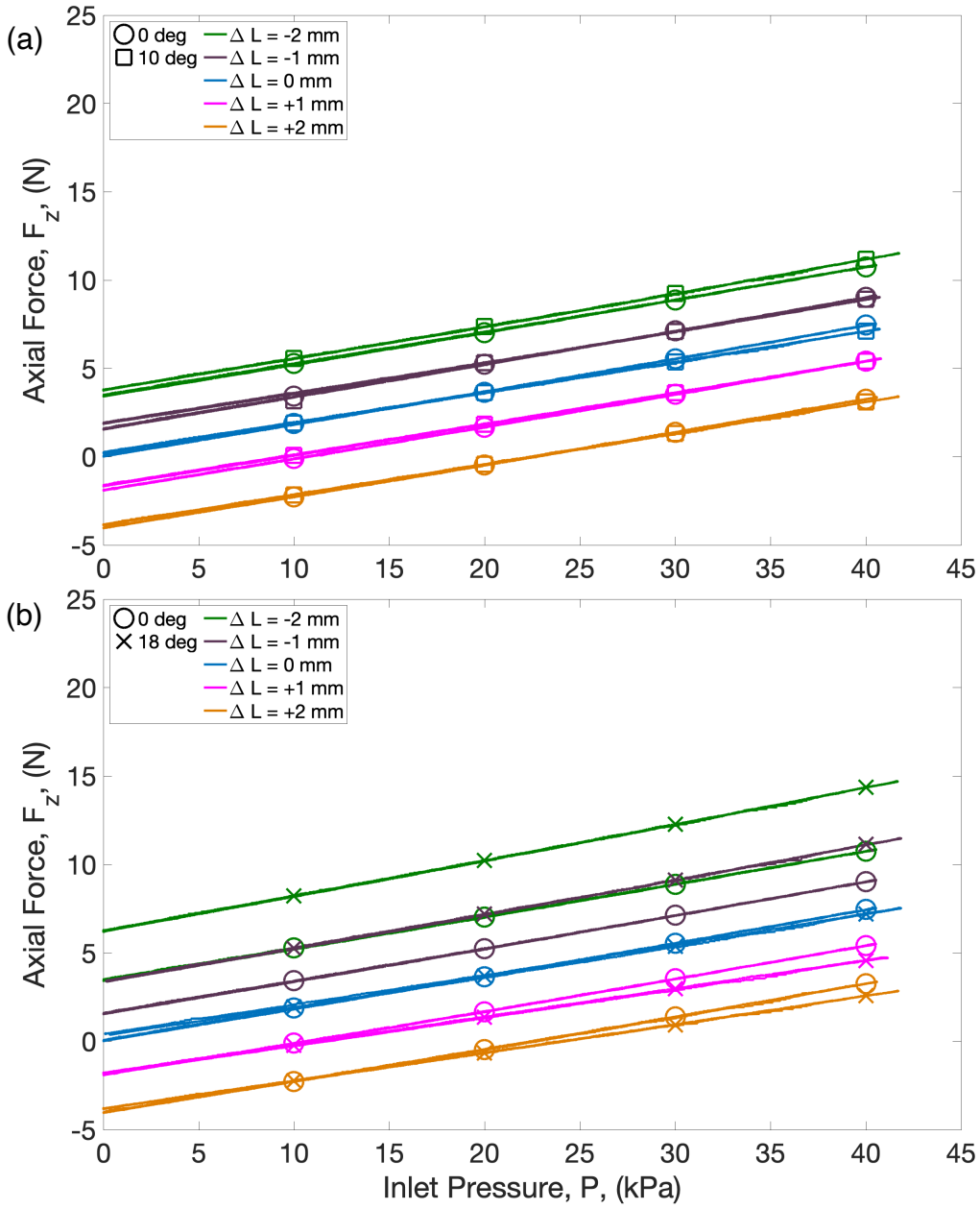

Figure 3.11. Axial forces vs air inlet pressure for all tested actuator lengths for a given orientation angle. (a) Axial forces for different actuator lengths when nominal $\theta = 10°$, (b) Axial forces for different actuator lengths when nominal $\theta = 18°$. The plots show the entire axial force versus pressure data obtained from the F/T transducer. The markers are only added for visibility and identification of the different actuator configurations. The legend markers signify the nominal ΔL and θ.

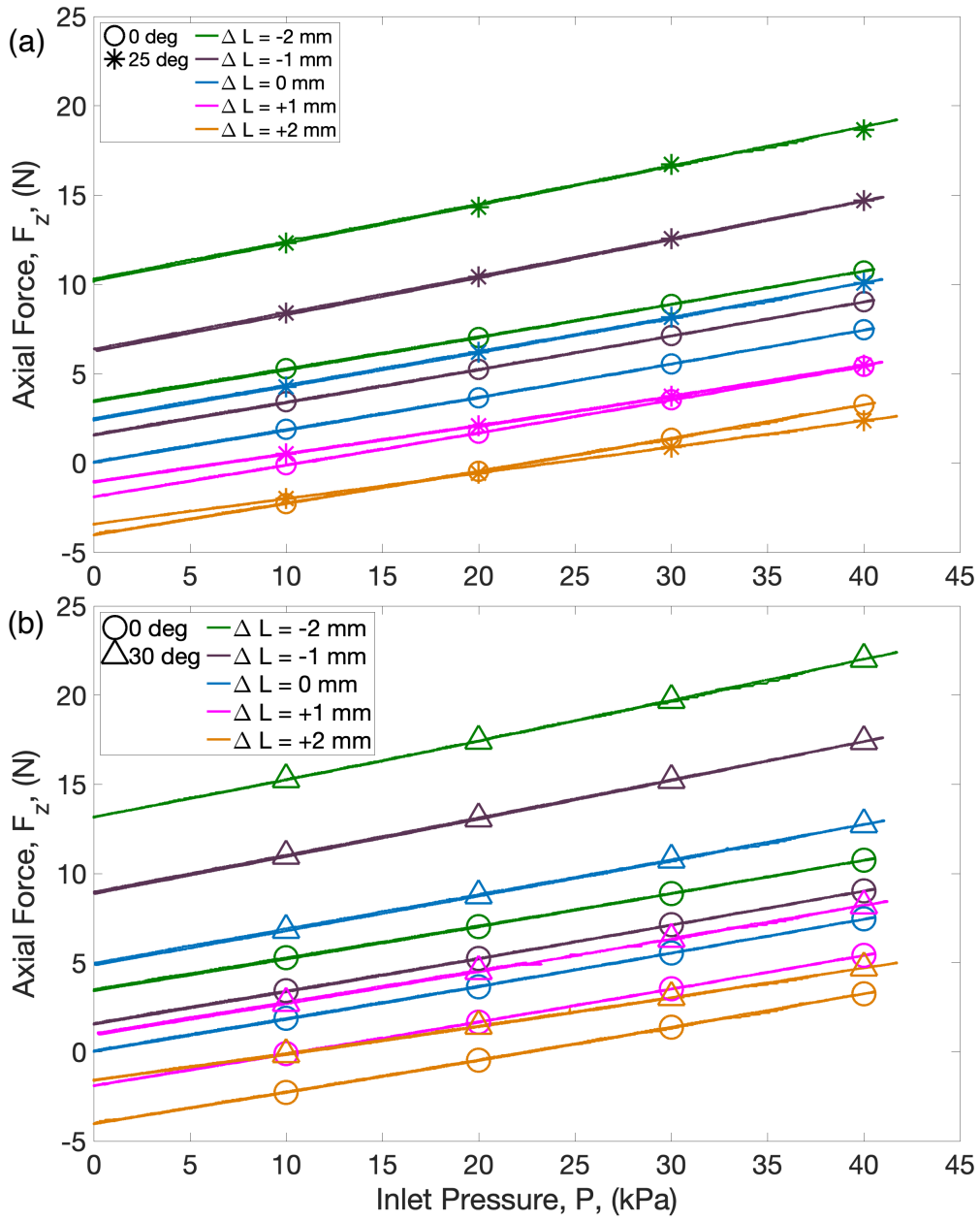

Figure 3.12. Axial forces vs air inlet pressure for all tested actuator lengths for a given orientation angle. (a) Axial forces for different actuator lengths when nominal $\theta = 25°$, (b) Axial forces for different actuator lengths when nominal $\theta = 30°$. The plots show the entire axial force versus pressure data obtained from the F/T transducer. The markers are only added for visibility and identification of the different actuator configurations. The legend markers signify the nominal ΔL and θ.

the static offset force whereas the slope of axial forces to inlet pressure remains constant. Comparing this behavior over both Figure 3.11 and 3.12 reveals that this slope is nearly constant even over all tested orientation angles. Moreover, upon comparing the axial static offset force magnitudes over the figures, we see that it increases with increasing θ. This is in agreement with our inferences from Figures 3.7 and 3.8, and with the axial force model in Equation 2.16.

In Figures 3.13 and 3.14, we can more clearly see the relationship between change in effective actuator length and the shear forces. Upon visual examination, we can clearly tell that the slope of the force profile is nearly constant irrespective of ΔL for a fixed non-zero orientation angle. Moreover, the shear static offset forces increase with increasing ΔL as well as θ, which can be identified by looking at the shear static offset force magnitudes over both figures. These inferences are in line with the predicted behavior in the model presented in Equation 2.17. Similar to Figures 3.9 and 3.10, the shear components of the actuator forces are zero irrespective of the actuator lengths when the orientation angle is zero. This is expected since the majority of the pressure forces cancel out in the shear direction due to the rotational symmetry of the bellows. This means that the shear effective area, $A_{y,\text{eff}}$, and consequently shear pressure forces will be zero under pure axial deformation (nominal $\theta = 0°$). This corresponds to the shear component of the linear spring force in Equation 2.15.

After preliminary visual analysis, we estimate the model constants. For the static offset forces, this is done by taking the mean of the force readings in their respective directions at each configuration when the inlet pressure is zero. This is shown in Figures 3.15 and 3.16 where the extracted static offset forces are independently plotted as functions of both nominal ΔL and nominal θ. The experimental results are analogous to the model, where the axial static offset forces, $F_{z,0}$, has a negative and roughly linear relationship to ΔL, but a non-linear relationship to θ, and shear static offset forces, $F_{y,0}$, have a linear relationship to both ΔL and θ. These observations validate Equations 2.14 and 2.15.

Thereafter, we can subtract the extracted static offset forces from the raw force data to obtain the pressure forces. In Figure 3.17, these are plotted against the nominal orientation angle, θ, as a mode of comparison since we expect shear effective area, $A_{\text{y,eff}}$, to only have a relationship to θ whereas the axial effective area, $A_{\text{z,eff}}$ is expected to be independent to

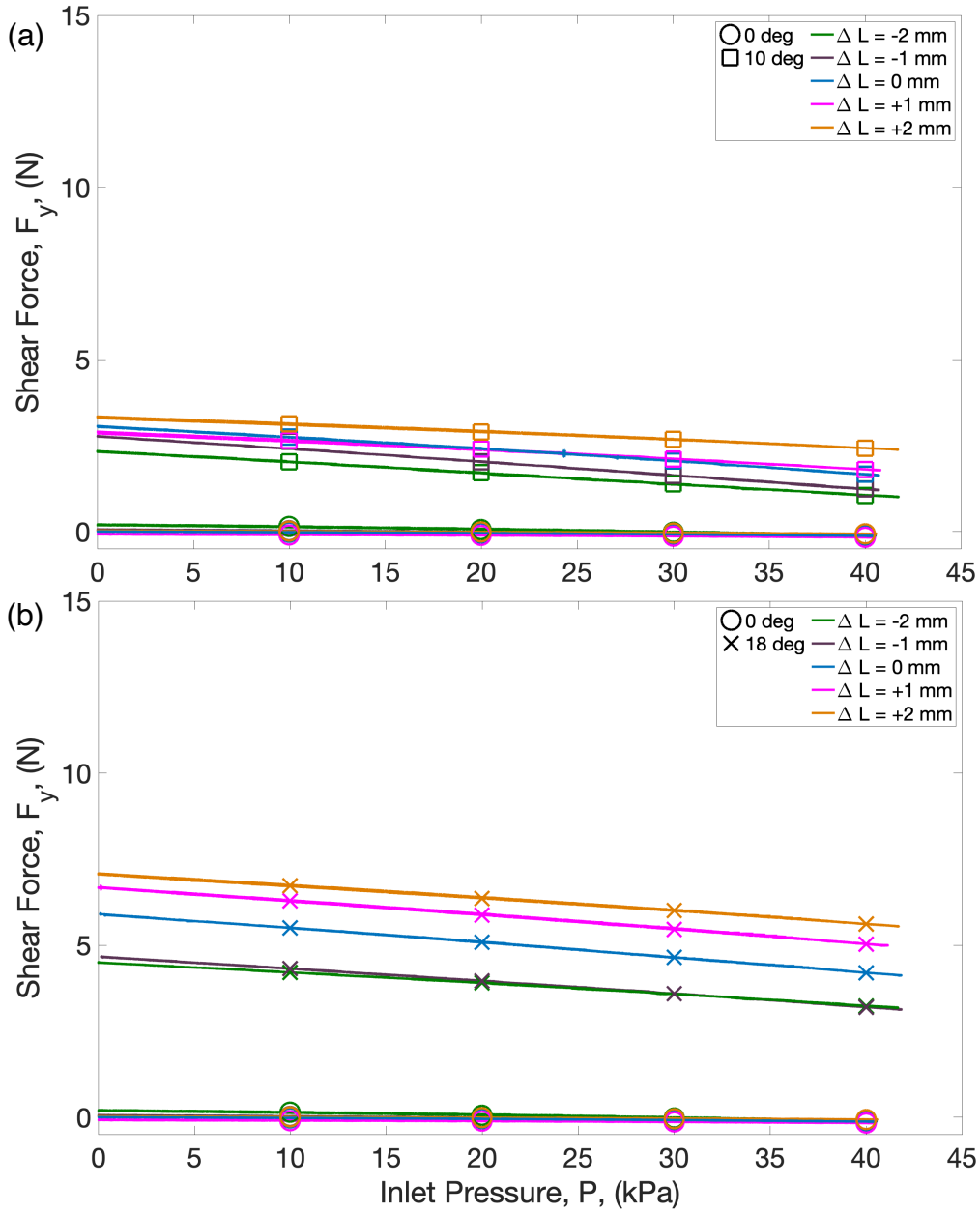

Figure 3.13. Shear forces vs air inlet pressure for all tested actuator lengths for a given orientation angle. (a) Shear forces for different actuator lengths when nominal $\theta = 10°$, (b) Shear forces for different actuator lengths when nominal $\theta = 18°$. The plots show the entire shear force versus pressure data obtained from the F/T transducer. The markers are only added for visibility and identification of the different actuator configurations. The legend markers signify the nominal ΔL and θ.

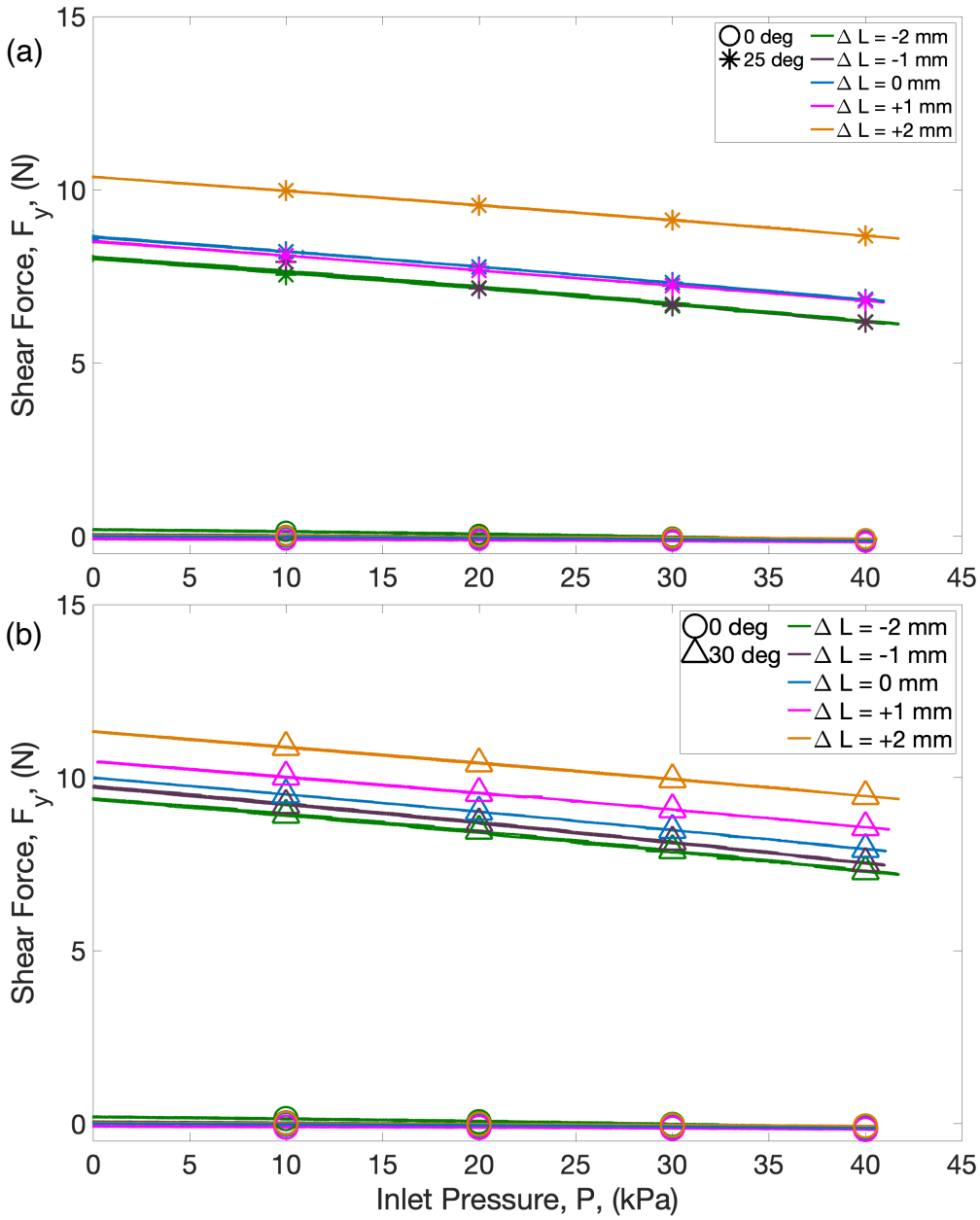

Figure 3.14. Shear forces vs air inlet pressure for all tested actuator lengths for a given orientation angle. (a) Shear forces for different actuator lengths when nominal $\theta = 25°$, (b) Shear forces for different actuator lengths when nominal $\theta = 30°$. The plots show the entire shear force versus pressure data obtained from the F/T transducer. The markers are only added for visibility and identification of the different actuator configurations. The legend markers signify the nominal ΔL and θ.

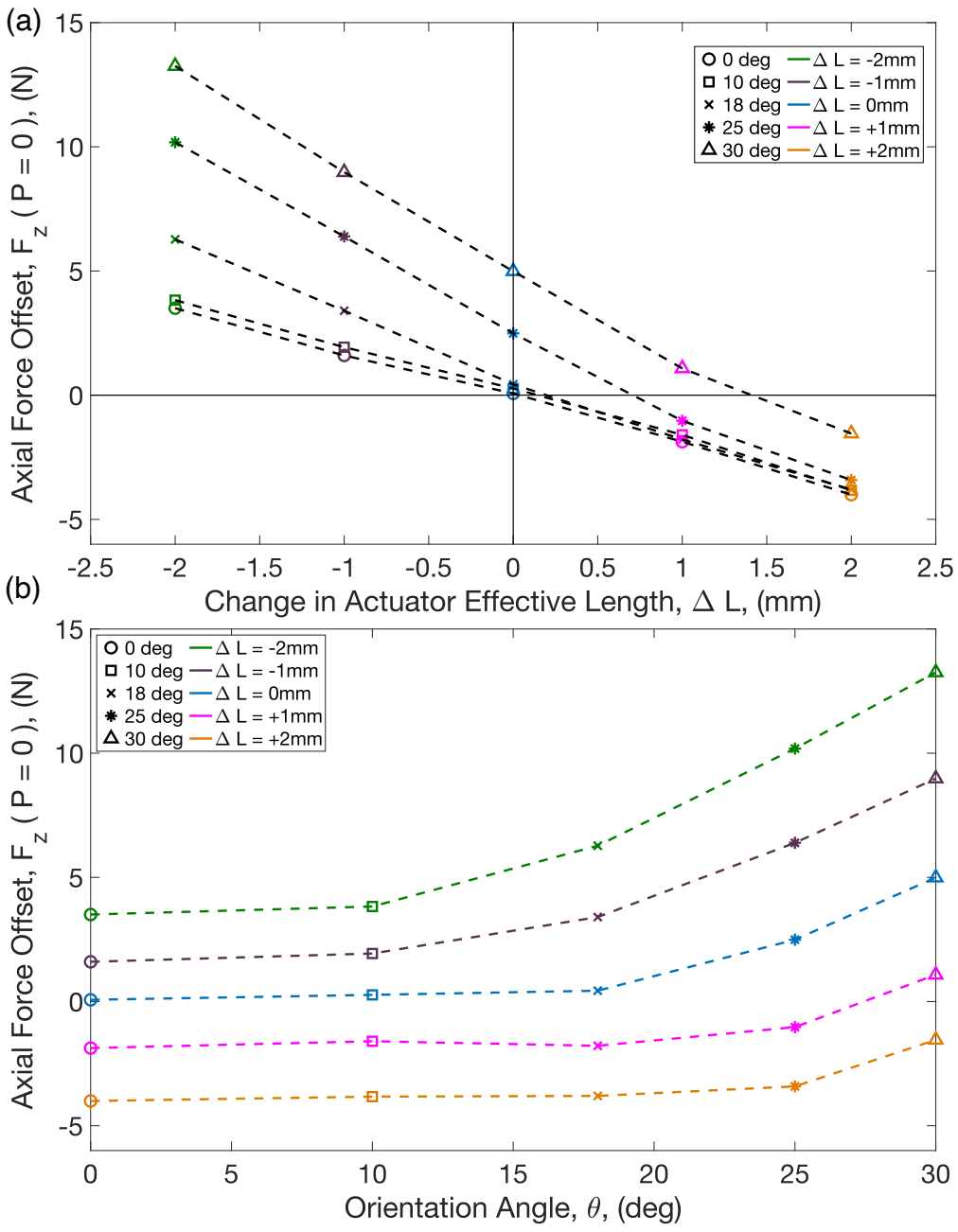

Figure 3.15. Axial static offset forces as separate functions of the actuator configuration variables, change in effective length and orientation angle. The data points in this plot are averages of extracted axial static offset forces for each configuration. (a) Axial static offset force plotted against nominal ΔL, (b) Axial static offset force plotted against nominal θ.

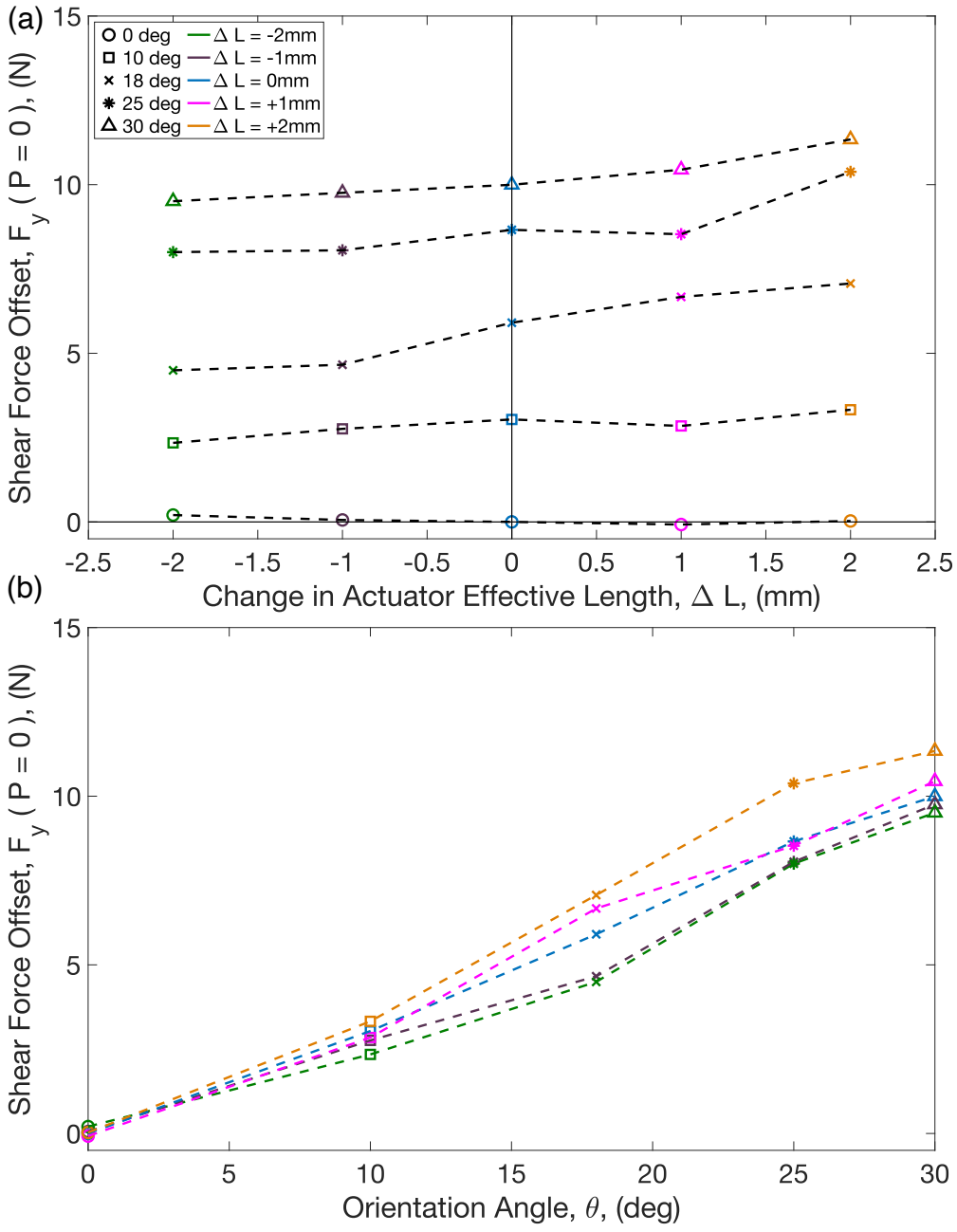

Figure 3.16. Shear static offset forces as separate functions of the actuator configuration variables, change in effective length and orientation angle. The data points in this plot are averages of extracted shear static offset forces for each configuration. (a) Shear static offset force plotted against nominal ΔL, (b) Shear static offset force plotted against nominal θ.

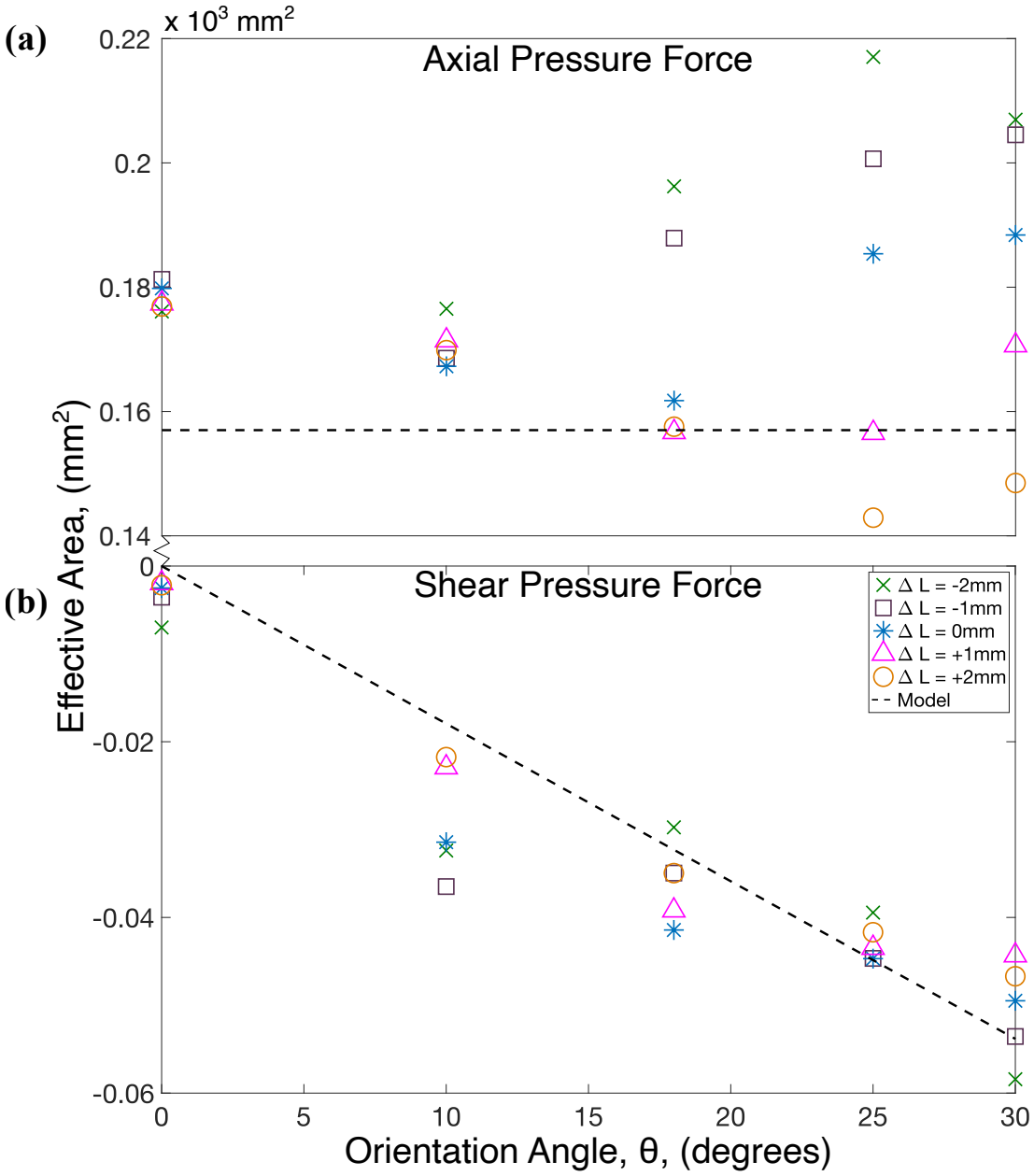

Figure 3.17. Effective cross-sectional areas for the axial and shear pressure forces, as a function of the nominal θ, and the corresponding model fits. The markers and the legend present the nominal actuator configurations. The data points in this plot are the averages of the effective areas for each configuration in axial and shear directions. (a) Relationship between the orientation angle and the axial effective area ($A_{z,\text{eff}}$). There is no distinct correlation and the dashed line represents the fit for $A_{z,\text{eff}} = 157$ mm^2. (b) Relationship between orientation angle and the shear effective area ($A_{y,\text{eff}}$). There is a clear linear relationship and the dashed line represents the fit for $W_{y,\text{eff}} = 102.8\text{mm}^2/\text{rad}$. From [64] ©IEEE 2022.

both. From Figure 3.17(b), we can confirm a strong linear relationship to θ and no noticeable dependency to ΔL. However, we do see higher order behaviors in the axial effective area, $A_{\text{z,eff}}$, in Figure 3.17(a) which differ between compression and extension of the soft bellows actuator. To characterize these would require further analyses which is out of scope for this thesis, hence we continue the characterization efforts assuming a constant $A_{\text{z,eff}}$ which is a good approximation given its range of magnitudes, 142.9 mm^2 to 217 mm^2.

With the static offset and pressure forces qualitatively analyzed, we can begin the quantitative characterization by fitting the experimental data to obtain the model constants, $A_{\text{z,eff}}$, $W_{\text{y,eff}}$, k_{s}, and k_θ. This is done on MATLAB using the "fmincon" solver which minimizes a constrained non-linear multi-variable function, and our derived model fits this criterion. To obtain robust results, this analysis is conducted by combining the raw force and pressure datasets from the sensors for all configurations into a single matrix with nearly 24 million rows. We start with inputting axial and shear force models as functions of the needed constants, and defining intermediate error functions between measured values and the model. Finally, the minimization function is defined as the root mean squared error of the shear forces error and the axial forces error. The algorithm for this is presented in Algorithm 1.

Algorithm 1 Minimization function for model constants

Require: Experimental data for inlet pressure (P), axial(F_z) and shear(F_y) forces, change in effective length (experimental ΔL), orientation angle (experimental θ)
Initialize: Model Constants $(A_{\text{z,eff}}, W_{\text{y,eff}}, k_s, k_\theta) \leftarrow$[1 1 1 1]

$F_{z,model} \leftarrow P A_{\text{z,eff}} - k_s \Delta L + k_t \theta^2$
$F_{y,model} \leftarrow -P W_{\text{y,eff}} \theta + k_s \Delta L \theta + k_t \theta$

$F_{z,error} \leftarrow F_z - F_{z,model}$
$F_{y,error} \leftarrow F_y - F_{y,model}$

$\text{fun}_{\text{min}} \leftarrow (F_{z,error})^2 + (F_{y,error})^2$

Model Constants $(A_{\text{z,eff}}, W_{\text{y,eff}}, k_s, k_\theta) \leftarrow$fmincon($\text{fun}_{\text{min}}$, [1 1 1 1])
▷ [1 1 1 1] are the initialized model constants

The resultant best-fit model constant of $A_{z,\text{eff}}$ is 157 mm^2 which when compared to the segregated axial pressure forces has a correlation coefficient of $R^2 > 0.93$, validating the

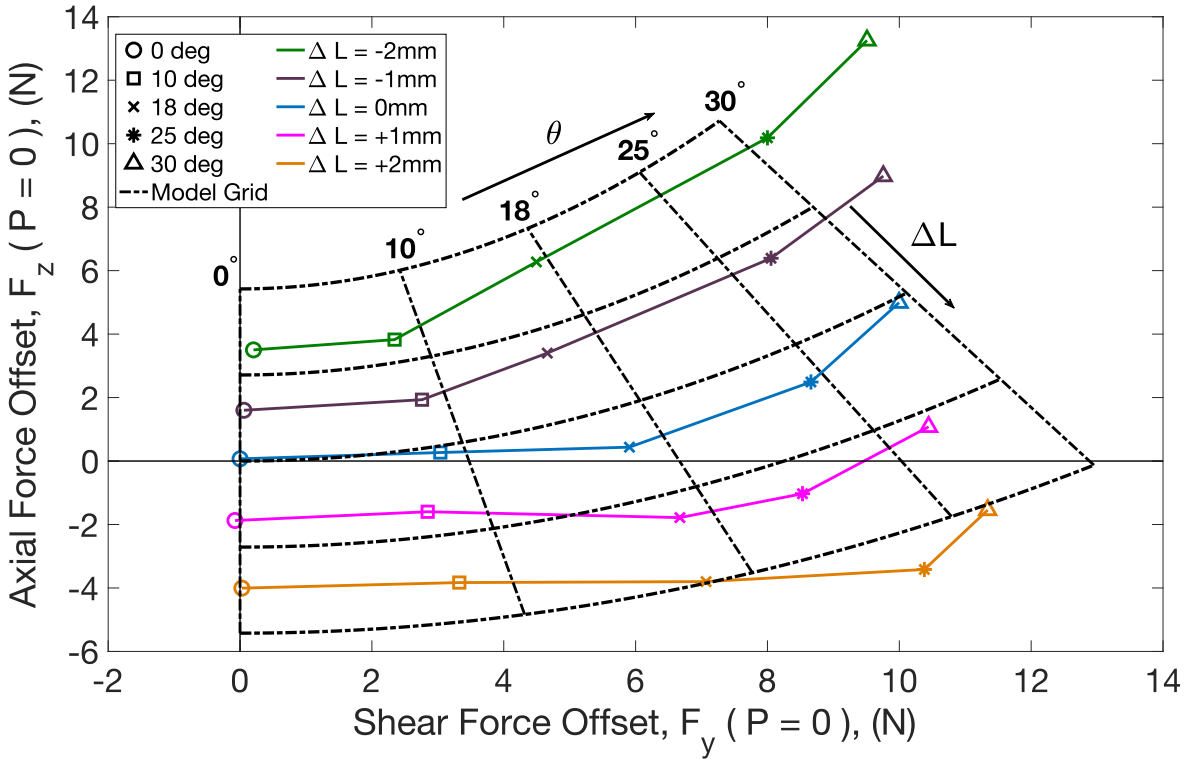

Figure 3.18. Experimental data and model for static shear and axial force offsets. The data shows a positive relationship to increasing θ for both axial and shear force offsets, an increasing relationship to ΔL for shear force offsets and a decreasing relationship to ΔL for axial force offsets. The modeled static force offsets are also presented in a "map grid" format to better visualize prediction performance in terms of magnitude and direction of static offset forces. The markers and the legend present the nominal actuator configurations. The data points in this plot are averages of extracted static offset forces for each configuration and direction. Modified from [64] ©IEEE 2022.

previous approximation of a constant axial effective area. Moreover, this is slightly smaller than the rigid cap's cross-sectional area of 254 mm^2. For $W_{y,\text{eff}}$, the constant coefficient to θ, the best-fit value is 105.2 mm^2/rad with a segregated correlation coefficient of $R^2 > 0.92$. The model-fitted constants for the axial and shear pressure forces are presented with dashed lines in Figure 3.17. The linear spring stiffness, k_s, comes out to be 2.71 N/mm and the torsional factor, k_θ, is best-fitted to 19.31 N/rad giving static offset R^2 values above 0.91 in the axial direction and above 0.94 in the shear direction.

In Figure 3.18, the experimental axial and shear static forces are plotted on the y- and x- graphical axes respectively with the model predictions represented as a grid. Visually, the static offsets force model fits well with the measured data trends. Larger errors occur primarily at the extreme values of θ and ΔL which may indicate a need to use the full model, not the small angle approximation, for nominal angles above 25°, and to implement a variable torsional moment arm, L_m, for the torsional spring component which changes with extension and compression of the actuator.

Combining the pressure and static offset forces models, the overall axial and shear forces are predicted with R^2 above 0.93 and 0.94 respectively. The RMSE error for the axial forces is 1.51 N with full scale range of 33.07 N resulting in 4.57% error in axial force prediction, whereas the shear forces have RMSE error of 0.82 N and full scale range of 11.52 N, resulting in a 7.12% shear force prediction error. Therefore, the model well predicts the axial and shear forces. To weigh the need for added complexity by removing the simplifying assumptions, the model fitting was performed again for two possible improvements: (a) without the small angle approximation, and (b) without the constant torsional moment arm assumption. Without the small angle approximation, using Equations 3.1 and 3.2,

$$F_{z,0} = -k_s \Delta L \cos(\theta) + (k_\theta)\theta \sin(\theta) \tag{3.1}$$

$$F_{y,0} = k_s \Delta L \sin(\theta) + (k_\theta)\theta \cos(\theta) \tag{3.2}$$

the best-fit model yielded R^2 values of around 0.91 and 0.93, and RMSE errors of 1.69 N (5.11% of FSR) and 0.94 N (8.16% of FSR), in the axial and shear directions respectively. Although the performance is slightly weaker, this difference is not significant given the relatively small set of tested actuator configurations, and the already strong correlation of the simplified model.

For (b), instead of a constant torsional moment arm (L_{m}), a moment arm variable using a multiplicative model uncertainty is attempted such that the torsional factor, K_θ, is represented by

$$k_\theta = \frac{k_t}{L_{m,0}(1 + (\frac{\Delta L}{L_0}))} \tag{3.3}$$

where $L_{\mathrm{m},0}$ is the torsional moment arm when nominal $\Delta L = 0$ mm. This results in R^2 values of around 0.95 and 0.98, and RMSE errors of 1.30 N (3.93% of FSR) and 0.54 N (4.71% of FSR) in the axial and shear directions respectively. Although there is a slight improvement, a model like this significantly increases the complexity of an already well-fit model. Therefore, we continue to use the model with the small angle approximation and constant torsional moment arm assumptions to maintain simplicity without significant losses in accuracy.

From the analysis presented in this chapter, we can conclude that the 1-DOF actuator's force characterization using a pressurized parallel linear and torsional spring is a strong model for prediction. In the next chapter, we will extend this force prediction model with the obtained constants to more complex parallel network systems to evaluate its effectiveness.

4. MULTI-ACTUATOR SYSTEM DESIGN, MANUFACTURING AND RESULTS

In order to prove the effectiveness of the presented models in Equations 2.16 and 2.17 and the fit parameters from Chapter 3, we attempt to extend the force models to multi-actuator networks. The systems analyzed in this work are the delta mechanism using three parallel actuators, and the floating actuator mechanism using five actuators- one of which is "floating" between the feedback heads. In their respective sections, we will discuss the mechanism's design in more detail, derive the position prediction model of the feedback head(s) given the air inlet pressures for each actuator, and finally compare prediction to experimental results. The realized mechanisms are shown in Figure 4.1. Portions of this chapter have been presented in [64] ©IEEE 2022.

4.1 Delta Mechanism

In this section, we will discuss the design and manufacturing of the delta mechanism, the modeling approach for its feedback head's position prediction, and compare it to experimental results.

4.1.1 Design and Manufacturing

The first step to the design process is to identify the actuators used. The three pneumatic bellows actuators used in this mechanism are identical in design to the one analyzed in Chapters 2 and 3 such that the same experimentally obtained constants can be used for each actuator's forces. To enable symmetry, the actuators are oriented at 120° from each other. This allows the workspace of the delta mechanism to be symmetric. Due to this, we can perform experimental tests in only one of the symmetric quadrants to characterize the entire workspace without any informational losses [26].

With the actuator already designed and oriented, we need to design the outer ring of the delta mechanism and the feedback head, noting hermetic joints are functional requirements for both mating parts. The parts are 3D printed using the Formlabs Form 3 SLA printer

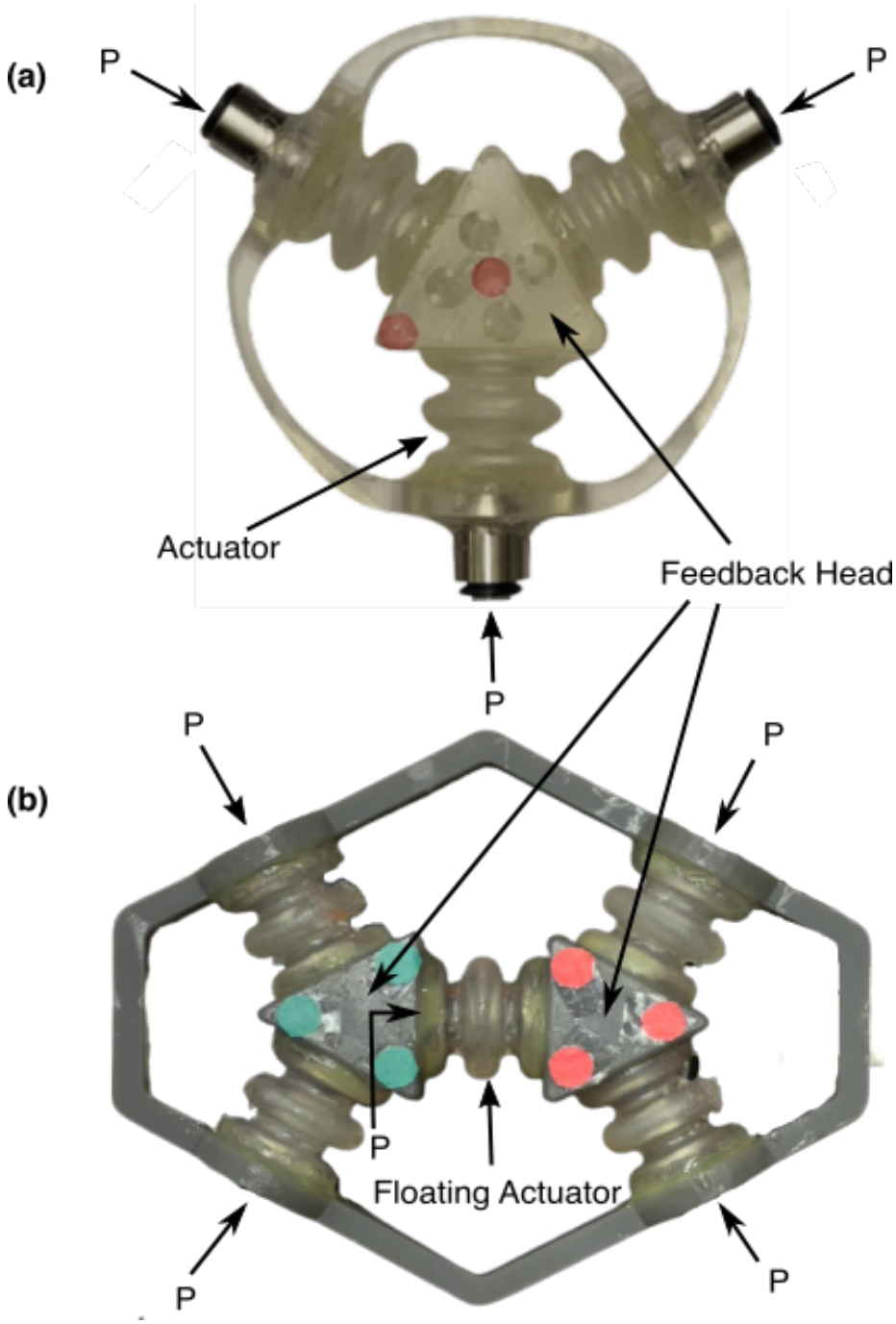

Figure 4.1. Realized multi-actuator systems with feedback heads labeled and air inlets specified as"P", (a) Delta mechanism with three independent air inlets and one feedback head, (b) Floating actuator mechanism with floating actuator labeled and five independent air inlets.

with the clear resin such that the feedback head and the outer ring are significantly more rigid than the actuators. For the feedback head, an equilateral triangular cross-section is chosen due to its simple geometry while still creating three equivalent straight lines, as its edges. These edges when extruded out-of-plane would create equivalent mating surfaces for the three actuators. To meet the dimensional constraints of the actuator outer diameter of 22 mm, the edge length of the equilateral triangular cross-section is 40 mm, and the height of the feedback head is 26 mm. Additionally, the edges of the resultant triangular prism are rounded with a radius of 3 mm.

With the preliminary geometry designed, we proceed with the mating surface design. The first option, inspired from the static test setup, would be to use a similar rigid cap design with a screw interface to the feedback head to create a hermetic assembly. However, this makes the feedback head's design and assembly more complex. Hence, we attempt to infuse the rigid cap design into the feedback head such that no additional parts are needed, and there is only one mating interface per actuator. This is done by creating a revolved cut on each of the feedback head's mating surfaces to which the actuators' flanges would mate to. The centers for both the revolved cut and the mating surface are coincidental in order to align the actuator's central axis appropriately. The revolved cut is of outer diameter 22.50 mm and inner diameter 18 mm such that a tight fit is formed with a total assembly tolerance of 0.50 mm between the outer diameters of the actuator and the cut. This tolerance is important since it allows room for extension of the actuator's diameter due to its compliance and reduces stresses at the joints, hence increasing their longevity. The depth of the revolved cut is 2 mm such that the actuator flanges of 3 mm length are sufficiently embodied in the cut to form a reliable joint. To complete the joints, the same flexible epoxy (DP110, 3M) is used here to bond the actuator flange to the feedback head through the revolved cut. The flat surfaces presented by the actuator flange and the cut enable desired mating configurations for the epoxy and hence, result in a strong hermetic joint. Figure 4.2 displays the CAD model of the feedback head.

The final step to the delta mechanism design is the outer ring which acts as the common base holding the actuators at their natural lengths when not pressurized, and provides the air inlet interfaces for the actuators. The first step to the design is to create three flat

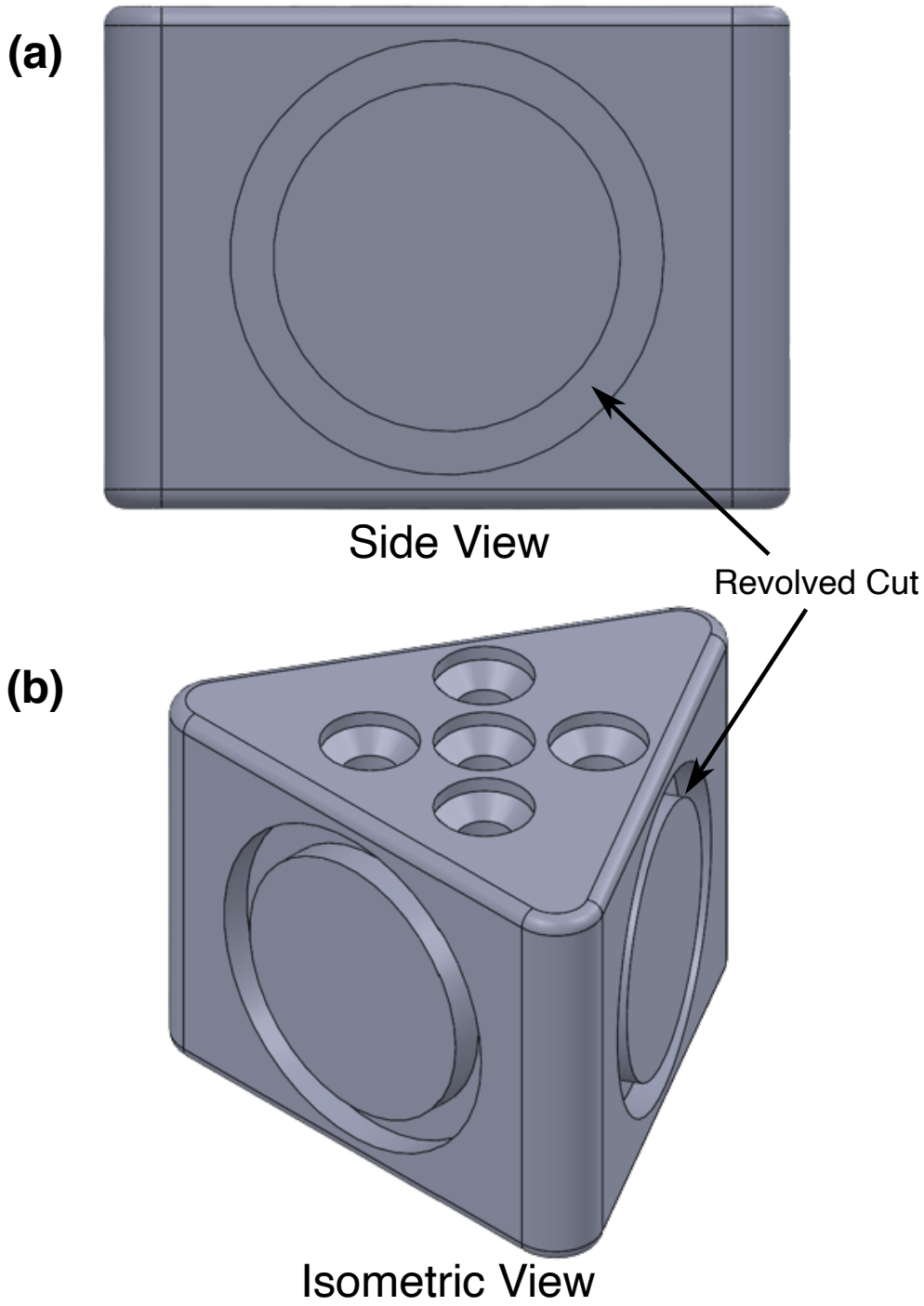

Figure 4.2. CAD model of the feedback head used in the delta mechanism. (a) Side view of the feedback head, and (b) Isometric view of the feedback head, both showing the revolved cut used to embody the actuator flanges.

surfaces where the actuator would mate with the outer ring. These surfaces have a circular cross-section of diameter 25 mm such that an actuator-wall distance of 1.5 mm is maintained when the actuator of outer diameter 22 mm is mounted. The mating technique is similar to that on the feedback head end using the revolved cut to sufficiently embody the 3 mm long actuator flanges. The thickness of 5 mm for these surfaces is determined by the depth of 2 mm needed for the revolved cut while still maintaining a wall thickness of 3 mm for the air inlet design. Finally, we incorporate the air inlet into these surfaces. The nozzle used in Chapter 3 worked well but is too long for practical use in the delta mechanism, hence we use a straight push-to-connect adapter with a #10-32 thread (5779K246, McMaster Carr) which with a total length of 19.56 mm is significantly shorter than the nozzle of total length 42.16 mm. To interface with the push-to-connect adapter, a housing is designed. First, a tightly toleranced through hole of 5 mm is added to the outer ring's surface geometry such that the threaded end of the adapter can be inserted in the hole. Next, a counterbore hole of 12.7 mm is created with a depth of 4 mm to house the 11.68 mm diameter adapter with nearly 1 mm of total assembly clearance. The interface can then be sealed using hot glue to ensure hermetic assembly throughout. With all the three surfaces designed, the final design step is to connect them to a common ring. This is done by creating concentric rings of 76 mm and 82 mm diameters, and creating extended flat surfaces to connect the mating geometries. This results in the outer ring being 3 mm wide with sections of 5 mm width where the mating surfaces are present. For a better visualization, Figure 4.3(a) shows the 2D sketch of the outer ring's underlying geometry. The ring is made 10 mm thick (out-of-plane direction) and fillets of radius 10 mm are added for geometric continuity between the ring and the mating surfaces. This helps with reduction of stress concentrations at these transitions. The actuators are assembled to the outer ring in a similar way to the feedback head, where the flexible epoxy is used to create the hermetic joint. The CAD model of the outer ring is shown in Figure 4.3(b) and (c). The delta mechanism is tested for leaks by random pressurization of each actuator, and no noticeable air leaks are identified within operating pressure ranges. Hence, hermetic design is achieved and reliable testing can be performed using this realized delta mechanism. The complete CAD model of the delta mechanism is shown in Figure 4.4.

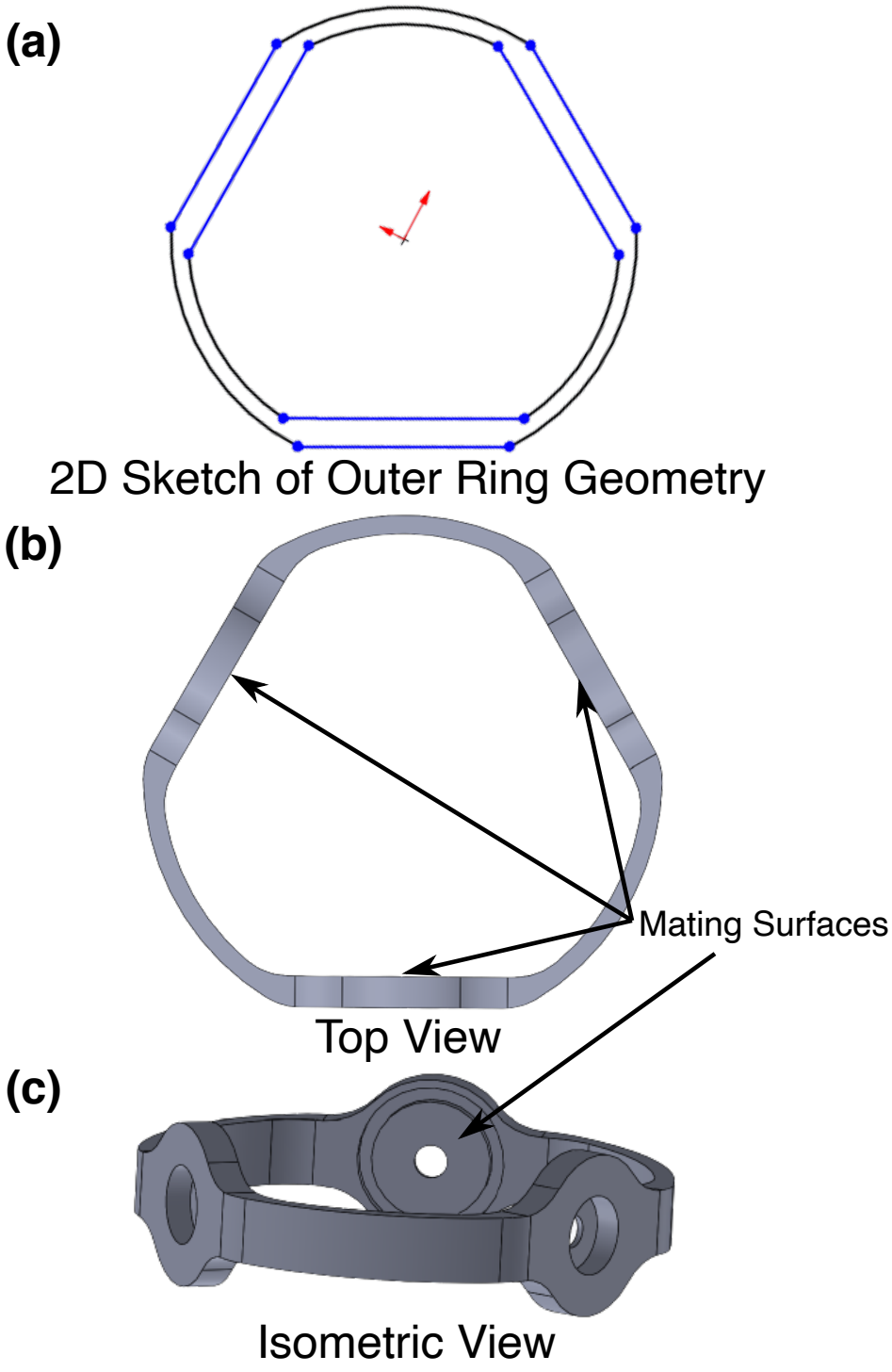

Figure 4.3. CAD model of outer ring for the delta mechanism. (a) 2D sketch of the outer ring geometry showing the underlying geometry, (b) Top view of the outer ring, and (c) Isometric view of the outer ring.

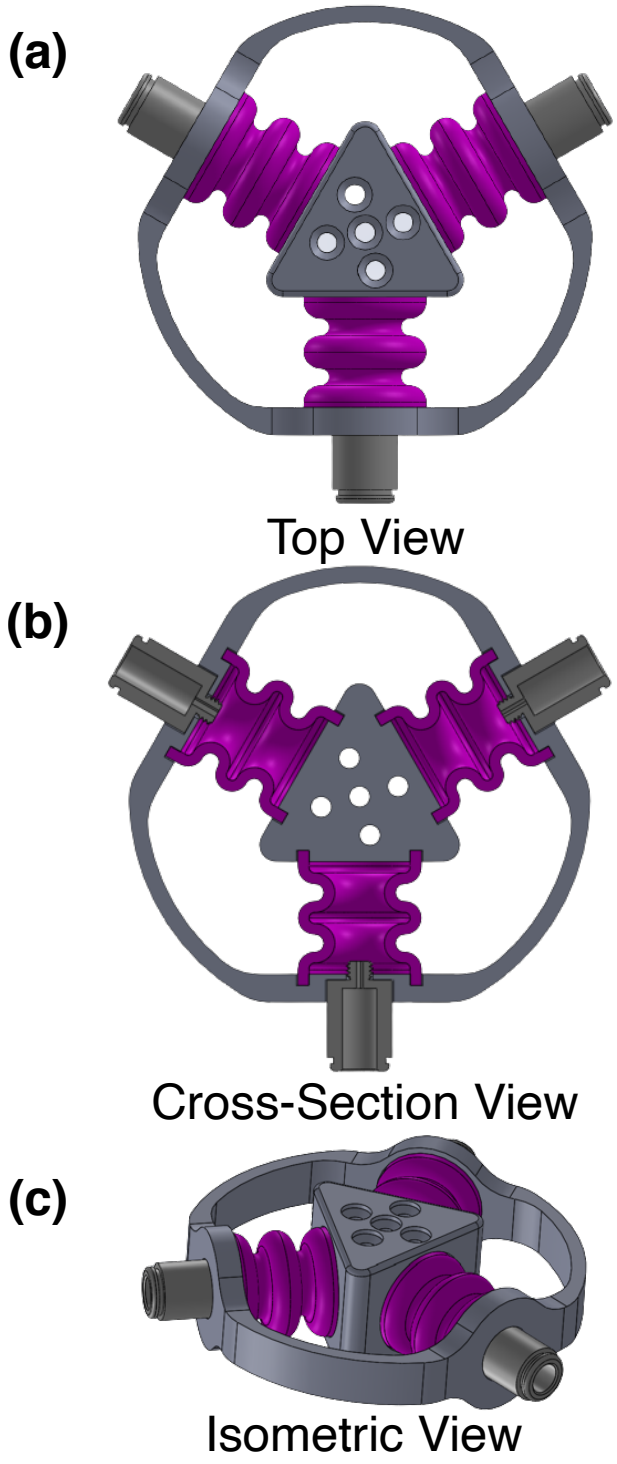

Figure 4.4. CAD model of the assembled delta mechanism. (a) Top view of the mechanism, (b) Cross-section view of the mechanism showing the different mating strategies adopted, and (c) Isometric view of the mechanism.

4.1.2 Position Prediction Algorithm

Before beginning testing, we derive the position prediction algorithm that inherits the previously formulated force models in Equations 2.16 and 2.17, and uses rotation matrices to determine the static equilibrium position of the delta mechanism as the actuators are pressurized. The inputs to the algorithm are the air inlet pressures for all actuators, and all model parameters, $A_{z,eff}$, $W_{y,eff}$, k_s, k_θ and L_0, are known from the static characterization tests.

A model of the soft delta mechanism is presented in Figure 4.5. In order to calculate the net force output from the three actuator system at the center point, we define rotation matrices to relate the reference frames of each of the actuators, O_1, O_2 and O_3, to the world frame, O :

$$ {}^0R_1 = \begin{pmatrix} 1 & 0 & 0 \\ 0 & 1 & 0 \\ 0 & 0 & 1 \end{pmatrix} \tag{4.1} $$

$$ {}^0R_2 = \begin{pmatrix} 1 & 0 & 0 \\ 0 & -0.5 & -0.866 \\ 0 & 0.866 & -0.5 \end{pmatrix} \tag{4.2} $$

$$ {}^0R_3 = \begin{pmatrix} 1 & 0 & 0 \\ 0 & -0.5 & 0.866 \\ 0 & -0.866 & -0.5 \end{pmatrix} \tag{4.3} $$

where ${}^0R_1$, ${}^0R_2$, and ${}^0R_3$ are the rotation matrices for the three actuators' reference frames with respect to the world frame, O.

The force vector for each actuator in the local frame, ${}^{\mathrm{i}}F_{\mathrm{i}}$, can be defined as:

$$ {}^{\mathrm{i}}F_{\mathrm{i}} = \begin{pmatrix} 0 \\ {}^{\mathrm{i}}F_{y_{\mathrm{i}}} \\ {}^{\mathrm{i}}F_{z_{\mathrm{i}}} \end{pmatrix} \tag{4.4} $$

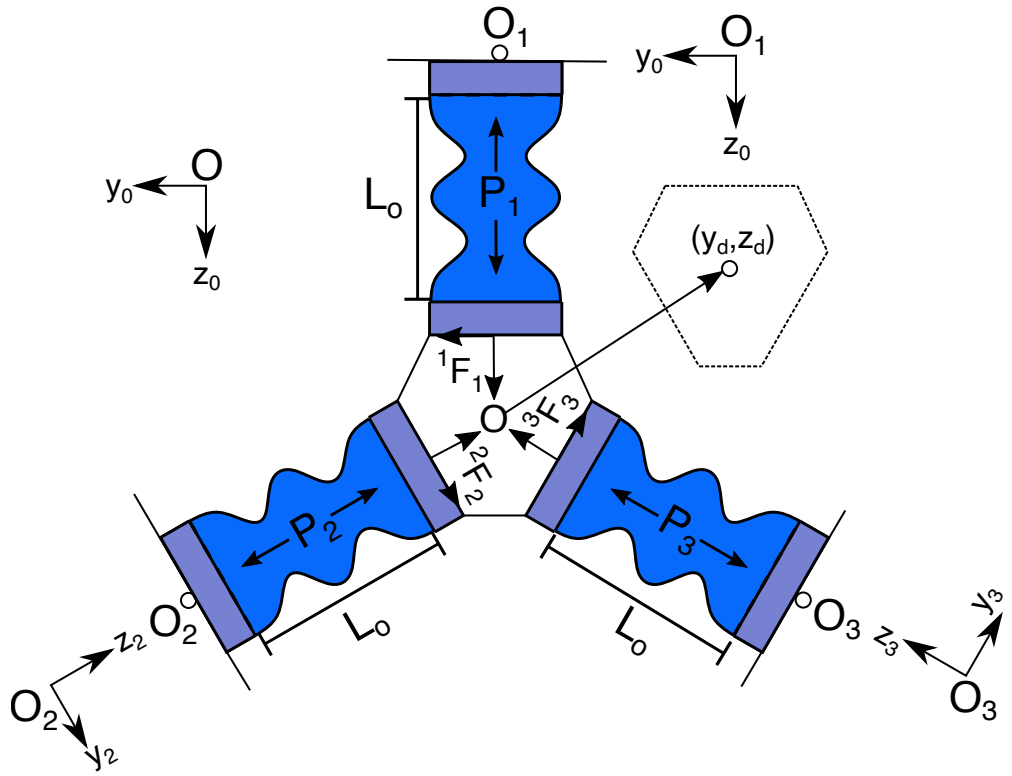

Figure 4.5. Model of Soft Delta Mechanism, using three soft actuators, to predict location of feedback head, O, shown as (y_d, z_d), to achieve quasi-static equilibrium, given the inlet pressures, P_1, P_2 and P_3. From [64] ©IEEE 2022.

where i $= 1, 2, 3$. For this planar configuration of actuators, we assume that forces into the plane (along the x-axis) for each actuator is negligible.

The rotation matrices from Equations 4.1, 4.2 and 4.3 can be used to transform each of the force vectors to the origin's reference frame:

$$F_{(1,2,3)} = {}^{0}R^{\mathrm{T}}_{(1,2,3)} \cdot {}^{(1,2,3)}F_{(1,2,3)} \tag{4.5}$$

These rotated forces can then be summed and set to zero assuming static equilibrium constraints:

$$F_{\text{total}} = F_1 + F_2 + F_3 = \mathbf{0} \tag{4.6}$$

Lastly, we write the ΔL and θ for each actuator in terms of y_d and z_d, which are the final coordinates for the center of the delta after pressurization.

Using the pressure of each actuator as the inputs to the system, this results in a system of two equations and two unknowns, y_d and z_d. Solving the equations in the other direction, i.e. inputting desired position and outputting actuator pressures, results in two equations and three unknowns. This implies that more than one set of pressures can lead to the same predicted position, if we can supply positive and negative pressures. This is in accordance with our understanding of degrees of freedom. However, since we only apply positive pressures in this thesis, the third actuator can be used to expand the workspace of the delta mechanism.

With the prediction model complete, we can develop MATLAB code that performs the aforementioned calculations for the forward direction, given the air inlet pressures as inputs, using the symbolic solver to solve the static equilibrium equations to obtain the y- and z-coordinates of the feedback head, O. Taking it a step further, we perform a simulation to determine the edges of the delta mechanism's workspace given the range of operating pressures, 0 to 41.37 kPa (6 psi), for each actuator. Additionally, this simulation provides us with vital information of the feedback head positions throughout the workspace such that we can choose air inlet pressures corresponding to interesting positions, as well as ensure a good spread of testing positions in terms of magnitude and direction from origin. This simulation is performed on MATLAB by iteratively running the symbolic solver for the feedback head's position developed earlier, for every possible air inlet pressure with a resolution of 6.895 kPa (1 psi) for each of the three actuators. This results in a point map of 343 positions representing the workspace of the delta mechanism given the pressure resolution of 6.895 kPa (1 psi) and range of 0 to 41.37 kPa (6 psi) (Figure 4.6). From this figure, the workspace symmetry is clearly visualized and hence, seven distinct points are selected from one of the four symmetrical workspace areas with edge cases, and spread in magnitude and direction as criteria. The selected points with their air inlet pressures are tabulated in Table 4.1.

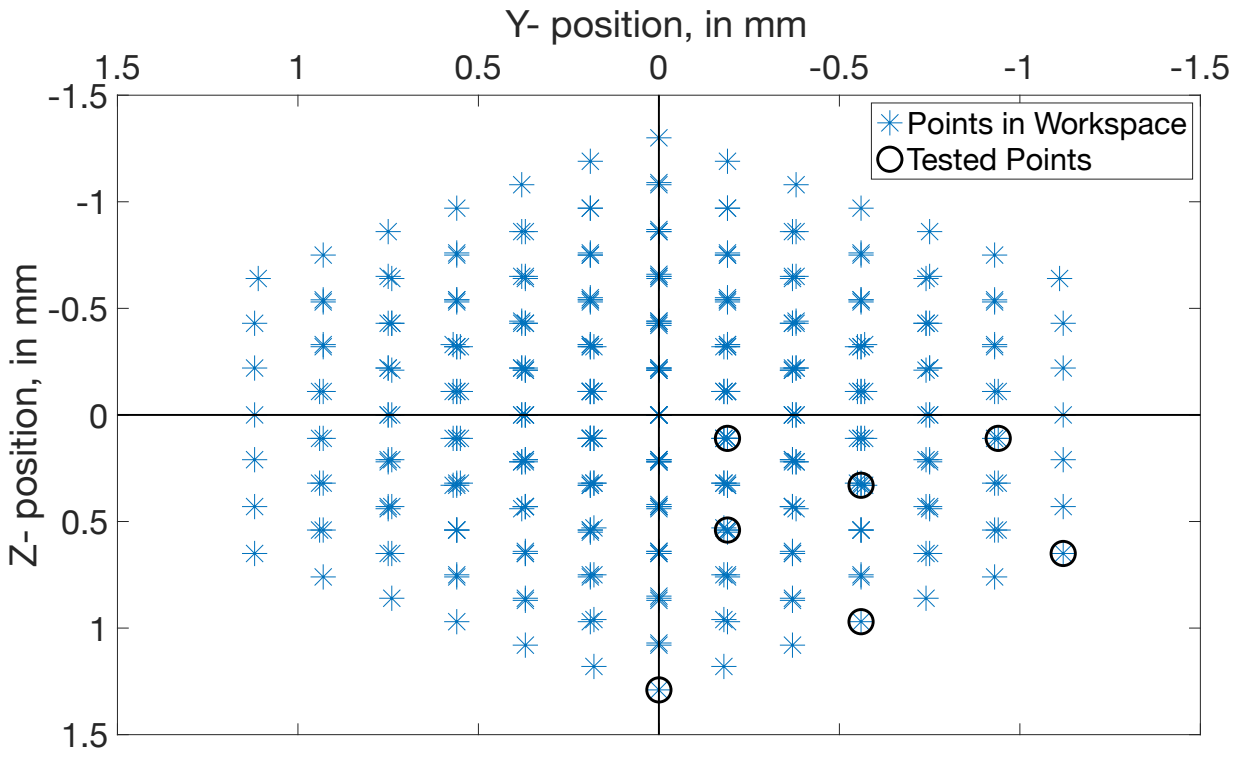

Figure 4.6. Workspace map of the delta mechanism. The symmetry of the workspace is clearly visible. The z- and y- displacements of the feedback head range from -1.29 mm to 1.29 mm, and -1.12 mm to 1.12 mm respectively. For testing, seven distinct points in one of the four symmetrical workspaces are chosen strategically and are indicated with black circles in the point map.

Table 4.1. Inlet Pressures and Locations of Selected Testing Points

P_1, **in kPa (psi)**	P_2, **in kPa (psi)**	P_3, **in kPa (psi)**	(y_d, z_d) **Location, in mm**
41.37 (6)	41.37 (6)	0 (0)	(-1.12 , 0.65)
41.37 (6)	20.69 (3)	0 (0)	(-0.56 , 0.97)
41.37 (6)	0 (0)	0 (0)	(0 , 1.29)
27.58 (4)	41.37 (6)	6.90 (1)	(-0.94 , 0.11)
34.48 (5)	34.48 (5)	13.79 (2)	(-0.56 , 0.33)
27.58 (4)	13.79 (2)	6.90 (1)	(-0.19 , 0.54)
34.48 (5)	34.48 (5)	27.58 (4)	(-0.19 , 0.11)

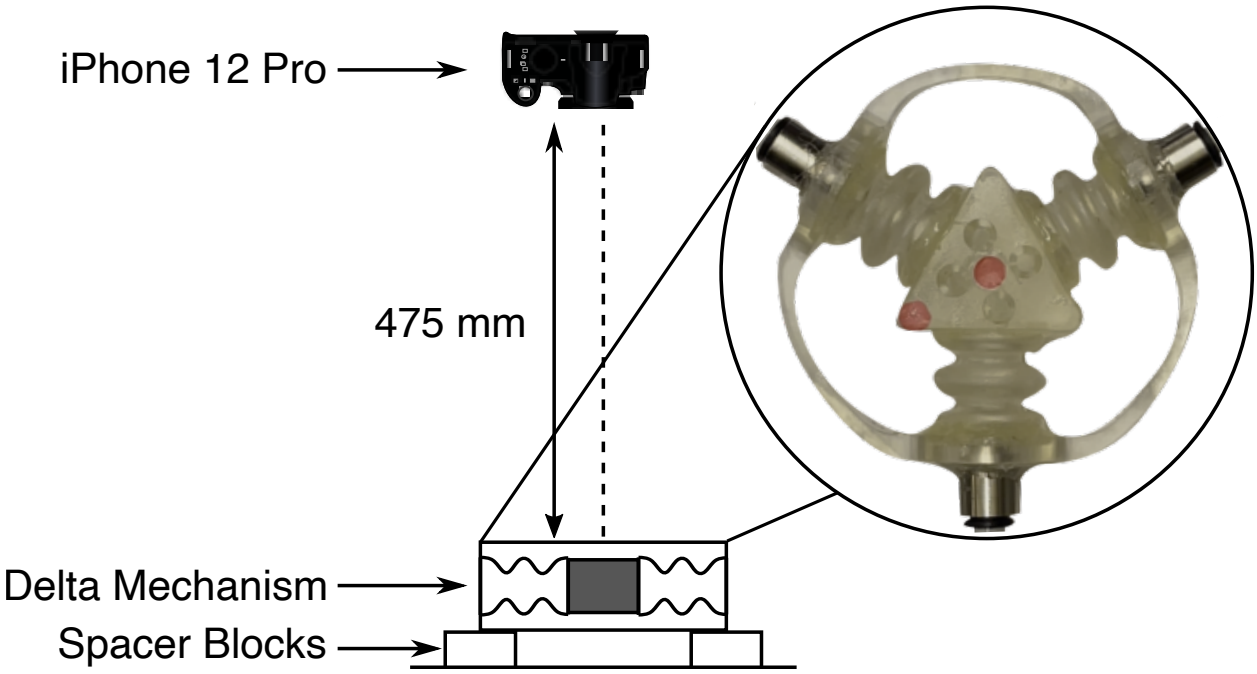

Figure 4.7. Experiment schematic for position prediction test on a delta mechanism. The camera used is an iPhone 12 Pro in video mode at 30 fps with a focal length of 52mm, and is supported on a tripod. The red dots on the feedback head are used for blob detection in MATLAB. From [64] ©IEEE 2022.

4.1.3 Experiments and Results

We are now ready to conduct the experiments. Here, each actuator is individually and independently pressurized using the QB3 pressure regulator. The experimental setup (Figure 4.7) captured image data of the feedback head's movements upon pressurization and depressurization for each set of (y_d, z_d) points tested. The camera used was an Apple iPhone 12 Pro camera, in video mode, supported on a tripod 475 mm away from the top of the feedback head (Figure 4.7). For each test, static frames from the recorded video were selected to record initial (zero pressures), actuated, and final (zero pressures post actuation) positions. The actuated position frame was selected after 20 seconds from bellows actuation to limit viscous effects and to ensure static behavior of mechanism. The selected frames were then analyzed through blob analysis using MATLAB's computer vision toolbox to calibrate measurement unit conversions, check for image distortion, record y- and z- displacements of

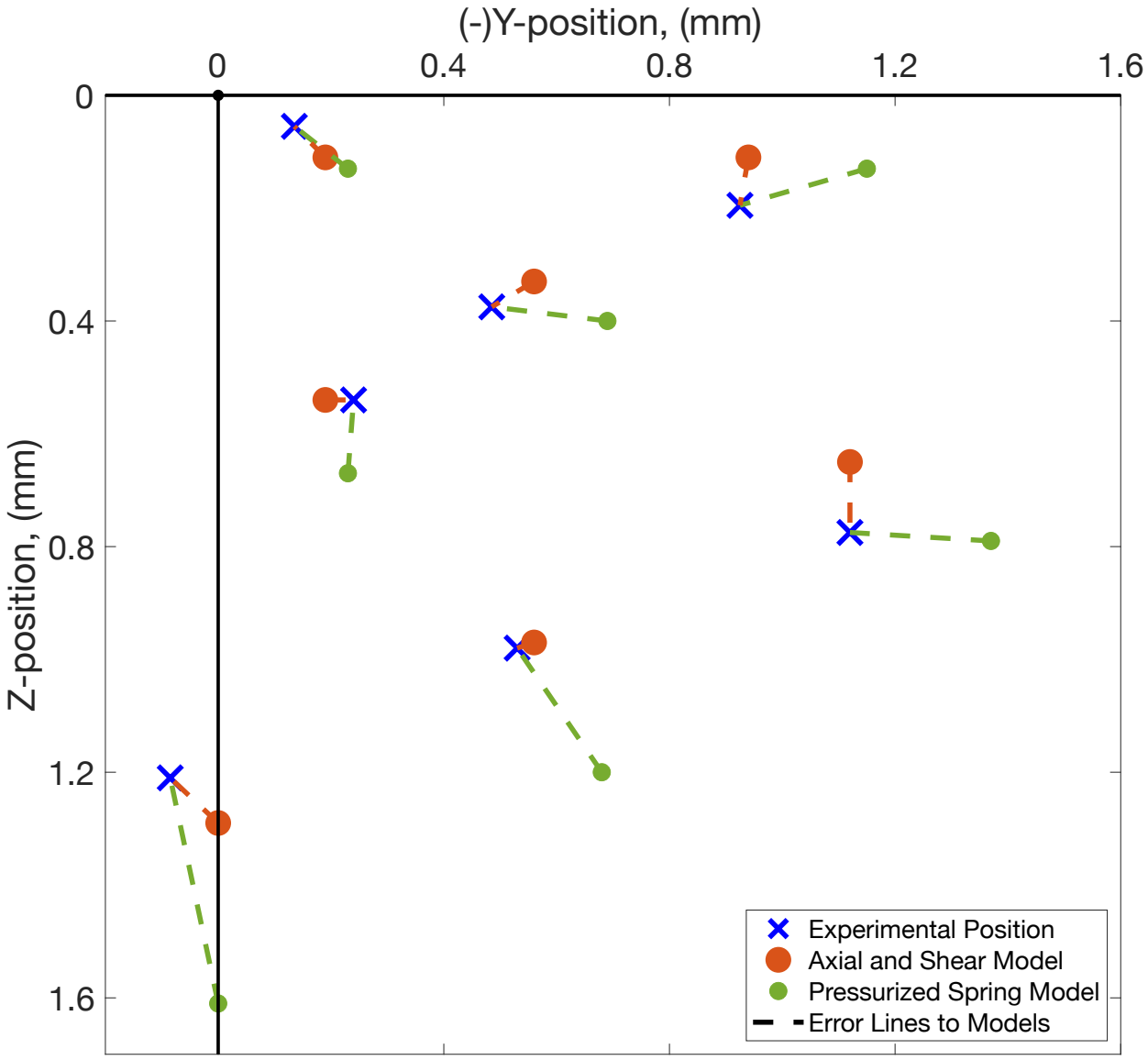

Figure 4.8. Experimental results of soft delta mechanism demonstration to predict feedback head's posititon, O, given inlet air pressures and comparing results of presented model, namely the axial and shear force model, to previous model, namely pressurized spring model. Significant improvement in prediction is clearly visible and dashed lines are indicative of model error. From [64] ©IEEE 2022.

the feedback head upon actuation and verify elastic range application of bellows actuators by studying hysteresis effects. The blob analysis is performed by first, thresholding the color of the red circles (blobs) on the feedback head in the HSV space using the color thresholder MATLAB application, and using the threshold limits in code to create a binary mask of the selected frames. Thereafter, a disk-shaped structuring element is used to remove noise from the image before comparative analysis is performed between frames.

Each test was performed twice to show repeatability, and the mean value of the center position is shown in Figure 4.8 along with the point predicted by the developed axial and shear force model. We additionally try to predict the position using the model from a previous work which characterized a soft bellows actuator as only a pressurized spring model [26]. This pressurized spring model is constructed using the similar Equations 2.16 and 2.17 but by setting k_θ and $W_{y,\mathrm{e}ff}$ to zero, since those are the shear-specific components introduced in this thesis. Finally, the absolute model error for the axial and spring model and for the pressurized spring model are shown in Figure 4.9.

It is evident that the axial and shear model presented in Equations 2.16 and 2.17, well predicts the final locations of the center point of the delta setup, even though the model was developed only for single actuators. This is especially true as compared to the previous pressurized spring model [26], which significantly over predicts the total magnitude of deflection and the amount of shear achieved. This improvement can be further quantified in Figure 4.9 which presents the absolute model errors for the magnitude of experimental positions in this test. The axial and shear model has an average error of 0.04 mm and a maximum error of 0.08 mm, compared to average and maximum errors of 0.22 mm and 0.40 mm respectively for the pressurized spring model. Additionally, while the pressurized spring model's prediction worsens the further out it is actuated, there is no correlation between error and the magnitude of position for the axial and shear model.

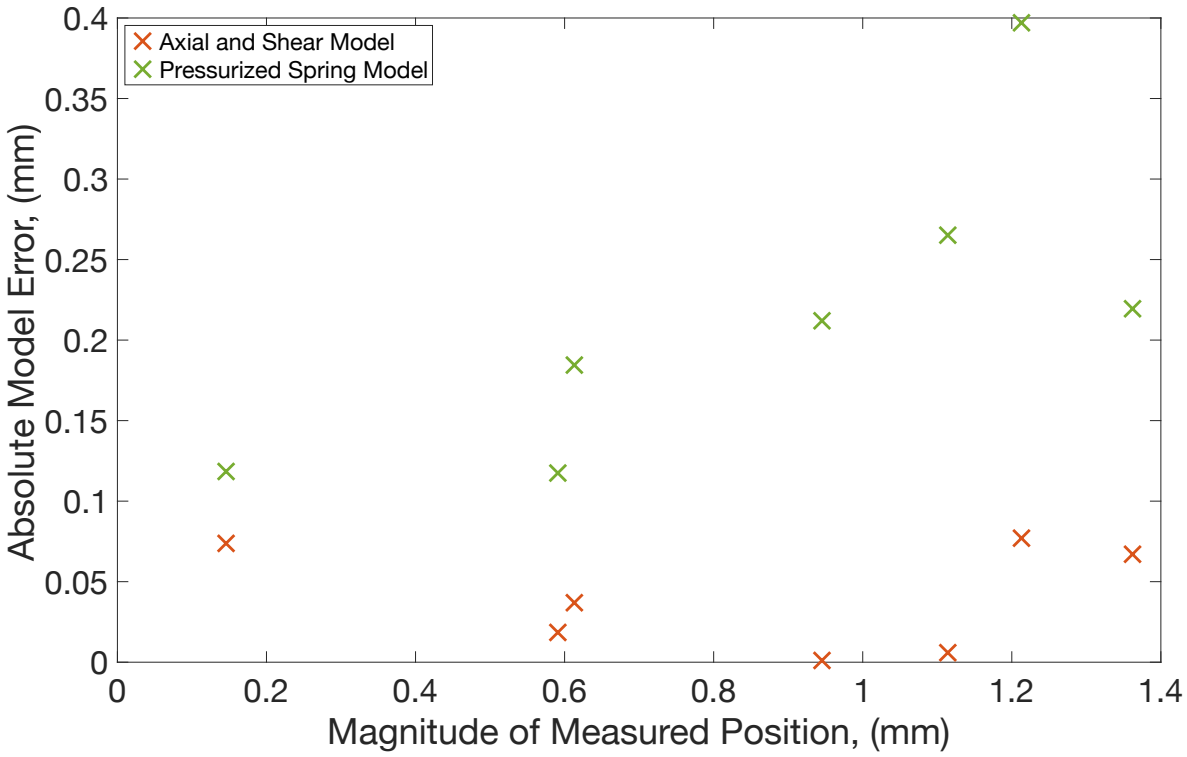

Figure 4.9. Absolute model error in magnitude of measured position for both presented (axial and shear model) and previous (pressurized spring) model. There is significant improvement in model prediction with mean model error of 0.04 mm for presented model and 0.22 mm for previous model. Modified from [64] ©IEEE 2022.

4.2 Floating Actuator Mechanism

With the thorough design and analysis of the delta mechanism, we were able to conclude significant improvement in position prediction of the feedback head's position as compared to previous work, which models the soft actuator as only a pressurized linear spring. In this section, we expand our analysis to a five-actuator system with four degrees-of-freedom and having a floating actuator, to evaluate the position prediction of the two feedback heads when some of the assumptions made during the 1-DOF actuator characterization break down due to potential of small amounts of bending of the actuators. Similar to the analysis of the delta mechanism, we compare the position prediction from the presented model to the previous pressurized spring model.

4.2.1 Design and Manufacturing

Since the delta mechanism design worked well, we will incorporate some design features from it into the floating actuator mechanism. To begin, as shown in Figure 4.1(b), this mechanism consists of five actuators and two feedback heads. Each feedback head is actuated directly by three actuators, similar to the delta mechanism, but they share a common actuator, the floating actuator, which makes their movements coupled. The floating actuator is called so because it is not directly fixed to the outer support, therefore allowing it to have displacements on both ends of itself. To design this system, we use actuators that are identical in design to the one analyzed in Sections 2 and 3. This enables us to use the same model constants for Equations 2.16 and 2.17 without performing additional testing.

The next step in the design process are the feedback heads. They have a similar design to the feedback head in the delta mechanism, but with modifications based on evaluation of previous design, and adaptation to the floating mechanism requirements. Firstly, they are printed using the draft resin by Formlabs instead of the clear resin because of faster printing times, and since no significant stresses are observed at the feedback heads in the operable pressure ranges, we are not compromising on the heads' structural integrity. The draft resin has an ultimate tensile strength of 36 MPa and 5% elongation at break post cure at room temperature, as compared to 65 MPa and 6.2% for the clear resin [69], [76]. The heads have a smaller triangular cross-section to reduce material usage and mass, while still accommodating the actuators. The equilateral triangular cross-section now has a side of 32 mm with 1.5 mm radius fillets to round the edges. The height of the feedback heads is still 26 mm. Moreover, the same mating strategy from the delta mechanism is used to mate the actuators to the feedback heads, where a revolved cut of depth 2 mm, and inner and outer diameters of 18 mm and 22.50 mm respectively is used to sufficiently embody the actuator flanges of 3 mm length. Once again, the flexible epoxy (DP110, 3M) is used to secure the joint. The modified feedback head is shown in Figure 4.10. However, the two feedback heads of the floating actuator mechanism are not exactly similar. One of them has an air passage hole designed into it to function as the air inlet to pressurize the floating actuator independently, as shown in Figure 4.10(c). The air passage hole of diameter 3 mm

is added to the bottom of the feedback head, and opens into the floating actuator through its mating surface on this feedback head. The hole is added to the bottom instead of the top to avoid air tubes from blocking the camera's view of the feedback heads, and to make the air tubes less susceptible to external movements which could cause unintentional movement of the feedback head. An elbow connector (1901K232, McMaster Carr) with a barbed end for the air tube, and a tube stem end for the air inlet end is used to change the direction of air supply for ease of assembly. Consequently, a counterbore hole of diameter 6.4 mm and depth 7.5 mm is added at the inlet of the air passage hole to house the elbow connector sufficiently. Finally, hot glue is used to hermetically secure this joint.

With the feedback heads and the actuators designed and assembled, the next step is to design the outer ring for the floating actuator mechanism. Once again, we print the outer ring using the draft resin instead of the clear resin due to the faster prototyping possibilities. We are able to do this without compromising the structural integrity of the ring since no significant stresses are expected on the outer ring that would require a stronger material in the operating pressure range. For the mating surfaces to the four supported actuators, a similar approach to the delta mechanism is taken. The circular cross-section of the mating surfaces is 26 mm to allow for a larger thicker wall-actuator distance of 2 mm as the actuator of outer diameter 22 mm is mounted. The same design for the extruded cut is used for sufficiently embodying the actuator flanges. To use a similar air inlet strategy as for the feedback head, straight barbed to tube stem connectors (5779K373, McMaster Carr) are used. To house these in the mating surfaces, a through hole of 8 mm is made and hot glue is used to hermetically secure the joint. Next, the outer ring needs to be closed by joining the mating surfaces. This is done by extending flat surfaces of width 5 mm and thickness 10 mm from the mating surfaces in towards the center of the mechanism until they intersect. For the other ends, a box-like approach is utilized to close off the geometry symmetrically. A 2D sketch of the underlying geometry of the outer ring, similar to a symmetric hexagon, and the outer ring CAD model are shown in Figure 4.11. The CAD model for the complete assembly is shown in Figure 4.12.

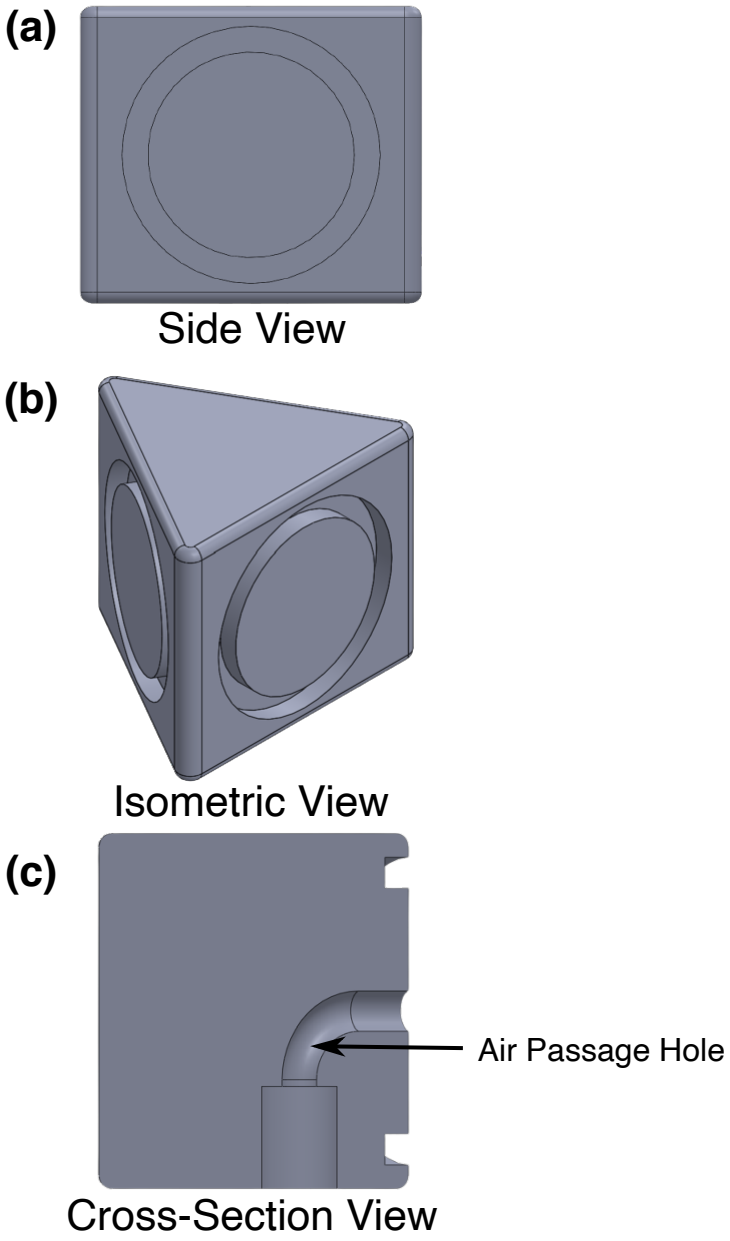

Figure 4.10. CAD model of modified feedback heads for the floating actuator mechanism. (a) Side view of the modified feedback head where the dimensions are noticeably reduced as compared to the delta mechanism's feedback head, (b) Isometric view of the modified feedback head, and (c) Cross-section view of the modified feedback head showing the air passage hole for pressurization of the floating actuator.

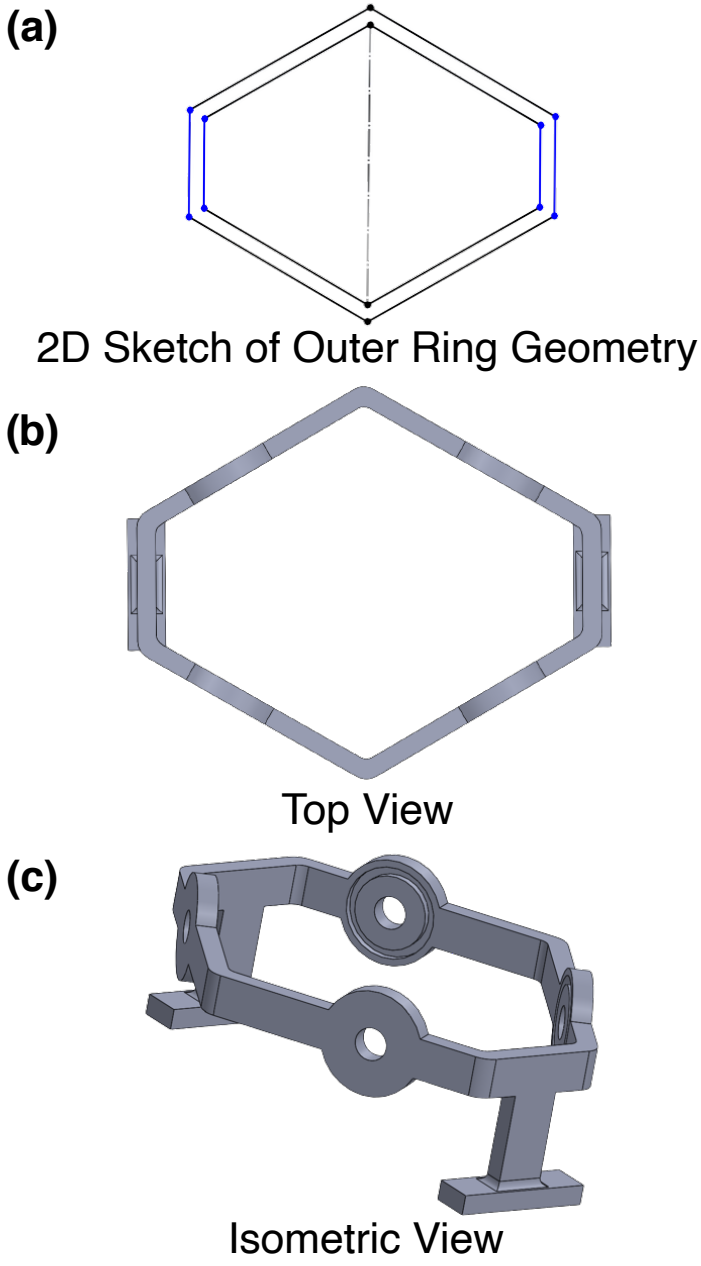

Figure 4.11. CAD model of outer ring for the floating actuator mechanism. (a) 2D sketch of the outer ring geometry showing the underlying hexagonal cross-section, (b) Top view of the outer ring, and (c) Isometric view of the outer ring.

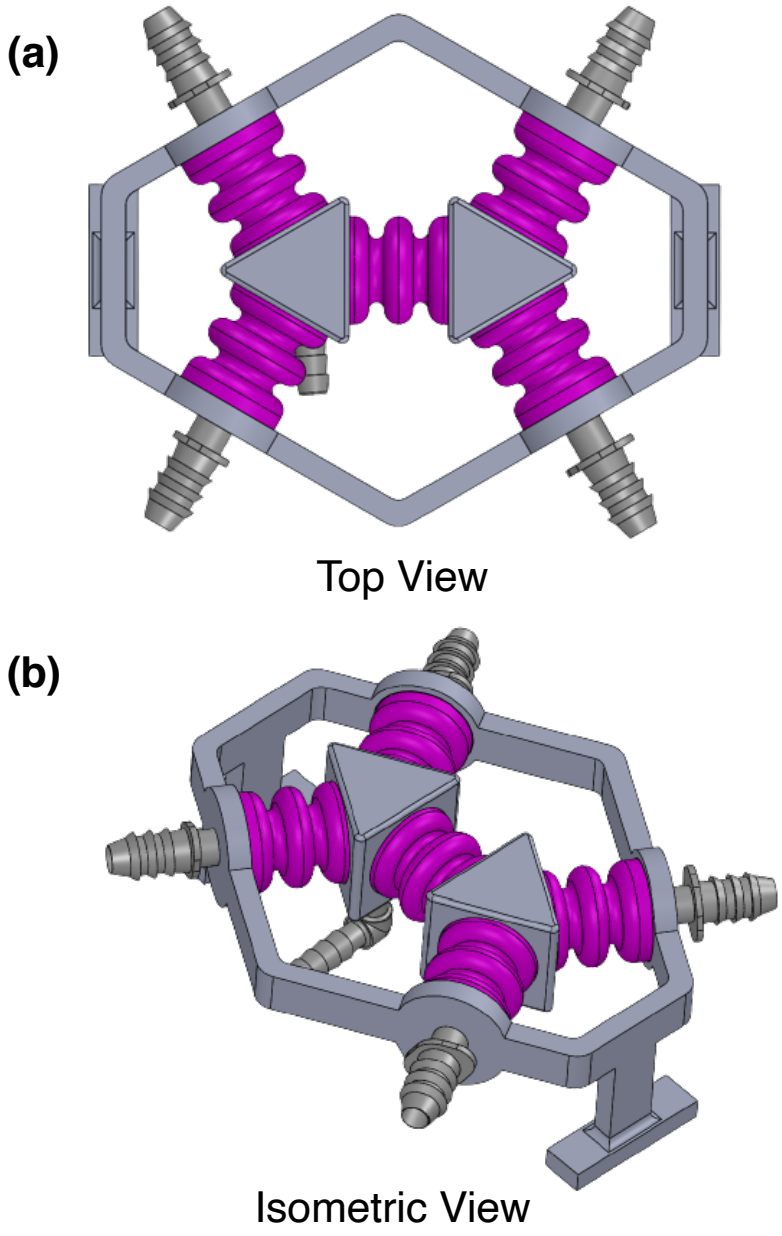

Figure 4.12. CAD model of the assembled floating actuator mechanism. (a) Top view showing the placement of the actuators and feedback heads in their resting state, and (b) Isometric view of the assembled floating actuator mechanism.

4.2.2 Position Prediction Algorithm

With the design now complete and the mechanism manufactured, we should use the presented models in Equations 2.16 and 2.17 to create a position prediction algorithm for both the feedback heads in this mechanism. A schematic of the floating actuator mechanism is shown in Figure 4.13. The first step to the algorithm design is setting up the coordinate frames appropriately. We set the coordinate frames and origin on the feedback heads, O_L and O_R, to be fixed in space and oriented in the same direction as the world frame, O. Each actuator has its own respective coordinate frame which is attached to its respective support on the outer ring. The inputs to the floating actuator mechanism are the five air inlet pressures. In this algorithm, we assume that the left and right feedback heads move to positions (y_{d1}, z_{d1}) and (y_{d2}, z_{d2}) respectively to achieve static equilibrium upon pressurization. First, we define rotation matrices from the actuator reference frames, O_1, O_2, O_3, O_4, and O_5 to the world frame, O.

$$ {}^0R_1 = \begin{pmatrix} 1 & 0 & 0 \\ 0 & 0.5 & 0.866 \\ 0 & -0.866 & 0.5 \end{pmatrix} \tag{4.7} $$

$$ {}^0R_2 = \begin{pmatrix} 1 & 0 & 0 \\ 0 & 0.5 & -0.866 \\ 0 & 0.866 & 0.5 \end{pmatrix} \tag{4.8} $$

$$ {}^0R_3 = \begin{pmatrix} 1 & 0 & 0 \\ 0 & -0.5 & -0.866 \\ 0 & 0.866 & -0.5 \end{pmatrix} \tag{4.9} $$

$$ {}^0R_4 = \begin{pmatrix} 1 & 0 & 0 \\ 0 & -0.5 & 0.866 \\ 0 & -0.866 & -0.5 \end{pmatrix} \tag{4.10} $$

$$ {}^0R_5 = \begin{pmatrix} 1 & 0 & 0 \\ 0 & 1 & 0 \\ 0 & 0 & 1 \end{pmatrix} \tag{4.11} $$

where ${}^0R_1$, ${}^0R_2$, ${}^0R_3$, ${}^0R_4$, and ${}^0R_5$ are the rotation matrices for the five actuators' reference frames with respect to the world frame, O.

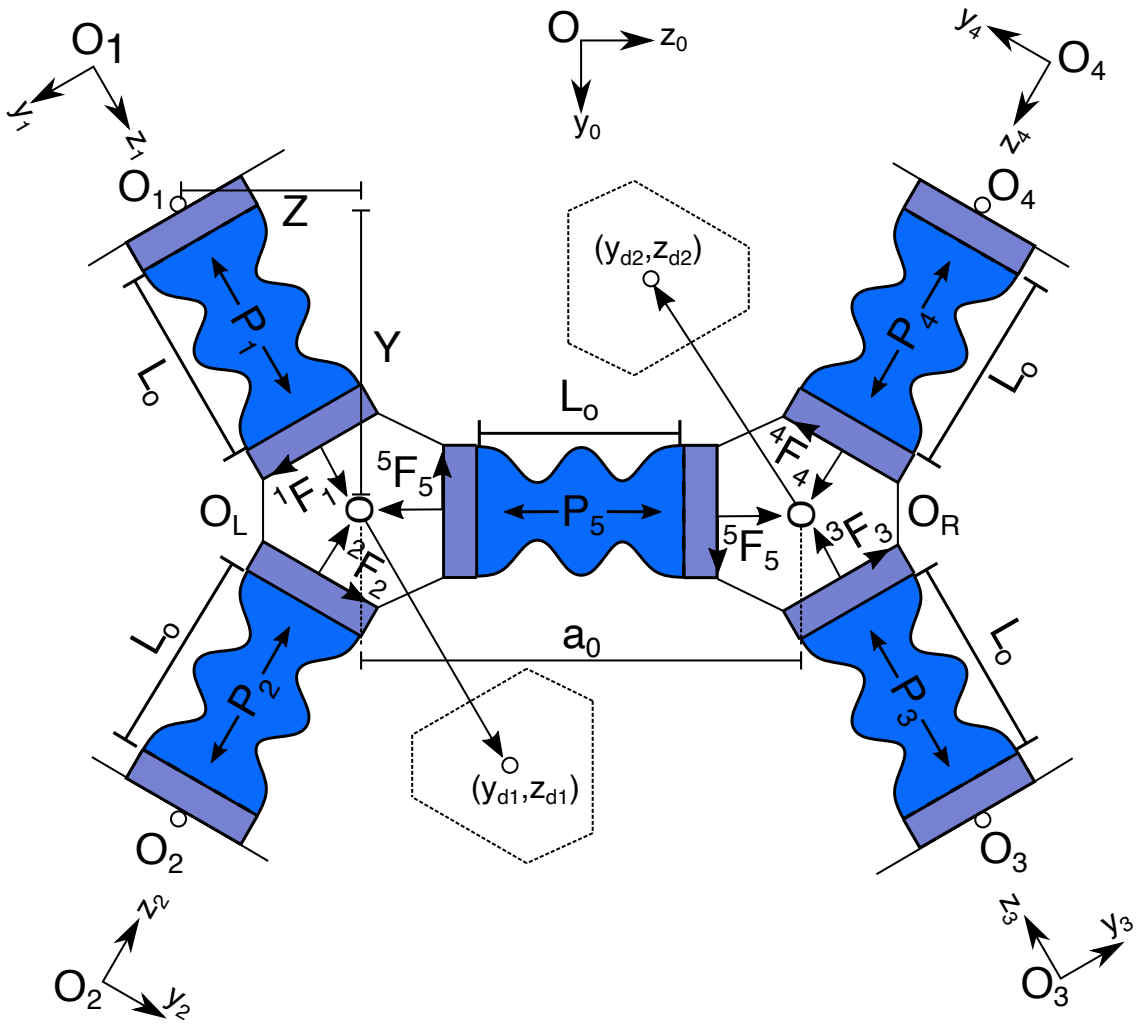

Figure 4.13. Model of Soft Floating Actuator Mechanism, using five soft actuators, to predict location of feedback heads, O_L and O_R, shown as (y_{d1}, z_{d1}) and (y_{d2}, z_{d2}), to achieve quasi-static equilibrium, given the inlet pressures, P_1, P_2, P_3, P_4, and P_5.

Next, we can define position vectors ${}^0p_1$, ${}^0p_2$, ${}^0p_3$, and ${}^0p_4$ with respect to the world frame, O, to define the location of the outer ring support. In order to do this, we establish some constants from the prototype design. Y and Z are the y- and z- components respectively of the distance from the outer ring support of actuator 1, O_1 to the left feedback head center with respect to the world frame. a_0 is the distance between the two feedback heads when the mechanism is in its natural resting state, with respect to the world frame. Hence, a_0 only has a z- component.

$$ {}^0p_1 = \begin{pmatrix} 0 \\ -Y \\ -Z \end{pmatrix} \tag{4.12} $$

$$ {}^0p_2 = \begin{pmatrix} 0 \\ Y \\ -Z \end{pmatrix} \tag{4.13} $$

$$ {}^0p_3 = \begin{pmatrix} 0 \\ Y \\ Z + a_0 \end{pmatrix} \tag{4.14} $$

$$ {}^0p_4 = \begin{pmatrix} 0 \\ -Y \\ Z + a_0 \end{pmatrix} \tag{4.15} $$

The values of Y, Z, and a_0 from the CAD model were obtained to be 26.98 mm, 15.58 mm, and 39.70 mm. Assuming the feedback heads reach equilibrium at ${}^0p_{d1} = (0, y_{d1}, z_{d1})^T$ and ${}^0p_{d2} = (0, y_{d2}, z_{d2})^T$, a symbolic equation can be created to obtain the position of the feedback heads from the outer ring supports with respect to their respective coordinate frames using Equation 4.16 for the left feedback head, O_L, and Equation 4.17 for the right feedback head, O_R, both of which have been derived from vector math.

$$ {}^{\mathrm{i}}p_{\mathrm{d1}} = {}^0R_{\mathrm{i}}^{\mathrm{T}}({}^0p_{\mathrm{d1}} - {}^0p_{\mathrm{i}}) \tag{4.16} $$

$$^{\mathrm{j}}p_{\mathrm{d2}} = {}^{0}R_{\mathrm{j}}^{\mathrm{T}}({}^{0}p_{\mathrm{d2}} - {}^{0}p_{\mathrm{j}}) \tag{4.17}$$

where, i = 1,2 and j = 3,4 and represents the outer ring support the respective actuator is attached to. Thereafter, we can use the y- and z- components of ${}^{(1,2)}p_{d1}$, and ${}^{(3,4)}p_{d2}$ to calculate the change in length, ΔL, and the shear angle, θ, for each of the four supported actuators in the symbolic notation. For the floating actuator, we can determine ΔL and θ symbolically through the location of the two feedback heads since the length of the floating actuator is the distance between the feedback heads, and the shear angle is the angle subtended by a line joining the two points in the equilibrium position to the line joining the two points in the resting position, about the x-axis.

With this knowledge, we can compute the axial and shear forces applied by the actuator in their respective coordinate frames using Equations 2.16 and 2.17. Thereafter, we can use a similar approach from Equations 4.4 and 4.5 to assemble the forces for each actuator in a vector, and rotate it to the world frame, O. Here, we can apply the equilibrium equation for the sum of forces to be zero for each feedback head to obtain four non-trivial equations with four unknowns, y_{d1}, z_{d1}, y_{d2}, and z_{d2}. However, we must be careful with the summation because the floating actuator forces act in the opposite direction on the left feedback head. Hence, the equilibrium equations can be written as in Equations 4.18 and 4.19 for the left and right feedback heads respectively.

$$F_{\mathrm{total,left}} = F_1 + F_2 - F_5 = \mathbf{0} \tag{4.18}$$

$$F_{\mathrm{total,right}} = F_3 + F_4 + F_5 = \mathbf{0} \tag{4.19}$$

where $F_{\mathrm{total,left}}$ and $F_{\mathrm{total,right}}$ are the sum of all forces acting on the left and right feedback heads respectively. These equations can be solved using the MATLAB symbolic solver to obtain the predicted positions for the feedback heads for any set of actuator pressures. Similar to the delta mechanism, we perform a workspace analysis simulation to determine the edges of the parallel actuator mechanism's workspace given the range of operating pressures, 0 to

41.37 kPa (6 psi) for each actuator with a resolution of 10.343 kPa (1.5 psi). This results in a workspace map of 3125 configurations which provides a robust visualization of the workspace of both feedback heads. The resulting workspaces are presented in Figure 4.14.

The workspace ranges of the left feedback head are maximum z- displacement of 1.89 mm and minimum z- displacement of -1.94 mm, and maximum y- displacement of 1.30 mm in both directions. Similarly, for the right feedback head- the maximum z- displacement is 1.94 mm and minimum z- displacement is -1.89 mm., and maximum y- displacement of 1.30 mm in both directions. It is important to note that although the two workspaces might look similar, they are actually quite different. This is because two points which might appear to be at the same location on both plots might be achieved using different actuator pressure combinations. To elaborate this further, we analyze the change in actuator length, ΔL_5, and shear angle of the floating actuator, θ_5, which provides a good indication of the relative location of the two feedback heads in Figure 4.15. Here, we can clearly see that a shear angle range of around 6 degrees is achieved by the actuator with greater than 3 mm of length change verifying that there is relative "twist" and change in length between the two feedback heads.

4.2.3 Experiments and Results

Once again, the workspace maps look fairly symmetric but due to the increased complexity of five actuation pressures, we will utilize a different approach for robust testing. We identify interesting points from the workspace such as those where maximum displacements occur and those where the shear angle of floating actuator is maximized. Thereafter, we use a random number generator to obtain randomized pressure inputs for each of the five actuators such that a total of 20 test sets are created. The experimental test setup is similar to that for the delta mechanism where an iPhone 12 Pro camera supported on a tripod 475 mm away, in video mode is used to capture the displacements of the feedback heads as the actuators are pressurized and depressurized. Each actuator is individually pressurized using a pressure regulator that is controlled using a microcontroller (Uno, Arduino). For verification

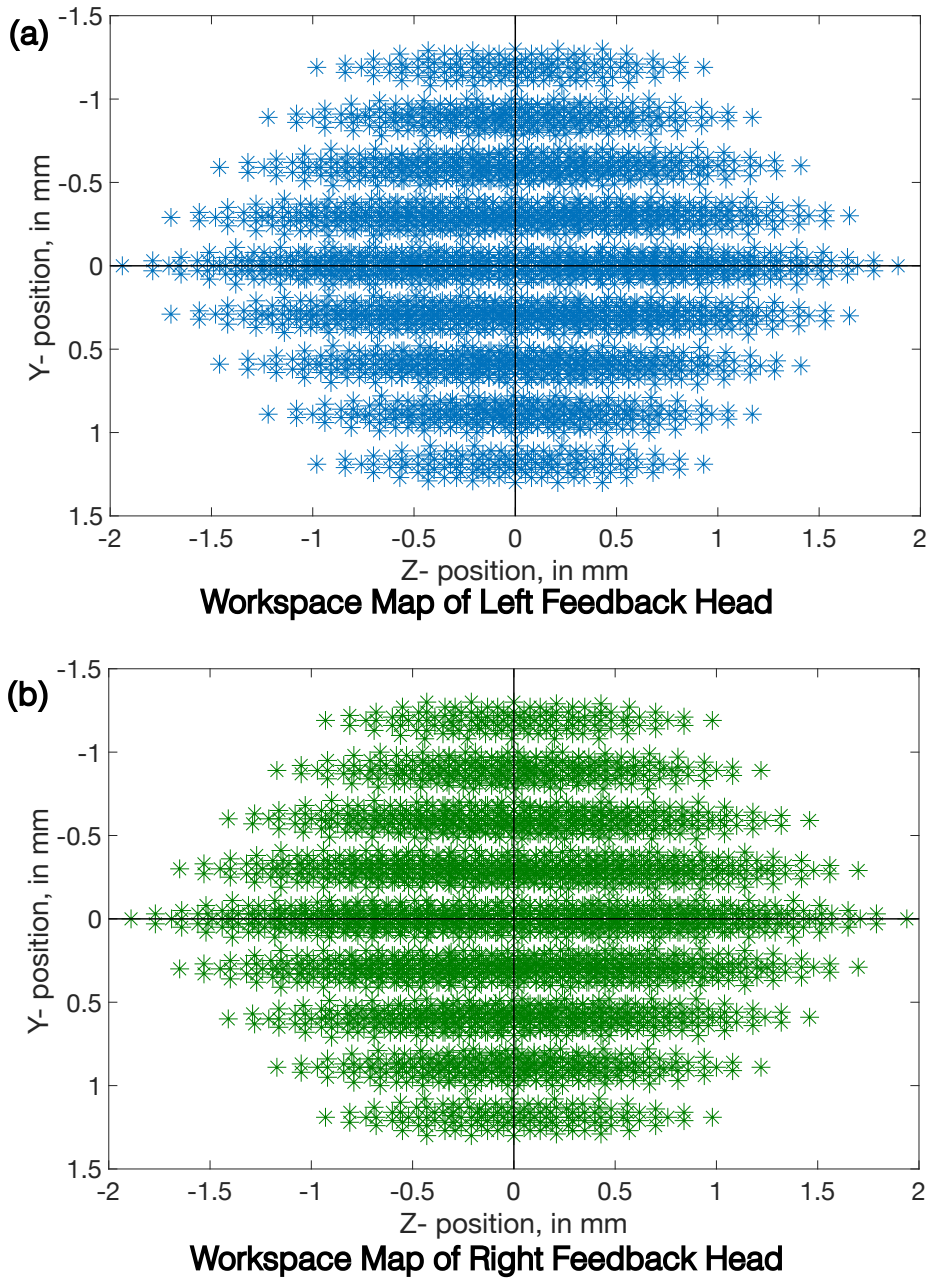

Figure 4.14. Workspace map of the floating actuator mechanism. (a) Workspace map for the left feedback head, with z- and y- displacements of the feedback head ranging from -1.94 mm to 1.89 mm, and -1.30 mm to 1.30 mm respectively, and (b) Workspace map for the right feedback head, with z- and y- displacements of the feedback head ranging from -1.89 mm to 1.94 mm, and -1.30 mm to 1.30 mm respectively

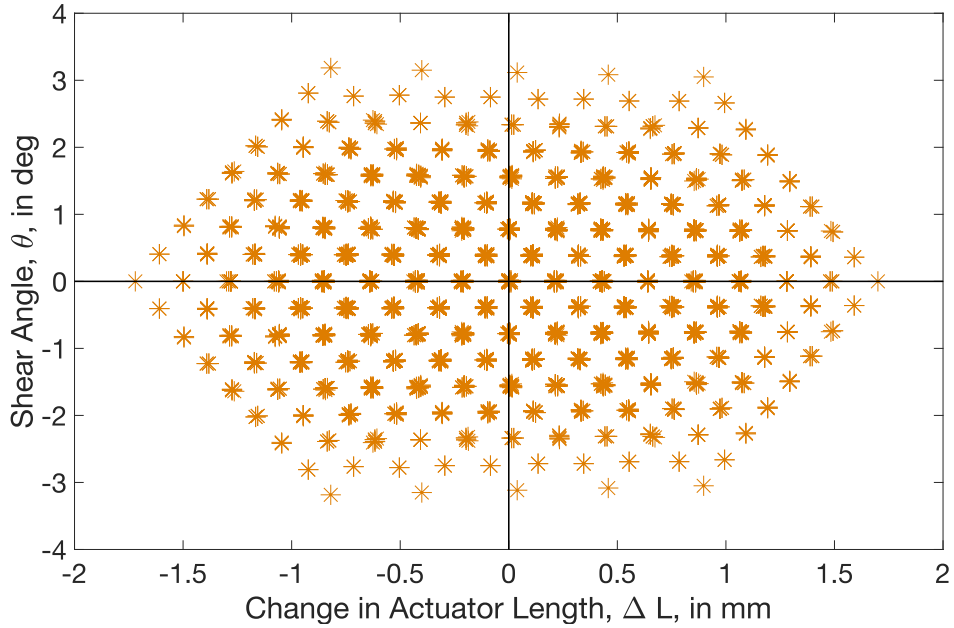

Figure 4.15. Movement of floating actuator in the workspace. This figure shows the theoretical range of change in actuator length and shear angle for the floating actuator, providing a good indication of the relative location of feedback heads.

of correct air inlet pressures, pressure sensors (HSCDANN030PGAA5, Honeywell) are used and continuously monitored through the microcontroller to avoid anomalies in data.

For each test, static frames from the recorded video were selected to record initial (zero pressures), actuated, and final (zero pressures post actuation) positions. Once again, MATLAB's computer vision toolbox is used to perform blob analysis on both feedback heads which have differently colored blobs for ease of identification. The analysis covers calibration of measurement unit conversions, checks for image distortion, study of hysteresis effects to ensure application in the elastic range of the actuators, and finally calculation of y- and z- displacements of the feedback heads upon actuation.

The results of the tests are shown in Figure 4.16. Similar to the analysis in the delta mechanism, we compare the presented axial and shear model to the previous pressurized spring model. This is done by setting k_θ and $W_{\text{y,eff}}$ to zero in Equations 2.16 and 2.17, since those are the shear-specific components introduced in this thesis.

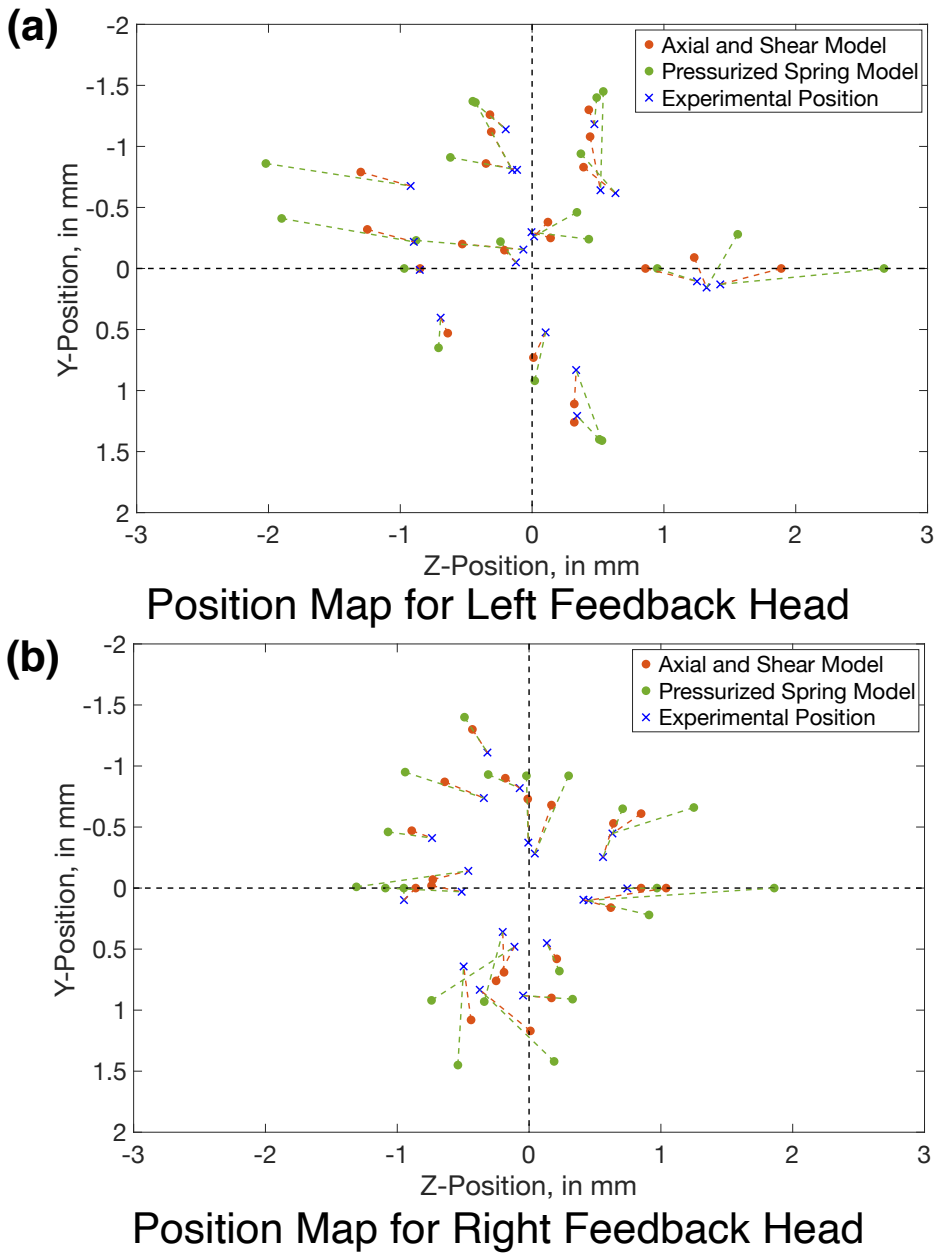

Figure 4.16. Experimental results of floating actuator mechanism demonstration to predict feedback heads' position, O_L and O_R, given inlet air pressures and comparing results of presented model, namely the axial and shear force model, to previous model, namely pressurized spring model. Significant improvement in prediction is clearly visible and dashed lines are indicative of model error.

From Figure 4.16, we can visually identify that the axial and shear model better predicts the position of the feedback heads, as compared to the previous pressurized spring model. Although, the errors are higher than that for the delta mechanism, that is to be expected due to the increased complexity of the floating actuator mechanism. Moreover, the errors appear to be larger for the right feedback head as compared to the left feedback head. It is also interesting to note that larger errors occur during large y- displacements of the feedback heads, which can be broadly interpreted as high shear angle tests for the floating actuator. This could be a consequence of the small angle approximation made during modeling in Chapter 2, or from the higher order effects seen in the axial forces where the axial cross-sectional area has different behavior for compression and elongation, as seen in Figure 3.17. Additionally, there are new sources of error where non-negligible out-of-plane movements were identified during testing at higher pressures. These can have a detrimental impact on the experimental data collected since our analysis assumes planar movements only. These out-of-plane movements can arise due to misalignment of the actuators' axes to the feedback heads' center of masses, causing the latter to have movements along the x- axis. To quantify the prediction errors of both models, the magnitudes of errors of both feedback heads are presented in Figure 4.17. Relative error is not a good measure for error quantification in this test due to the testing of multiple small magnitude positions. In these cases, the relative error can be unusually high despite the error magnitude being in range.

From Figure 4.17, one can clearly see the improvement in the axial and shear model as compared to the pressurized spring model. The mean absolute error for the presented axial and shear model for the left and right feedback heads are 0.26 mm and 0.28 mm respectively, as compared to 0.53 mm and 0.56 mm for the left and right feedback head position prediction using the pressurized spring model. The presented model shows a mean improvement of 50% in absolute error as compared to the previous model. Since an absolute error of 0.27 mm can be significant for small magnitude movements, care needs to be taken when implementing this model for such use cases. This error might arise due to the bending of actuators as it moves through the workspace, and future work should include this deformation mode in the 1-DOF actuator characterization for more accurate results. Altogether, it is evident that the model presented in Equations 2.16 and 2.17 results in improved prediction of the feedback

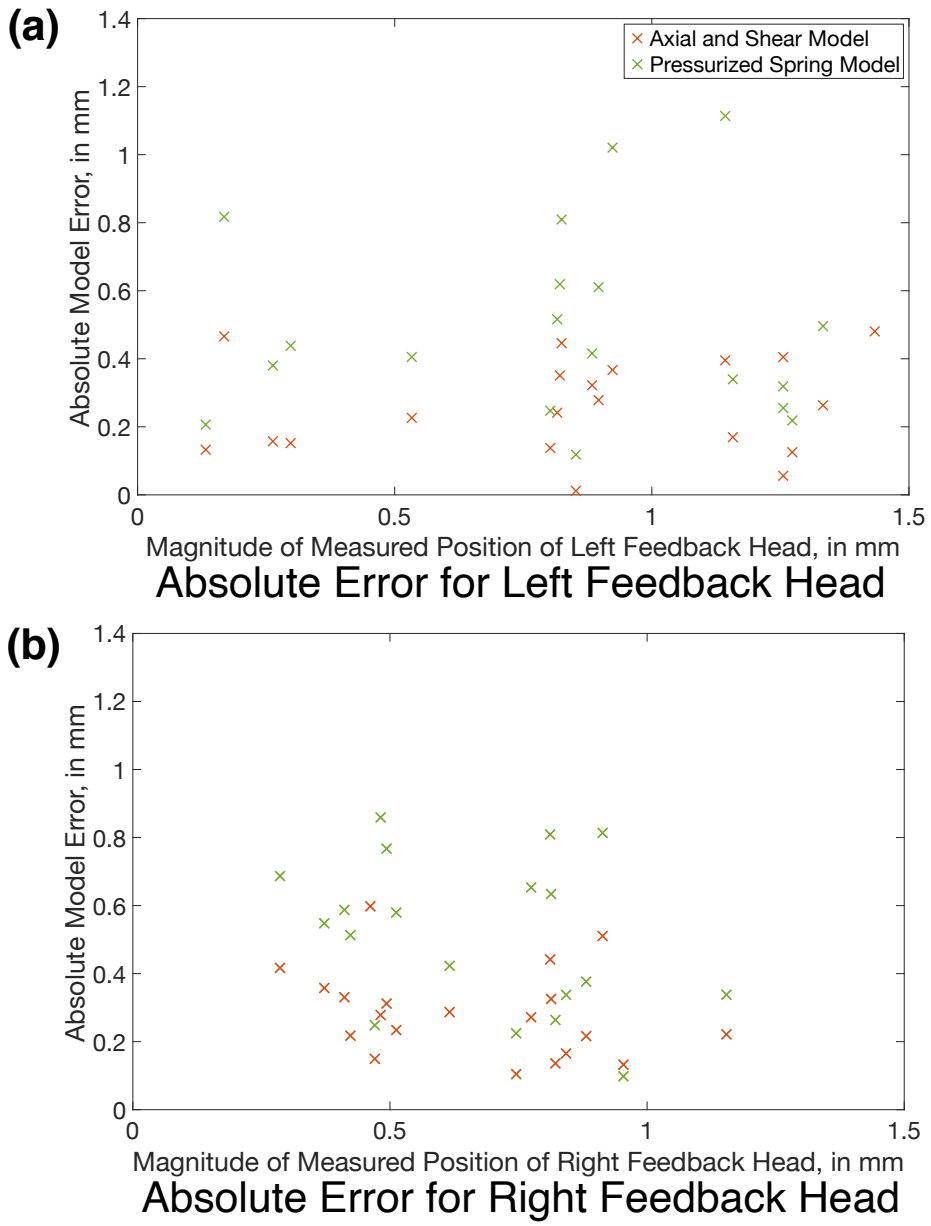

Figure 4.17. Absolute model error in magnitude of measured position for both presented (axial and shear model) and previous (pressurized spring) model. There is significant improvement in model prediction with mean model error of 0.26 mm and 0.28 mm for the left and right feedback heads respectively using the presented model, as compared to 0.53 mm and 0.56 mm for left and right feedback heads respectively using the previous model.

heads' positions, and that using 1-DOF actuators to model complex parallel networks is a viable approach for preliminary predictions of mechanism movements. Moreover, the mean absolute error is nearly consistent between both feedback heads irrespective of the model used which shows that the models don't have bias towards either head.

4.2.4 Discussion

In this chapter, we have shown the usefulness of the presented axial and shear model in predicting the feedback head locations for a three-actuator parallel system with one feedback head, delta mechanism, and a five-actuator system with two feedback heads, floating actuator mechanism. This was done by presenting the design and manufacturing of these systems, creating a position prediction algorithm based on the presented models, and finally conducting experiments to quantify the accuracy of the position prediction models as compared to previous work. The delta mechanism had a mean absolute error of 0.04 mm as compared to 0.22 mm for the previous pressurized spring model, and the floating actuator mechanism has a mean absolute error of 0.27 mm using the presented axial and shear model as compared to 0.55 mm from the pressurized spring model. Thus, showing the improvements achieved by this modeling approach. Next, we will provide a conclusion to the thesis and provide recommendations for future work in Chapter 5.

5. CONCLUSIONS

In this chapter, we briefly review the work we have presented, and then provide recommendations for future work. In this thesis, we showed how movements of complex soft parallel mechanisms can be well predicted by characterizing both active and passive forces of its one degree-of-freedom soft actuator, as compared to characterizing only active force directions.

First, we reviewed the previous work that is done in the field of soft robots and soft actuators in Chapter 1. Here, we motivated the need for a simplified modeling approach for soft robots by characterizing both the active and passive forces exerted and then, provided background on the state of the art in soft bellows actuators, and modeling of soft robots. In Chapter 2, we presented our bellows actuator design and manufacturing process followed by force models for active (axial) and passive (shear) forces using a pressurized piston, and parallel linear and torsional springs system which is one of the major contributions of this work. Previous work has characterized forces in only active directions, axial for soft bellows actuators, but that does not sufficiently encapsulate the actuator's force profile when deformed. To experimentally verify the model, and to obtain the modeling constants defined, a static test setup was designed and manufactured in Chapter 3. Here, we also performed the characterization tests and obtain the required model constants using data fitting. Finally, we extended our derived force models to more complex soft robots in Chapter 4. We designed and manufactured two parallel systems, the delta mechanism and the novel floating actuator mechanism. Thereafter, we derived the position prediction algorithms for them using the developed force models, and performed experiments to obtain true position using image processing. We compared the accuracy of the proposed axial and shear force models, to the previous pressurized spring model and identified significant improvements in position prediction. For the delta mechanism, an average absolute error of 0.04 mm was observed using the proposed model as compared to 0.22 mm for the pressurized spring model, which is an 81.8% improvement. For the floating actuator mechanism, the errors were higher as expected due to the increased complexity, but the position prediction algorithm performed well using the axial and shear model. A mean absolute error of 0.27 mm was obtained with the presented model as compared to 0.55 mm with the previous model, quantifying a 50%

improvement in position prediction. Hence, we can see improvements in modeling of the actuator forces using the proposed approach of characterizing both active and passive forces exerted by the one degree-of-freedom actuator of a more complex soft robot. Using this modeling approach as a design tool can potentially help to analyze forces and deformations more efficiently in preliminary stages of complex soft robot design. It could also reduce computation time in preliminary finite elements analysis, serve as validation to simulations, and simplify kinematic models for initial stages of controller design.

In future work, we recommend improving the presented model to characterize small bending of the actuators and further reduce errors, extending the model to predict more complex systems of parallel and series actuators, and testing the feasibility of this simplified model for other actuator designs where active and passive forces can be similarly analyzed. Additionally, while the demonstration uses a static model for pressure estimation in planar movement, specifically eliminating viscous material effects, it would be useful to study dynamic response of this system for a robust controller design. It would be particularly useful to design systems for three-dimensional actuation and expand the predictive workspace. Finally, results from the presented work and inferences from the aforementioned improvements can be used to design a haptic device similar to the floating actuator mechanism for effectively simulating skin-stretch and slip, where the device is capable of simulating complex patterns using motion planning and appropriate controller design.

REFERENCES

[1] B. Trimmer, "Soft robots," *Current Biology*, vol. 23, no. 15, R639–R641, 2013.

[2] N. Elango and A. Faudzi, "A review article: Investigations on soft materials for soft robot manipulations," *The International Journal of Advanced Manufacturing Technology*, vol. 80, no. 5, pp. 1027–1037, 2015.

[3] R. F. Shepherd, F. Ilievski, W. Choi, S. A. Morin, A. A. Stokes, A. D. Mazzeo, X. Chen, M. Wang, and G. M. Whitesides, "Multigait soft robot," *Proceedings of the national academy of sciences*, vol. 108, no. 51, pp. 20 400–20 403, 2011.

[4] S. Kim, C. Laschi, and B. Trimmer, "Soft robotics: A bioinspired evolution in robotics," *Trends in biotechnology*, vol. 31, no. 5, pp. 287–294, 2013.

[5] C. Della Santina, M. G. Catalano, and A. Bicchi, "Soft robots," *Encyclopedia of Robotics*, vol. 489, 2020.

[6] C. Laschi, M. Cianchetti, B. Mazzolai, L. Margheri, M. Follador, and P. Dario, "Soft robot arm inspired by the octopus," *Advanced robotics*, vol. 26, no. 7, pp. 709–727, 2012.

[7] F. Negrello, A. Settimi, D. Caporale, G. Lentini, M. Poggiani, D. Kanoulas, L. Muratore, E. Luberto, G. Santaera, L. Ciarleglio, L. Ermini, L. Pallottino, D. G. Caldwell, N. Tsagarakis, A. Bicchi, M. Garabini, and M. G. Catalano, "Humanoids at work: The walkman robot in a postearthquake scenario," *IEEE Robotics Automation Magazine*, vol. 25, no. 3, pp. 8–22, 2018. DOI: 10.1109/MRA.2017.2788801.

[8] E. W. Hawkes, L. H. Blumenschein, J. D. Greer, and A. M. Okamura, "A soft robot that navigates its environment through growth," *Science Robotics*, vol. 2, no. 8, 2017.

[9] E. T. Roche, M. A. Horvath, I. Wamala, A. Alazmani, S.-E. Song, W. Whyte, Z. Machaidze, C. J. Payne, J. C. Weaver, G. Fishbein, J. Kuebler, N. V. Vasilyev, D. J. Mooney, F. A. Pigula, and C. J. Walsh, "Soft robotic sleeve supports heart function," *Science Translational Medicine*, vol. 9, no. 373, 2017. DOI: 10.1126/scitranslmed.aaf3925.

[10] T. Ranzani, G. Gerboni, M. Cianchetti, and A. Menciassi, "A bioinspired soft manipulator for minimally invasive surgery," *Bioinspiration & biomimetics*, vol. 10, no. 3, 2015.

[11] D. Rus and M. T. Tolley, "Design, fabrication and control of soft robots," *Nature*, vol. 521, no. 7553, pp. 467–475, 2015.

[12] M. Cianchetti, C. Laschi, A. Menciassi, and P. Dario, "Biomedical applications of soft robotics," *Nature Reviews Materials*, vol. 3, no. 6, pp. 143–153, 2018.

[13] N. El-Atab, R. B. Mishra, F. Al-Modaf, L. Joharji, A. A. Alsharif, H. Alamoudi, M. Diaz, N. Qaiser, and M. M. Hussain, "Soft actuators for soft robotic applications: A review," *Advanced Intelligent Systems*, vol. 2, no. 10, p. 2 000 128, 2020.

[14] L. Cappello, J. T. Meyer, K. C. Galloway, J. D. Peisner, R. Granberry, D. A. Wagner, S. Engelhardt, S. Paganoni, and C. J. Walsh, "Assisting hand function after spinal cord injury with a fabric-based soft robotic glove," *Journal of neuroengineering and rehabilitation*, vol. 15, no. 1, pp. 1–10, 2018.

[15] J. D. Greer, L. H. Blumenschein, R. Alterovitz, E. W. Hawkes, and A. M. Okamura, "Robust navigation of a soft growing robot by exploiting contact with the environment," *The International Journal of Robotics Research*, vol. 39, no. 14, pp. 1724–1738, 2020.

[16] M. Manti, T. Hassan, G. Passetti, N. D'Elia, C. Laschi, and M. Cianchetti, "A bioinspired soft robotic gripper for adaptable and effective grasping," *Soft Robotics*, vol. 2, no. 3, pp. 107–116, 2015.

[17] J. D. Greer, T. K. Morimoto, A. M. Okamura, and E. W. Hawkes, "Series pneumatic artificial muscles (sPAMs) and application to a soft continuum robot," in *IEEE International Conference on Robotics and Automation*, 2017, pp. 5503–5510.

[18] G. Singh and G. Krishnan, "A constrained maximization formulation to analyze deformation of fiber reinforced elastomeric actuators," *Smart Materials and Structures*, vol. 26, no. 6, p. 065 024, 2017.

[19] R. S. Diteesawat, T. Helps, M. Taghavi, and J. Rossiter, "Characteristic analysis and design optimization of bubble artificial muscles," *Soft Robotics*, 2020.

[20] C. Duriez, "Control of elastic soft robots based on real-time finite element method," *IEEE International Conference on Robotics and Automation*, pp. 3982–3987, 2013. DOI: 10.1109/icra.2013.6631138.

[21] O. Goury and C. Duriez, "Fast, generic, and reliable control and simulation of soft robots using model order reduction," *IEEE Transactions on Robotics*, vol. 34, no. 6, pp. 1565–1576, 2018. DOI: 10.1109/tro.2018.2861900.

[22] H. Zhang, Y. Wang, M. Y. Wang, J. Y. H. Fuh, and A. S. Kumar, "Design and Analysis of Soft Grippers for Hand Rehabilitation," ser. International Manufacturing Science and Engineering Conference, V004T05A003, vol. Volume 4: Bio and Sustainable Manufacturing, Jun. 2017. DOI: 10.1115/MSEC2017-2814.

[23] R. J. Webster III and B. A. Jones, "Design and kinematic modeling of constant curvature continuum robots: A review," *The International Journal of Robotics Research*, vol. 29, no. 13, pp. 1661–1683, 2010.

[24] R. K. Katzschmann, C. Della Santina, Y. Toshimitsu, A. Bicchi, and D. Rus, "Dynamic motion control of multi-segment soft robots using piecewise constant curvature matched with an augmented rigid body model," in *2nd IEEE International Conference on Soft Robotics*, 2019, pp. 454–461.

[25] C. D. Onal and D. Rus, "A modular approach to soft robots," *IEEE RAS EMBS International Conference on Biomedical Robotics and Biomechatronics*, pp. 1038–1045, 2012. DOI: 10.1109/biorob.2012.6290290.

[26] L. H. Blumenschein and Y. Mengüç, "Generalized delta mechanisms from soft actuators," in *International Conference on Soft Robotics*, 2019, pp. 249–256.

[27] G. Dämmer, S. Gablenz, A. Hildebrandt, and Z. Major, "Polyjet-printed bellows actuators: Design, structural optimization, and experimental investigation," *Frontiers in Robotics and AI*, vol. 6, p. 34, 2019.

[28] G. Dämmer, S. Gablenz, A. Hildebrandt, and Z. Major, "Design and shape optimization of polyjet bellows actuators," in *IEEE International Conference on Soft Robotics*, 2018, pp. 282–287. DOI: 10.1109/ROBOSOFT.2018.8404933.

[29] D. Drotman, M. Ishida, S. Jadhav, and M. T. Tolley, "Application-driven design of soft, 3-d printed, pneumatic actuators with bellows," *IEEE/ASME Transactions on Mechatronics*, vol. 24, no. 1, pp. 78–87, 2019. DOI: 10.1109/TMECH.2018.2879299.

[30] J. Fras, Y. Noh, H. Wurdemann, and K. Althoefer, "Soft fluidic rotary actuator with improved actuation properties," in *IEEE/RSJ International Conference on Intelligent Robots and Systems*, 2017, pp. 5610–5615. DOI: 10.1109/IROS.2017.8206448.

[31] J. Cao, L. Qin, J. Liu, Q. Ren, C. C. Foo, H. Wang, H. P. Lee, and J. Zhu, "Untethered soft robot capable of stable locomotion using soft electrostatic actuators," *Extreme Mechanics Letters*, vol. 21, pp. 9–16, 2018.

[32] N. Kohls, B. Dias, Y. Mensah, B. P. Ruddy, and Y. C. Mazumdar, "Compliant electromagnetic actuator architecture for soft robotics," in *IEEE International Conference on Robotics and Automation*, 2020, pp. 9042–9049. DOI: 10.1109/ICRA40945.2020.9197442.

[33] R. Hashem, M. Stommel, L. K. Cheng, and W. Xu, "Design and characterization of a bellows-driven soft pneumatic actuator," *IEEE/ASME Transactions on Mechatronics*, vol. 26, no. 5, pp. 2327–2338, 2020.

[34] A. De Greef, P. Lambert, and A. Delchambre, "Towards flexible medical instruments: Review of flexible fluidic actuators," *Precision engineering*, vol. 33, no. 4, pp. 311–321, 2009.

[35] I. Sîrbu, G. Moretti, G. Bortolotti, M. Bolignari, S. Diré, L. Fambri, R. Vertechy, and M. Fontana, "Electrostatic bellow muscle actuators and energy harvesters that stack up," *Science Robotics*, vol. 6, no. 51, eaaz5796, 2021.

[36] G. Mao, M. Drack, M. Karami-Mosammam, D. Wirthl, T. Stockinger, R. Schwödiauer, and M. Kaltenbrunner, "Soft electromagnetic actuators," *Science advances*, vol. 6, no. 26, eabc0251, 2020.

[37] W. Jung, S. Lee, J. Lee, and Y. Hwang, "Wirelessly powered micro soft bellows actuator with 3d helix coils," in *IEEE International Conference on Micro Electro Mechanical Systems Conference*, 2022, pp. 361–364. DOI: 10.1109/MEMS51670.2022.9699778.

[38] P. Boyraz, G. Runge, and A. Raatz, "An overview of novel actuators for soft robotics," *Actuators*, vol. 7, no. 3, 2018. DOI: 10.3390/act7030048.

[39] Y. Shapiro, A. Wolf, and K. Gabor, "Bi-bellows: Pneumatic bending actuator," *Sensors and Actuators A: Physical*, vol. 167, no. 2, pp. 484–494, 2011, Solid-State Sensors, Actuators and Microsystems Workshop. DOI: https://doi.org/10.1016/j.sna.2011.03.008.

[40] G. Udupa, P. Sreedharan, P. Sai Dinesh, and D. Kim, "Asymmetric bellow flexible pneumatic actuator for miniature robotic soft gripper," *Journal of Robotics*, vol. 2014, no. 902625, 2014. DOI: 10.1155/2014/902625.

[41] T. Rehman, A. A. M. Faudzi, D. E. O. Dewi, and M. S. M. Ali, "Design, characterization, and manufacturing of circular bellows pneumatic soft actuator," *The International Journal of Advanced Manufacturing Technology*, vol. 93, no. 9, pp. 4295–4304, 2017.

[42] G. Stano and G. Percoco, "Additive manufacturing aimed to soft robots fabrication: A review," *Extreme Mechanics Letters*, vol. 42, p. 101 079, 2021.

[43] B. Gorissen, D. Reynaerts, S. Konishi, K. Yoshida, J.-W. Kim, and M. De Volder, "Elastic inflatable actuators for soft robotic applications," *Advanced Materials*, vol. 29, no. 43, p. 1 604 977, 2017.

[44] F. Schmitt, O. Piccin, L. Barbé, and B. Bayle, "Soft robots manufacturing: A review," *Frontiers in Robotics and AI*, vol. 5, p. 84, 2018.

[45] J. Hughes, U. Culha, F. Giardina, F. Guenther, A. Rosendo, and F. Iida, "Soft manipulators and grippers: A review," *Frontiers in Robotics and AI*, vol. 3, p. 69, 2016.

[46] C. G. Harris, N. J. Jursik, W. E. Rochefort, and T. W. Walker, "Additive manufacturing with soft TPU–adhesion strength in multimaterial flexible joints," *Frontiers in Mechanical Engineering*, vol. 5, p. 37, 2019.

[47] F. Liravi and E. Toyserkani, "Additive manufacturing of silicone structures: A review and prospective," *Additive Manufacturing*, vol. 24, pp. 232–242, 2018.

[48] A. R. Studart, "Additive manufacturing of biologically-inspired materials," *Chemical Society Reviews*, vol. 45, no. 2, pp. 359–376, 2016.

[49] R. T. Shafranek, S. C. Millik, P. T. Smith, C.-U. Lee, A. J. Boydston, and A. Nelson, "Stimuli-responsive materials in additive manufacturing," *Progress in Polymer Science*, vol. 93, pp. 36–67, 2019.

[50] N. W. Bartlett, M. T. Tolley, J. T. Overvelde, J. C. Weaver, B. Mosadegh, K. Bertoldi, G. M. Whitesides, and R. J. Wood, "A 3d-printed, functionally graded soft robot powered by combustion," *Science*, vol. 349, no. 6244, pp. 161–165, 2015.

[51] M. Decker, "Soft robotics and emergent materials in architecture," in *eCAADe Conference*, vol. 2, 2015.

[52] H. Zhao, Y. Li, A. Elsamadisi, and R. Shepherd, "Scalable manufacturing of high force wearable soft actuators," *Extreme Mechanics Letters*, vol. 3, pp. 89–104, 2015. DOI: https://doi.org/10.1016/j.eml.2015.02.006.

[53] J. Walker, T. Zidek, C. Harbel, S. Yoon, F. S. Strickland, S. Kumar, and M. Shin, "Soft robotics: A review of recent developments of pneumatic soft actuators," *Actuators*, vol. 9, no. 3, 2020.

[54] T. Wallin, J. Pikul, and R. Shepherd, "3d printing of soft robotic systems," *Nature Reviews Materials*, vol. 3, no. 6, pp. 84–100, 2018.

[55] C. Tawk and G. Alici, "Finite element modeling in the design process of 3D printed pneumatic soft actuators and sensors," *Robotics*, vol. 9, no. 3, p. 52, 2020.

[56] B. A. Jones and I. D. Walker, "Kinematics for multisection continuum robots," *IEEE Transactions on Robotics*, vol. 22, no. 1, pp. 43–55, 2006.

[57] J. Till, V. Aloi, and C. Rucker, "Real-time dynamics of soft and continuum robots based on cosserat rod models," *The International Journal of Robotics Research*, vol. 38, no. 6, pp. 723–746, 2019.

[58] P. Ćurković and A. Jambrečić, "Improving structural design of soft actuators using finite element method analysis," *Interdisciplinary Description of Complex Systems: INDECS*, vol. 18, no. 4, pp. 490–500, 2020.

[59] F. Largilliere, V. Verona, E. Coevoet, M. Sanz-Lopez, J. Dequidt, and C. Duriez, "Real-time control of soft-robots using asynchronous finite element modeling," in *IEEE International Conference on Robotics and Automation*, IEEE, 2015, pp. 2550–2555.

[60] J. Chenevier, D. González, J. V. Aguado, F. Chinesta, and E. Cueto, "Reduced-order modeling of soft robots," *PloS one*, vol. 13, no. 2, 2018.

[61] M. Thieffry, A. Kruszewski, C. Duriez, and T.-M. Guerra, "Control design for soft robots based on reduced-order model," *IEEE Robotics and Automation Letters*, vol. 4, no. 1, pp. 25–32, 2019. DOI: 10.1109/LRA.2018.2876734.

[62] L. Marechal, P. Balland, L. Lindenroth, F. Petrou, C. Kontovounisios, and F. Bello, "Toward a common framework and database of materials for soft robotics," *Soft robotics*, vol. 8, no. 3, pp. 284–297, 2021.

[63] E. Coevoet, T. Morales-Bieze, F. Largilliere, Z. Zhang, M. Thieffry, M. Sanz-Lopez, B. Carrez, D. Marchal, O. Goury, J. Dequidt, *et al.*, "Software toolkit for modeling, simulation, and control of soft robots," *Advanced Robotics*, vol. 31, no. 22, pp. 1208–1224, 2017.

[64] S. Khetan and L. H. Blumenschein, "Characterization of soft 3D printed actuators for parallel networks," *IEEE Robotics and Automation Letters*, vol. 7, no. 2, pp. 5342–5348, 2022. DOI: 10.1109/LRA.2022.3155807.

[65] E. Battaglia, J. P. Clark, M. Bianchi, M. G. Catalano, A. Bicchi, and M. K. O'Malley, "The rice haptic rocker: Skin stretch haptic feedback with the pisa/IIT softhand," in *IEEE World Haptics Conference*, 2017, pp. 7–12. DOI: 10.1109/WHC.2017.7989848.

[66] F. Ilievski, A. D. Mazzeo, R. F. Shepherd, X. Chen, and G. M. Whitesides, "Soft robotics for chemists," *Angewandte Chemie International Edition*, vol. 50, no. 8, pp. 1890–1895, 2011. DOI: https://doi.org/10.1002/anie.201006464.

[67] S. Wakimoto, K. Ogura, K. Suzumori, and Y. Nishioka, "Miniature soft hand with curling rubber pneumatic actuators," *IEEE International Conference on Robotics and Automation*, pp. 556–561, May 2009. DOI: 10.1109/ROBOT.2009.5152259.

[68] *Elastic 50A*, FLELCL01, Rev. 01, Formlabs, 2019. [Online]. Available: https://formlabs-media.formlabs.com/datasheets/2001420-TDS-ENUS-0.pdf.

[69] *Standard*, FLGPCL04, Rev. 01, Formlabs, 2017. [Online]. Available: https://formlabs-media.formlabs.com/datasheets/Clear_Resin_Technical.pdf.

[70] *Flexible 80A*, FLFL8001, Rev. 01, Formlabs, 2020. [Online]. Available: https://formlabs-media.formlabs.com/datasheets/2001418-TDS-ENUS-0.pdf.

[71] F. Boyer, V. Lebastard, F. Candelier, and F. Renda, "Dynamics of continuum and soft robots: A strain parameterization based approach," *IEEE Transactions on Robotics*, vol. 37, no. 3, pp. 847–863, 2021. DOI: 10.1109/TRO.2020.3036618.

[72] ATI, *Mini40-E transducer with strain relieved cable, rev. 09*, Aug. 2016. [Online]. Available: https://www.ati-ia.com/app_content/Documents/9230-05-1314.auto.pdf.

[73] ATI, *9620-05-transducer section, six-axis force/torque sensor system*. [Online]. Available: https://www.ati-ia.com/app_content/documents/9620-05-Transducer20Section.pdf.

[74] ProportionAir, *Qb3 electro-pneumatic pressure regulator*. [Online]. Available: https://proportionair.com/literature/brochures/QB3-datasheet.pdf.

[75] Honeywell, *Trustability board mount pressure sensors*. [Online]. Available: https://www.mouser.com/datasheet/2/187/honeywell-sensing-trustability-hsc-series-high-acc-1228679.pdf.

[76] *Draft*, FLDRGR02, Rev. 01, Formlabs, 2020. [Online]. Available: https://formlabs-media.formlabs.com/datasheets/2001477-TDS-ENUS-0.pdf.